Improving Nanosatellite Capabilities for Atmospheric Sounding and Characterization

by

Anne Dorothy Marinan
B.S., University of Michigan (2011)
S.M., Massachusetts Institute of Technology (2013)

Submitted to the Department of Aeronautics and Astronautics
in partial fulfillment of the requirements for the degree of
Doctor of Philosophy in Aerospace Engineering
at the
MASSACHUSETTS INSTITUTE OF TECHNOLOGY
June 2016

Author ..... Signature redacted
Department of Aeronautics and Astronautics
May 19, 2016

Certified by ..... Signature redacted
Kerri L. Cahoy
Assistant Professor of Aeronautics and Astronautics
Thesis Supervisor

Certified by ..... Signature redacted
David W. Miller
Jerome Hunsaker Professor of Aeronautics and Astronautics

Certified by ..... Signature redacted
Bruce Macintosh
Professor of Physics, Stanford University

Certified by ..... Signature redacted
Ruslan Belikov
Astrophysicist, NASA Ames Research Center

Accepted by ..... Signature redacted
Paulo C. Lozano
Chairman, Graduate Program Committee

Improving Nanosatellite Capabilities for Atmospheric Sounding and Characterization

by

Anne Dorothy Marinan

Submitted to the Department of Aeronautics and Astronautics
on May 19, 2016, in partial fulfillment of the
requirements for the degree of
Doctor of Philosophy in Aerospace Engineering

Abstract

Measurements of atmospheric temperature, pressure, water vapor, and composition are important to users in the Earth science, defense, and intelligence communities. Nanosatellites (with mass < 10 kg, such as CubeSats) can support miniaturized instruments for atmospheric sounding and characterization. Nanosatellite constellations can improve spatial and temporal coverage of Earth and can produce data consistent with the current state of the art at reduced cost compared with larger satellites. Nanosatellites are also used for on-orbit technology demonstrations due to low cost and higher risk posture. We focus on CubeSats as a host platform for instruments and technology demonstrations for three kinds of atmospheric sensors: (i) passive microwave radiometers, (ii) atmospheric occultation experiments and (iii) coronagraphic direct imaging of exoplanets.

Microwave radiometers (MWR) measure brightness temperatures in multiple channels across bands centered on atmospheric absorption features. MWRs require stable cold and warm calibration targets for accurate measurements. CubeSat MWRs, such as MicroMAS (the Micro-sized Microwave Atmospheric Satellite) and MiRaTA (Microwave Radiometer Technology Acceleration), use deep space as a cold target with a noise diode as the warm target instead of larger calibration targets. However, noise diodes drift, and a better calibration method is needed to meet the desired measurement precision.

Occultation experiments measure electromagnetic signals received from a transmitter as it passes behind the Earth from the perspective of the receiver. In the neutral atmosphere, the measurements yield profiles of temperature, pressure and in certain configurations, composition. We consider radio and optical wavelengths. GPS Radio Occultation (GPSRO) instruments measure phase delay in signals transmitted from GPS satellites that travel through the atmosphere to a low earth orbit (LEO) receiver. GPSRO measurements are inherently well calibrated, because the primary interaction is of an electromagnetic wave through a medium, and have high accuracy and vertical resolution. We show that it is possible to make several GPSRO measurements per day that are collocated spatially and temporally with space-based MWR measure-

ments and that using these measurements enables better MWR calibration by measuring noise diode drift. Occultation observations using several near infrared optical wavelengths can measure absorption features to characterize atmospheric species and abundances. Intersatellite optical links are used for these measurements, but transmissions deep in the atmosphere experience scintillation and distortion. Wavefront control systems could be used to compensate for atmosphere-induced aberrations.

Wavefront control systems are also needed to obtain reflection absorption spectra of exoplanet atmospheres, where photons from the host star are reflected by the planet. A space-based telescope equipped with an internal coronagraph can make high contrast measurements off-axis using high spatial frequency wavefront control systems to correct for speckles, imperfections, and other distortions that would degrade the measurement. High actuator count deformable mirrors (DMs) are needed, and Microelectromechanical systems (MEMS) DMs can provide a cost-effective, compact solution. We describe our design for a nanosatellite platform using a wavefront sensor to characterize the on-orbit performance of MEMS DMs.

We present results from these new approaches to improve atmospheric sounding and characterization missions using nanosatellites. Our hardware analysis for MiRaTA demonstrates that the CubeSat GPSRO instrument noise performance supports the calibration of the noise diode to improve the CubeSat MWR measurement accuracy from > 0.75 K to 0.25 K. We simulate and experimentally demonstrate a CubeSat wavefront control system using a MEMS DM that can be used to characterize the performance of MEMS DMs, sensitive to 10's of nm motion and up to three times the 1.5 μm-stroke of the DMs, which is useful for future applications in both atmospheric near infrared occultation as well as in exoplanet direct imaging space telescopes. Each of these contributions improves current nanosatellite capabilities or uses nanosatellites to advance technologies in future larger systems for atmospheric sounding and characterization of Earth and exoplanets.

Thesis Supervisor: Kerri L. Cahoy
Title: Assistant Professor of Aeronautics and Astronautics

Committee Member: David W. Miller
Title: Jerome Hunsaker Professor of Aeronautics and Astronautics

Committee Member: Bruce Macintosh
Title: Professor of Physics, Stanford University

Committee Member: Ruslan Belikov
Title: Astrophysicist, NASA Ames Research Center

Acknowledgments

Thank you to everyone who mentored, advised, supported, and encouraged me through this process.

I would like to acknowledge and thank my advisor, Kerri Cahoy, for her continuous encouragement and inspiration both in and out of the lab.

I further acknowledge the MicroMAS and MiRaTA teams in the STAR Lab for their extraordinary effort and dedication to the project. Thanks also to everyone I interacted with at Lincoln Laboratory for their advice and exceeding willingness to help out.

Finally, I would like to thank my family (Mom, Dad, Marie, Kathleen, Emily, and John) as well as Meghan and Austin for their invaluable support and reassurance. This work was supported by a NASA Office of the Chief Technologists Space Technology Research Fellowship as well as by funds provided by the William Asbjornsen Albert Memorial Fellowship. Analytical Graphics, Inc provided the Systems Toolkit software and modules used in this analysis through the Educational Alliance Program with MIT.

Contents

1 Introduction 1

1.1 Motivation - Nanosatellites for Atmospheric Characterization 2

1.2 State of the Art and Gap Identification 2

1.2.1 CubeSat Capabilities 2

1.2.2 Atmospheric Sounding and Characterization 6

1.2.2.1 Microwave Radiometry 8

1.2.2.2 Atmospheric Occultation 8

1.2.2.3 Exoplanet Detection and Characterization Methods . 11

1.2.3 Adaptive Optics 12

1.2.4 Ground Applications for Adaptive Optics 14

1.2.5 Space Applications for Adaptive Optics 15

1.3 Research Contributions 16

1.4 Thesis Organization 18

2 Nanosatellite Atmospheric Sounding Technology: Literature Review **21**

2.1 CubeSat Requirements to Support Atmospheric Sensing 22

2.1.1 Structure and Accommodation 22

2.1.2 Power 23

2.1.3 Data 23

2.1.4 Pointing 24

2.1.5 Positioning 24

2.1.6 Thermal Management 25

2.1.7 Global Coverage Considerations . . . 25
2.2 Microwave Radiometry . . . 26
2.2.1 Measurement Principles . . . 27
2.2.2 CubeSat Microwave Radiometry Missions . . . 27
2.2.3 Calibration and Coverage Challenges . . . 30
2.3 Atmospheric Occultation . . . 30
2.3.1 Radio Occultation . . . 30
2.3.1.1 Radio Occultation Measurement Principles . . . 31
2.3.1.2 CubeSat Radio Occultation Missions . . . 32
2.3.1.3 Lower Atmospheric Sounding Challenge . . . 33
2.3.2 Laser Occultation . . . 35
2.3.2.1 Laser Occultation Absorption Measurement Principles 35
2.3.2.2 CubeSat Intersatellite Communications Missions . . 36
2.3.2.3 Challenges of Lower Atmospheric Occultations . . . 36
2.3.2.4 Adaptive Optics for Atmospheric Correction . . . 37
2.4 Exoplanet Direct Imaging . . . 38
2.4.1 Achieving High Contrast with Adaptive Optics . . . 40
2.4.1.1 Space Qualification . . . 43
2.5 Summary of Gap and Contributions . . . 45

3 Nanosatellite Atmospheric Sounding and Sensor Calibration 49
3.1 Nanosatellite Microwave Radiometry . . . 49
3.1.1 CubeSat Microwave Radiometer Design and Calibration . . . 50
3.1.2 MiRaTA Radiometer and Mission Overview . . . 52
3.1.3 MiRaTA Radiometer . . . 54
3.1.4 MiRaTA GPSRO Sensor . . . 55
3.1.5 MiRaTA Radiometer Calibration Process . . . 56
3.2 Nanosatellite GPS Radio Occultation . . . 58
3.2.1 Benefit of GPS Radio Occultation Measurements . . . 58
3.2.2 Achieving Global Occultation Measurements with CubeSats . 58

3.2.2.1 Orbits and GPSRO Model for Global Measurements 59
3.2.2.2 Global GPSRO Coverage Results 60
3.3 Radiometer Calibration with Radio Occultation - Overlapping Measurements 61
3.3.1 Calibration Opportunities for the MiRaTA Mission 64
3.3.1.1 MiRaTA Calibration Overlap Model 65
3.3.1.2 MiRaTA Calibration Overlap Results 65
3.3.2 Calibration Opportunities for other Low Earth Orbits 66
3.4 Radiometer Calibration with Radio Occultation - Measurement Errors 67
3.4.1 Sources of Error in Radio Occultation 69
3.4.2 Assessing Nanosatellite Temperature Retrieval Error 71
3.4.2.1 The CTAGS Instrument 71
3.4.2.2 SNR and Signal Acquisition 72
3.4.2.3 Measured Bending Angle Error 73
3.4.2.4 Calculating Nanosatellite Temperature Precision . . 75
3.4.2.5 Results 77
3.5 Summary of Contributions 79

4 Nanosatellite Atmospheric Characterization 81
4.1 Laser and Stellar Occultation 81
4.1.1 Achieving Global Measurements with LEO Intersatellite Links 83
4.1.2 Sources of Error for Laser Occultation - Atmospheric Turbulence 85
4.1.3 Turbulence Calculation Approach 86
4.1.3.1 Refractive Structure Index 89
4.1.3.2 Fried Parameter 89
4.1.3.3 Greenwood Frequency 90
4.1.4 Adaptive Optics System Correction and Error 91
4.1.5 Feasibility of Adaptive Optics for Crosslink Correction 93
4.2 Exoplanet Direct Imaging 94
4.2.1 Principles of High-Contrast Imaging with AO 94

4.3 Nanosatellite Deformable Mirror Validation 96
4.3.1 Need for Space Qualification 97
4.4 Summary of Contributions 97

5 CubeSat Wavefront Sensor Design to Enable Earth and Exoplanet Atmospheric Characterization 101

5.1 DeMi Mission Overview 102
5.1.1 DeMi Mission Goals 102
5.1.2 DeMi Operation 103
5.1.2.1 Experiment 0: Mirror Characterization 105
5.1.2.2 Experiment 1: Wavefront Correction on Internal Source 105
5.1.2.3 Experiment 2: Wavefront Correction on External Object 105
5.2 Design and Performance Analysis 106
5.2.1 Science Traceability 106
5.2.2 DeMi Design Overview 107
5.2.3 Wavefront Sensor Design: Shack Hartmann 110
5.2.4 Science Image Design: Focal Plane Sensor 112
5.3 DeMi Satellite System Requirements 114
5.3.1 DeMi Pointing and Jitter Requirements 115
5.3.2 Other Considerations 116
5.4 Summary of Contributions 116

6 Laboratory Validation of CubeSat Adaptive Optics Payload for Atmospheric Characterization 119

6.1 Hardware Setup 120
6.2 Software Setup 121
6.3 Open-Loop Wavefront Reconstruction 123
6.3.1 Reconstruction Algorithm 123
6.3.2 Truth measurements with Zygo Interferometer 124
6.3.3 Results 125
6.3.4 Limitations and Future Modifications 126

6.4 Closed-Loop Wavefront Control 128
6.4.1 System Characterization 128
6.4.1.1 Theoretical Reference Grid 128
6.4.1.2 Calibration and Registration 128
6.4.2 Closed-Loop Correction Algorithm 129
6.4.2.1 Wavefront Error Measurement 129
6.4.2.2 Wavefront Error Reconstruction and Control 129
6.4.2.3 Commanding the Mirror 131
6.4.3 Results 131
6.5 Limitations and Flight Implementation 133

7 Conclusions and Future Work **135**
7.1 Research Contributions 135
7.2 Future Work 137
7.2.1 Nanosatellite Atmospheric Sounding 137
7.2.2 Nanosatellite Atmospheric Characterization 139
7.2.3 Nanosatellite Adaptive Optics Technology Demonstration . . . 139

A MATLAB Code **141**
A.1 GPS Radio Occultation 141
A.1.1 Access Calculations 141
A.1.2 Temperature Precision 156
A.2 Open-Loop Wavefront Reconstruction 164
A.3 Closed-Loop Wavefront Control 178
A.3.1 Calibration 178
A.3.2 Closed-Loop Operation 190

List of Figures

1-1 Projected CubeSat mission applications show dramatic increase in scientific and remote sensing fields 5

1-2 Atmospheric transparency across the electromagnetic spectrum. We focus on visible/infrared and radio/microwave wavelengths. 6

1-3 Occultation sensing techniques measure the interaction of electromagnetic waves with the atmosphere to determine atmospheric properties [25]. 9

1-4 There are three main elements to an adaptive optics system: the deformable mirror, the wavefront sensor, and the control system. 13

2-1 Area of contribution in context with major areas of research 22

2-2 Microwave and millimeter wave absorption spectrum for dry air and air with water vapor [73] 28

2-3 GPS radio occultation measures signal bending (elongation) through the atmosphere and retrieves temperature and pressure information. [80] 31

2-4 Difference in retrievals for open-loop and closed-loop tracking for the CHAMP mission 34

2-5 Electrostatic DM actuator architectures: (Top) continuous facesheet and (Bottom) segmented apertures. 38

2-6 Long term 0-degree astigmatism aberrations observed on the Hubble Space Telescope [111] 41

2-7 Zernike modes are a set of orthogonal basis functions used to describe the surface of a wavefront. We distinguish between lower and higher-order modes 42

3-1 Radiometer calibration setup with warm and cold targets [125] 51

3-2 Diagram of MiRaTA radiometer internal electronics. Top: The V-band receiver modules include an internal matched load as well as a noise diode. Bottom: The G-band receiver modules include a noise diode. . 52

3-3 MiRaTA Axes and Orientation Nomenclature. Left: Local Vertical Local Horizontal (LVLH) orientation. Right: Pitched-up orientation to achieve GPS Radio Occultation with assumed 115 degree pitch-up angle 54

3-4 The MiRaTA CubeSat primary mission validation Concept of Operations pitch-up maneuver 55

3-5 Ground processing and validation flow for the MiRaTA mission data products (blue highlight box indicates contributions from this thesis) 57

3-6 Model architecture for a GPSRO payload 60

3-7 Summary of occultation opportunities for a range of possible orbits over 3 months 60

3-8 GPSRO Signal to noise ratio for (A) antenna gain of 9 dB, (B) antenna gain of 9.5 dB, and (c) antenna gain of 10 dB for varying orbit parameters (assuming a Gaussian antenna profile) 61

3-9 Revisit Times for (top) One (middle) Three and (bottom) Six GPS RO satellites. Color bars are consistent across all three plots. 62

3-10 When limb-facing, the radiometer weighting function is about 3.5 km higher than when the radiometer is nadir-facing 64

3-11 Tangential height (< 25 km) as a function of latitude and longitude for all visible setting GPS satellites over one day 66

3-12 Tangential height (< 25 km) as a function of latitude and longitude for all visible setting GPS satellites within the radiometer field of view over three months 67

3-13 Histogram and CDF of expected overlapping occultation durations for the MiRaTA mission 68

3-14 Number of occultations that overlap with a given radiometer field of view over 3 months 68

3-15 Latitude and Longitude Locations of Overlapping Radiometer and GPSRO limb measurements over three months (400 km altitude) 69

3-16 Process for estimating temperature precision for the MiRaTA GPSRO measurements based on thermal phase noise. 71

3-17 Bending angle precision vs. tangential height predicted for thermal noise error contributions (does not include atmospheric conditions, clock noise, position/velocity errors, or multipath effects) 76

3-18 Error in temperature calculations due to numerical approximations in performing the Abel transform. For a detailed treatment of the radio occultation mapping kernel, see Ahmad 1998 [136] 77

3-19 Temperature retrieval error with 95% confidence interval (red). The error used for input was based on thermal noise contributions and does not include atmospheric conditions, clock error, velocity/position errors, or multipath effects. It also does not include averaging performed in post-processing software. 78

4-1 Earth atmosphere absorption spectrum for short wave infrared wavelengths 82

4-2 Number of setting occultations between pairs of satellites in varied orbits 83

4-3 Geographical location of setting occultations for (top) a prograde/retrograde pair of satellites and (bottom) a mid-latitude and sun-synchronous satellite 84

4-4 Histogram and CDF of tangent height rates during setting occultations for several dual-satellite configurations 85

4-5 Histogram and CDF of access range during setting occultations for several dual-satellite configurations 86

4-6 Diagram of intersatellite laser occultation through layers of the atmosphere 87

4-7 Elevation angle from the transmitting satellite (nadir = 0 degrees) for tangential heights of interest 88

4-8 Refractive Structure Parameters for several models. We assume a Hufnagel-Valley model modified with the Gurvich correction for upper altitudes [139] 89

4-9 Coherence Length for an Intersatellite Crosslink as a Function of Tangential Height. The dotted line denotes the altitude below which we want to sound. 90

4-10 Greenwood Frequency (and Tyler-Tilt Removed Frequency) as a function of Tangential Height. The dotted line denotes the altitude below which we want to sound. 91

4-11 Wavefront fitting error for different mirror architecture options. Below 5 km (dotted line) is the optimal desired sounding depth 92

4-12 Strehl ratio from fitting error only for different sizes (number of actuators) of MEMS deformable mirrors. Below 5 km (dotted line) is the optimal desired sounding depth 94

4-13 Strehl ratio from temporal error as a function of tangential height. Temporal error dominates the system in the troposphere, making sounding at low altitudes challenging. 95

4-14 Earth atmospheric reflection absorption for short wave infrared wavelengths [141] 96

4-15 Example architecture of a coronagraph. A Telescope is configured in a 4f system and on-axis light is blocked at the focal plane by a small opaque spot, allowing dimmer light from an off-axis object to reach the detector. Adaptive from [141] 99

4-16 Speckles and spider diffraction on an occulted star with a binary companion (Adapted from [141]) 100

5-1 Optical layout of the 2U adaptive optics characterization payload. Blue: light path to the wavefront sensor (mirror characterization and closed loop demonstration). Green: light path to the focal plane sensor (closed loop demonstration). 110

5-2 Requirements flow for the Shack Hartmann sensor design. Final design decision variables are lenslet size and focal length, and detector pixels. 111

5-3 Requirements flow for external object observation and correction. The exposure time, platescale, and stability are the main driven design variables. 113

6-1 Laboratory Hardware Setup of CubeSat-Scale Wavefront Sensor . . . 120

6-2 Diagram of internal control structure (depicts both open and closed-loop paths) 122

6-3 Pictoral Representation of the Southwell Reconstruction Algorithm [142] 123

6-4 Hardware Setup for BMC Mini DM measurements 124

6-5 MetroPro software output for BMC Mini DM measurements 125

6-6 Side by side comparison of the Zygo interferometer surface measurement and the Shack Hartmann wavefront sensor for each Boston Micromachines Mini actuator poke. Each grid figure represents the entire surface of the mirror with one actuator poked, and the grid is laid out to reflect the position of each actuator 126

6-7 Influence functions of the BMC actuators as measured with a Zygo interferometer. Top: horizontal, Bottom: vertical. Each actuator is represented by a different colored dashed line. Each actuator exhibits a Gaussian-type influence function, but there is variability in the measured performance of each actuator 126
6-8 Influence functions of the BMC actuators as measured with a Zygo interferometer. Top: horizontal, Bottom: vertical. Each actuator is represented by a different colored dashed line. Each actuator exhibits a Gaussian-type influence function, but there is variability in the measured performance of each actuator 127
6-9 Quiver plot showing measured spot deviations from a theoretical flat wavefront. The overall spot deflections are typical of a defocused beam. 130
6-10 Deflection Curve (Voltage vs Stroke) for the BMC mini mirror [95] . . 132
6-11 Closed Loop Mirror Performance - First Measurement **Note: will be updated** 132
6-12 Closed loop mirror correction (left) before turning on the mirror (middle) after introducing aberrations (clear plastic sheeting) and (right) after 5 iterations of the algorithm. 133
6-13 Plot of the encircled energy over the control time. The control bandwidth is approximately 0.2 Hz. 134

List of Tables

1-1 Satellite Size Definitions [5] 3

1-2 Comparison of chosen nanosatellite science payloads 7

2-1 CubeSat Radiometer Mission Comparison 29

2-2 Thesis Contributions 47

3-1 Temperature error for a variety of noise sources based on the Kursinksi study of GPS-MET, with values specifically pulled for MiRaTAs altitude range of interest [27]. The conditions are: Thermal error, 1 s SNR(W) = 5e4; Local multipath, 10 mm rms spread over 0.01 Hz; Horizontal refractivity structure, along track from simulation and horizontal motion of ray path tangent point from tropospheric and stratospheric climatologies near 30S for June-July-August; Ionosphere error, daytime, solar maximum conditions; Abel boundary error, 7 % in α, 5 % in H_ϕ; Hydrostatic boundary error, 5 K; Tropospheric water vapor, 0 latitude with 8 km vertical correlation length 70

5-1 DeMi Optical Payload Experiment Summary 105

5-2 Experiment traceability for open-loop mirror characterization 106

5-3 Experiment traceability for closed loop wavefront correction with the internal source 107

5-4 Experiment traceability for closed loop wavefront correction with an external source 108

5-5 Science Traceability for high-level DeMi mission goals 109

5-6 Requirements on the spacecraft from the two experiment configurations on DeMi 115

7-1 Thesis Contributions 138

Chapter 1

Introduction

Nanosatellites are becoming increasingly important to Earth-based observation and atmospheric characterization. CubeSats in particular are improving in capability [1], and small-satellite specific launch capabilities are providing realistic opportunities for constellations of such satellites to be deployed [2]. The 2007 National Academy of Sciences Decadal survey calls out the importance for improved weather monitoring and a need for "increased accuracy, reliability, and duration of forecasts with finer spatial and temporal detail for a wider array of weather variables"[3]. Measurements of interest include all-weather atmospheric sounding with 15–30 minute revisits and 25 km ground resolution, radio occultation measurements at 200 m vertical resolution with ~2500 measurements globally per day, and overall increases of global composition and pollutant measurements. There is both a scientific and commercial interest in remote sensing, and several start-ups have based their operations on generating data for interested end users (agriculture, government, military, scientific) using constellations of micro- and nanosatellites [4].

Small satellites and nanosatellites, specifically CubeSats, offer the opportunity to improve global measurements. Constellations of small satellites in low earth orbit (LEO) can enable global coverage and improved spatial and temporal resolution compared with large monolithic satellites in higher orbits, though typically at the expense of reduced precision or accuracy.

CubeSats are an active area of research and development, and recent years have

seen significant improvements in the capabilities and applications of CubeSat platforms in both engineering and scientific capacities. Nanosatellites are useful for both science applications and technology demonstrations. In this thesis we address both uses of nanosatellites in the improvement of atmospheric sensing and characterization.

1.1 Motivation - Nanosatellites for Atmospheric Characterization

Nanosatellite payloads, such as radiometers, radio occultation receivers, and lasers have applications for atmospheric sensing observations that improve the state of the art and contribute to global needs such as near-real-time weather forecasting, disaster monitoring, and assessment of climate trends. Weather and climate have a significant impact on global transportation, economy, and overall quality of life.

1.2 State of the Art and Gap Identification

1.2.1 CubeSat Capabilities

Space-based systems offer a unique platform that can provide persistent coverage over a wide region of the Earth with different operational constraints than ground-based sondes or airborne systems. Small satellites, like CubeSats and other sub-100 kg satellites, have been increasingly popular as platforms for remote sensing technology demonstrations with evolution toward operational missions. These small satellite platforms offer faster development time, higher acceptable risk, and reduced cost relative to large monolithic systems. These features offer a significant benefit to stakeholders if miniaturized payload performance meets mission objectives, especially as part of a constellation or cooperative measurements. Large constellations of small satellites may be able to provide the temporal resolution of GEO missions with the spatial resolution of LEO missions.

Small satellites are placed in one of several categories ranging from femtosatellites

Table 1-1: Satellite Size Definitions [5]

Name	Mass Category
Minisatellite	100 + kg
Microsatellite	10 - 100 kg
Nanosatellite	1 - 10 kg
Picosatellite	0.01 - 1 kg
Femtosatellite	0.001 - 0.01 kg

(less than 10 g) to microsatellites (up to 100 kg) as summarized in Table 1-1. These satellites are generally launched into space as secondary or auxiliary payloads.

In this work we focus on a specific class of nanosatellites known as CubeSats. CubeSats are defined in units (U's) of 10 cm $\times$ 10 cm $\times$ 10 cm cubes. The first CubeSat launched in 2001 [1]. The majority of applications up to 2012 were allowing students and young professionals easy access to space and hands-on space systems design. Since then, hundreds of these nanosatellites have launched, with 132 launched in 2014 alone [6].

CubeSats are advertised as cheaper to design, build, and launch than traditional satellite systems. Typical design timescales for CubeSats vary between 1-3 years [7] (with some designs turned around within a matter of weeks [8]). The use of commercial-off-the-shelf (COTS) components reduces the amount of in-house design, customization, and fabrication equipment required to produce CubeSats. CubeSats can be launched at significantly reduced costs, as they typically fly as secondary and auxiliary payloads on launch vehicles already commissioned for other missions. Launch costs are reduced from millions of dollars to hundreds of thousands of dollars. NASA offers a program for academic institutions called the Educational Launch of Nanosatelites, and missions selected through this program are offered launch opportunities at no cost to the satellite developers [9].

The popularity of COTS components has fostered an entire industry of small-satellite component providers and bus manufacturers. Communications systems, attitude determination and control units, and power subsystems are common components available [10], and there are companies that offer buses to integrate with payloads of

choice (Pumpkin, Tyvak, BCT, and Clyde Space).

There is also a business case in selling data generated from these CubeSat platforms. Several start-up companies such as Planet Labs, PlanetiQ, Spire, Skybox, GeoOptics, etc. have grown out of this concept, offering imaging or sensing data from future constellations of nano/microsatellites [11].

There are other advances in electronics and manufacturing and trends in platform volume that will grow the capability of future CubeSats [10]. Already, 3D printing enables more complex components to be fabricated easily, more quickly, and with less mass than machined metal components [10]. Plug and play technologies will further reduce cost for small satellites. There is also growing interest in 6U and 12U CubeSat platforms. These have more volume and mass than 3U CubeSats, leading to more available power, more capable subsystems (such as communications and attitude control), and more room for payload accommodation. Only two 6U CubeSats have been launched to date, but over 50 are planned for launch in the next three years. Advances in miniaturization of electronics and sensors, enabled by the development of Microelectromechanical Systems (MEMS), have also improved measurement capabilities.

CubeSats are an increasingly viable scientific platform [2], and their simplicity and low mass make them good candidates for low earth orbit constellations. Projections show that future missions will see a dramatic increase in CubeSat scientific and observation applications, as illustrated in Figure 1-1.

Even with advances in electronics and platform capabilities, there are physical limits to what can be accommodated in the tight volume and mass constraints of a CubeSat [12]. Aperture size, power generation, pointing control, and downlink capabilities constrain the instruments that are feasible on such a platform. Deployable architectures or distributed systems can be used to alleviate some of these limitations on aperture (and also communications and power generation) but may require active elements to achieve proper alignment and calibration.

There are several types of Earth-observing instruments that are suitable for such a constrained environment and have been successfully demonstrated on orbit as shown

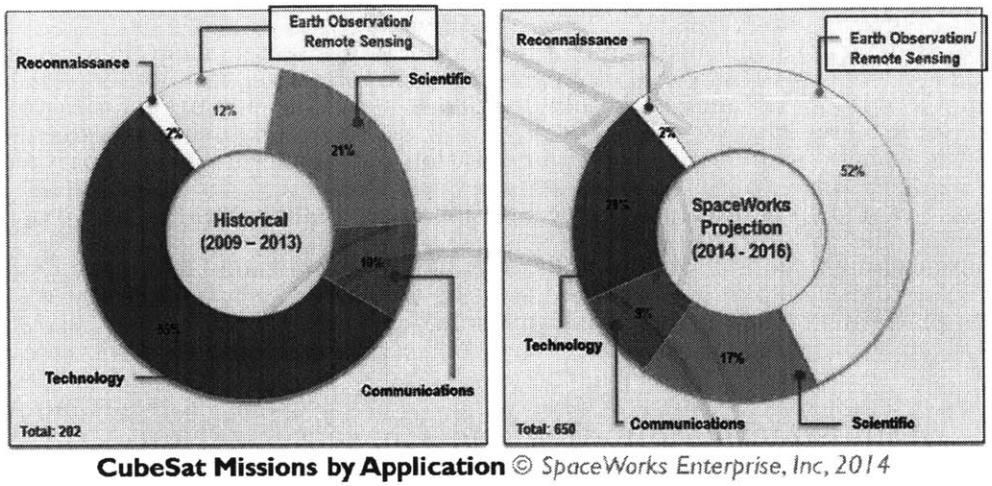

Figure 1-1: Projected CubeSat mission applications show dramatic increase in scientific and remote sensing fields

in the results of a 2012 survey of state of the art capabilities performed by Daniel Selva [13]. Payloads deemed immediately feasible or possible with some technology development by that study include:

- Atmospheric chemistry instruments
- Atmospheric temperature and humidity sounders
- Earth radiation budget radiometers
- Gravity instruments
- Multi-spectral visible/IR radiometers
- Multi-spectral passive microwave radiometers
- Multiple direction/polarization radiometers
- Lightning imagers
- Magnetic field instruments
- Ocean color instruments
- Precision orbit determination

The payloads chosen for study in this thesis contribute to atmospheric sounding and characterization measurements —temperature, humidity, pressure, composition

—based on near-term interests and utility in obtaining better atmospheric understanding of both Earth and Earth-like exoplanets. We develop approaches to improve atmospheric sounding and characterization with nanosatellites using passive microwave radiometers, atmospheric occultation measurements, and adaptive optics. We consider applications for nanosatellites as both scientific and technology demonstration platforms to enable improved atmospheric measurements.

1.2.2 Atmospheric Sounding and Characterization

We look at characterizing atmospheric sensing and characterization on nanosatellites for three applications: microwave radiometry, atmospheric occultation, and exoplanet direct imaging. We focus on atmospheric sensing and characterization through observations in two different regimes in the electromagnetic spectrum: infrared and radio/microwave. Each of these ranges of wavelengths contains absorption features that can be exploited to capture information about the atmosphere. Figure 1-2 shows what these absorption profiles look like in context of the electromagnetic spectrum.

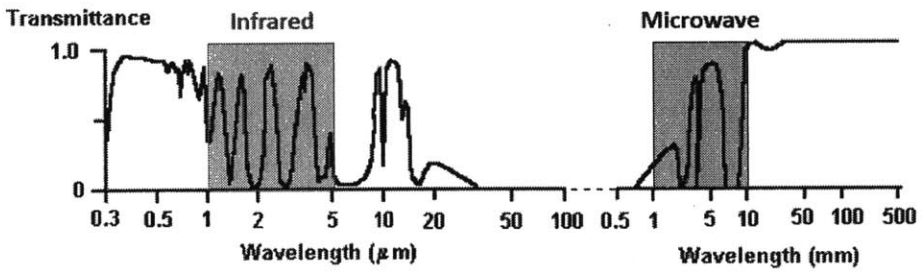

Figure 1-2: Atmospheric transparency across the electromagnetic spectrum. We focus on visible/infrared and radio/microwave wavelengths.

Table 1-2 shows the expected science return from the chosen payloads as well as the main challenges, benefits, and limitations associated with each. Each of the applications chosen can be improved through the use of nanosatellites, either using nanosatellites as platforms to fly instruments or using nanosatellites to demonstrate technology required to enable or improve measurements on a larger satellite platform.

Table 1-2: Comparison of chosen nanosatellite science payloads

Instrument	Science	Capabilities	Limitations	Nanosatellite Application
Microwave Radiometer	Temperature, water vapor pressure, cloud ice	All-weather sounding	Calibration, imaging through rain	Fly sensor
Radio Occultation	Temperature, electron density, water vapor pressure	All-weather sounding, inherently unbiased	Sounding to surface	Fly Sensor
Laser Occultation	Absorption Spectra	Identify compounds that absorb at IR wavelengths	Overcoming turbulence at low altitudes	Tech Demo
Direct Imaging	Reflection spectroscopy	Sound deeper into atmosphere	High-contrast imaging, platform stability	Tech Demo

1.2.2.1 Microwave Radiometry

Microwave radiometers have traditionally been flown on very large weather satellites [14], but recent research and development has led to miniaturized sensors that fit on nanosatellite platforms with comparable performance to existing systems [15]. Microwave radiometers are capable of measuring atmospheric pressure, temperature, water vapor content, and cloud water and ice content [16].

The current state of the art for weather sensing satellites with microwave radiometers includes instruments like the Advanced Technology Microwave Sounder [17], the Advanced Microwave Sounder Unit (AMSU) [18], and the Microwave Humidity Sounder (MHS) [19]. These instruments are over 50 kg in mass and consume tens of watts. They are able to sample across multiple bands and tens of channels, and the internal blackbody calibration sources allow for measurement accuracy to sub-K levels [17]. As existing weather satellites age and there is a push for improved spatial and temporal weather measurements [20], recent research has been focused on developing miniaturized microwave radiometers to fly on constellations of small satellites [21].

Limb-sounding passive microwave sounding instruments can collect information on temperature, water vapor, cloud ice, and atmospheric composition. Several instruments have flown, including MLS on the AURA mission [22], and the 2007 Earth Science Decadal recommended several more similar instruments on missions such as PATH [23] and GACM [24].

1.2.2.2 Atmospheric Occultation

Occultation measurements for atmospheric characterization are made when a transmitted signal passes behind the Earth with respect to the receiving satellite. The electromagnetic signal is refracted or attenuated as it passes through the Earth's atmosphere. Analyzing the received signal yields information on the thermophysical properties and composition of the atmosphere. This concept is illustrated in Figure 1-3.

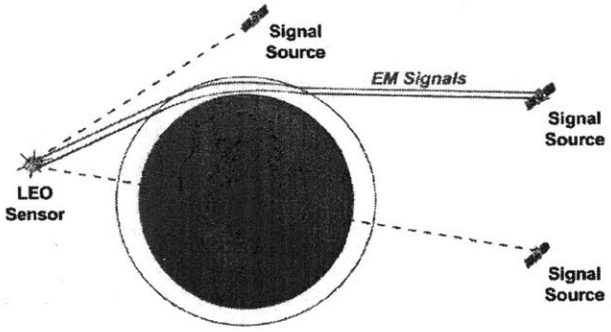

Figure 1-3: Occultation sensing techniques measure the interaction of electromagnetic waves with the atmosphere to determine atmospheric properties [25].

Radio occultation with the Global Positioning System (GPS) has been used for decades to do remote atmospheric sounding. The signal from a Global Navigation Satellite System (GNSS) satellite, often a GPS satellite, is tracked as the positioning satellite sets with respect to a receiver on a satellite platform in Low Earth Orbit. As the electromagnetic signals interact with the changing density (refractivity) gradient in the atmosphere, they will "bend,"and the path length will change incrementally. The relationship between the magnitude of signal refraction and the local atmospheric density gives information on the temperature and pressure of that volume of atmosphere.

GPS satellites transmit at different frequencies, and by sampling at multiple frequencies (e.g. L1 at 1575 MHz and L2 at 1228 MHz), effects from the ionosphere can be caliibrated out. The L1 and L2 signals can penetrate clouds and rain (unlike radiometers), so measurements made with GPS Radio Occultation (GPSRO) instruments can occur in all-weather conditions.

A key feature of GPSRO is long term stability of measurements that can be averaged to an accuracy of better than 0.1 K [26]. The resulting data are sometimes used for calibrating and characterizing bias of other sensors (radiometers, radiosondes, etc).

Since 1995, there have been many missions that have successfully flown GPSRO sensors utilizing receivers designed or built by the Jet Propulsion Laboratory. While

capable, these heritage receivers have large size, weight, and power requirements. Early missions used closed-loop tracking and single patch antennas, but as instrument technology became more advanced and data product requirements grew, large high-gain antennas and open-loop, single frequency tracking was implemented. The most notable of these receivers —TurboRogue (GPS-MET, PICOSat-9) [27], BlackJack (CHAMP, COSMIC, C/NOFS) [26] and TriG (COSMIC-2) —weigh up to 30 kg and draw up to 50 W of power [28] which works for microsatellites but is still too large for CubeSats or other nanosatellites. GPS receivers are now commonly flown on satellites in LEO for position and tracking information, and with minor modifications these can yield useful scientific information. State-of-the-art CubeSat GPSRO instruments can perform to <1 K in the neutral atmosphere at 10-20 km altitudes [26].

Occultation measurements at other (non-GPS) wavelengths in the microwave and infrared ranges can provide information on atmospheric composition as well as thermodynamic properties [16]. Measurements can be made at several different wavelengths that capture continuum and absorption behavior of different atmospheric constituents, such as methane, water vapor, and carbon dioxide. The intensity of the received signal can be used in conjunction with detailed models to estimate the abundance of different atmospheric molecules. Bending angle measurements may also be possible with advanced pointing control systems and would enable the concurrent measurement of abundance and thermodynamic properties.

As the signal transmits through the atmosphere, turbulence, scintillation, and scattering will also affect the intensity of the received signal. Signal improvement can be made onboard with adaptive optics, enabling better measurements.

Several missions have flown atmospheric composition sensors using solar occultation measurements. Instruments such as Haloe [29], SciSat/ACE [30], SOFIE [31], MIRIAM [32], and SCIAMACHY [33] were 8 - 120 kg, consumed up to 150 W, and generated several Mb of data. The instruments' size and complexity were driven by the objectives to measure vertical profiles of molecules (O3, HCl, HF, CH4, H2O, NO, NO2) as well as aerosol extinction, cloud ice particle distribution, and temperature and pressure profiles.

Retroreflectors, which exist on many satellite systems for laser ranging purposes, have been considered for atmospheric extinction measurements [34]. There are several challenges involved with this system architecture. A transmitter (either on a satellite or on the ground) sends a signal to a satellite equipped with a retroreflector such as a corner cube, and the reflected signal is received back at the transmitter's location. Because the signal has to travel through the atmosphere twice, there is substantial power loss due to atmospheric turbulence and beam spreading. The reflective properties of corner cubes as a function of incidence angle and time on orbit are uncertain [35] and would require precise calibration to yield reliable atmospheric extinction measurements.

Intersatellite links at radio and optical wavelengths are also useful from a communications standpoint. Constellation and cluster operation may depend on full-duplex intersatellite transceivers. Laser wavelengths offer increased throughput and datarates, but links through the atmosphere encounter similar scintillation and bending effects [36].

1.2.2.3 Exoplanet Detection and Characterization Methods

In addition to Earth sensing and characterization, micro- and nanosatellites are being built for exoplanet observations. Transit exoplanet detection can be implemented on a CubeSat platform [37], and CubeSats can offer on-orbit technology demonstration to enable space-based exoplanet detection on larger telescopes [38]. Direct imaging is a common exoplanet detection technique that requires a large aperture, and spectral information can be obtained from exoplanet observations in order to determine their composition [39]. Ground-based systems use adaptive optics to correct for atmospheric correction and can image planets at better than 10^{-6} contrast (planets that are six orders of magnitude dimmer than their parent stars). Imaging Earth-like exoplanets (10^{-10} contrast in regions closer to the parent star for a Solar twin) requires space-based telescopes above the effects of the atmosphere.

Even above the atmosphere, direct imaging missions with an internal coronagraph require fine wavefront correction to mitigate the effects of internal diffraction and

scattering in order to obtain the desired high-contrast measurements. Adaptive optics are used to correct high spatial frequency aberrations.

One of the advantages and future applications of direct imaging is to obtain reflection absorption spectra from exoplanets' atmospheres. Compared with transit methods, direct imaging has the potential to identify more targets and to generate spectra from deeper within the planets' atmospheres. Also, direct imaging can detect planets around any star system close to the Sun. Transits can only detect 0.5% of planets for Earth-like planets orbiting with a radius of 1 AU around sun-like stars due to the geometry required to be able to detect a transit event.

1.2.3 Adaptive Optics

Adaptive Optics (AO) is a method for real-time correction of wavefront distortions that may affect the performance of an optical system. For signals that pass through the atmosphere, a typical cause of wavefront aberration is atmospheric turbulence, which encompasses changes in the atmosphere due to temperature, pressure, wind velocities, humidity, and temporal changes. In space, wavefront control systems are needed to correct for the effects of diffraction, manufacturing imperfections, the changes in an optical system after surviving launch and existing in a varying thermal environment (both local to the spacecraft and throughout the orbit and as a function of pointing), and the structural and mechanical effects of actuators and the spacecraft attitude control system, such as jitter. A traditional adaptive optics system is illustrated in Figure 1-4.

Typically an adaptive optics system contains three main elements: a deformable mirror to change the wavefront of light propagating through the system, a wavefront sensor to measure distortion, and a control system to calculate the mirror deflection required to correct the wavefront [40].

Implementing active and adaptive optics on a nanosatellite platform is of interest to demonstrate and characterize MEMS deformable mirror (enabling technology) in space. Adaptive optics enable improvements in intersatellite links through the atmosphere, measuring the intensity and bending angle of these links (yielding atmospheric

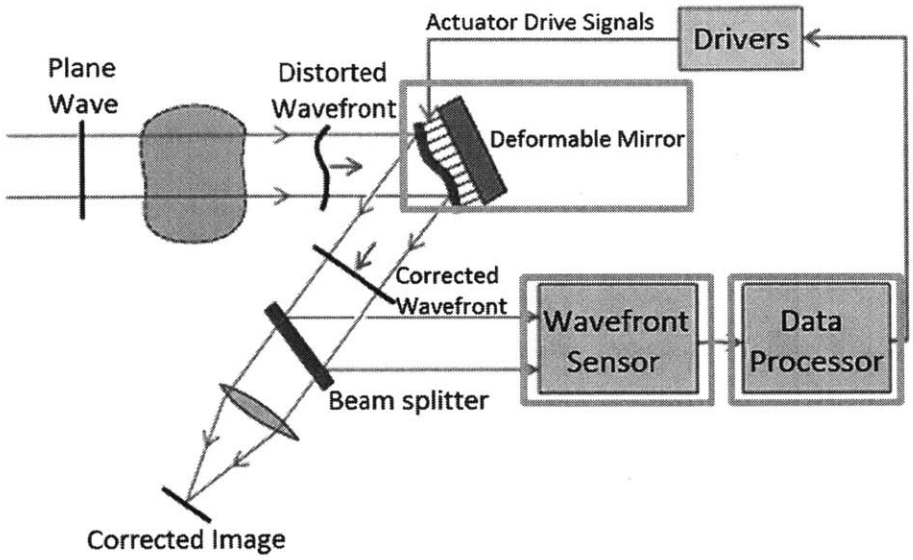

Figure 1-4: There are three main elements to an adaptive optics system: the deformable mirror, the wavefront sensor, and the control system.

composition, atmospheric thermophysical parameters). Improvements in intersatellite links also better crosslink communication, expanding the effective range for data transfer between satellites. Elements of adaptive optics systems are also useful in alignment corrections for deployed aperture concepts.

Deformable mirrors (DM) are a key part of adaptive optics systems, and existing mirrors have been shown to correct wavefront aberrations to better than nm levels in ground operation. Frequently-used DM options currently include Xinetics piezoelectric and PMN actuators, technology that is currently at NASA Technology Readiness Level 6. MEMS deformable mirrors offer improvements in mass, volume, and cost, but they are less developed for space applications [41]. While a nanosatellite platform is not suitable to achieve high-contrast imaging science, CubeSats offer a relatively low-cost, fast opportunity to space-qualify mission critical technologies. Flying adaptive optics systems on nanosatellite platforms paves the way for future flagship class missions or next-generation space telescopes, serving as technology demonstrations for larger platforms characterizing exoplanets with highly precise wavefront control

systems.

1.2.4 Ground Applications for Adaptive Optics

On the ground, wavefront control systems are designed to perform at high speeds and use mirrors with large strokes in order to compensate for atmospheric turbulence. A two-mirror woofer-tweeter (coarse-fine) wavefront control approach is frequently used where the woofer corrects slower, larger amplitude, lower-frequency components and the tweeter corrects faster, smaller-amplitude, higher-frequency components . There are several ground-based observatories that utilize adaptive optics systems, including (but not limited to) Keck I and Keck II [42], Palomar [43], and Lick [44], and the Advanced Electro-Optical System (AEOS) [39]. Additionally, ground stations such as the ESA Optical Ground Station employ adaptive optics for use in optical communication [45].

The adaptive optics system Gemini Planet Imager (GPI) was built for the Gemini Observatory to detect and analyze Jupiter-like exoplanets. It incorporates a woofer-/tweeter AO architecture. The tweeter is a Boston Micromachines (BMC) 64x64 array of electrostatic actuators with a continuous gold facesheet and 400 m stroke [46]. This platform required a custom deformable mirror mount to withstand the variable ambient temperature, gravity orientations, humidity, and dust associated with operations on a ground-based telescope. GPI received first light in November 2013 and has since obtained several observations and spectra of exoplanets [46].

Another ground-based observatory in planning is the Thirty-Meter Telescope (TMT), which is the first ground-based telescope being designed with adaptive optics incorporated from the start. The proposed Planet Formation Imager would incorporate extreme adaptive optics in order to enable direct imaging and spectroscopy of Jupiter-like exoplanets [47].

1.2.5 Space Applications for Adaptive Optics

The most relevant recent effort to demonstrate the use of deformable mirrors in space was the Boston University PICTURE (Planet Imaging Concept Testbed Using a Rocket Experiment) [48] sounding rocket experiment, which flew with a BMC MEMS DM for high contrast wavefront control in 2007. The rocket attitude control system provided 627 milliarcseconds (mas) RMS body pointing and the fine pointing system successfully stabilized the telescope beam to 5.1 mas RMS using an angle tracker camera and fast steering mirror. Due to a communications system malfunction all MEMS DM performance data were unfortunately lost on PICTURE-A. Picture-2 (sounding rocket) did fly successfully, and PICTURE-C (balloon payload) is planned for launch in 2017 [49]. The total sounding rocket observing time is on the order of 5 minutes (320 seconds) which is not sufficient to demonstrate the long-term, accurate calibration and operation of a MEMS DM over the multiple hours of integration necessary for building confidence in robust on-orbit deformable mirror performance.

Another relevant effort was the South Korean MEMS Telescope for Extreme Lightning (MTEL), which was launched for operation on the ISS in 2009 [50] [51]. This mission used a one-axis torsional spring tilt single actuator trigger mirror and a two-axis tip-tilt electrostatic comb-drive 8 x 8 MEMS mirror array. However, the actuators in this mirror are very different from the high actuator count MEMS DMs needed for wavefront control for a high contrast imaging application. The MTEL trigger mirror operated in tilt only with two possible positions (on/off), and the tip-tilt torsional spring array was for selective beam directing rather than precise wavefront control.

There is interest in flying internal coronagraph missions in space [52]. The WFIRST mission [53] will fly an internal coronagraph and 48 $\times$ 48 Xinetics deformable mirrors to enable high contrast imaging. A study was done on the design of a probe-class mission with an internal coronagraph (a sister study looked at an external occulter), Exo-C [54], which baselined the same electrostrictive mirror as WFIRST. NASA Ames has proposed several smaller-class missions to directly image exoplanets [55] [56] with MEMS deformable mirror technologies.

Future space missions, especially on volume and mass constrained platforms, would benefit from MEMS deformable mirrors. There have been several efforts to space qualify MEMS devices, but so far no long-term on-orbit operation has been demonstrated. A nanosatellite technology demonstration would help to validate and bring flight heritage to MEMS deformable mirror systems that would enable current and future space missions. Currently MEMS deformable mirrors do not meet the performance requirements to achieve high-contrast imaging at 10^{-10} levels. Improvements in printthrough and scalloping, more gentle influence functions, and smaller actuator pitch are needed before MEMS deformable mirrors provide correction performance to rival piezoelectric and electrostrictive devices [54].

1.3 Research Contributions

The goal of this thesis is to develop payload concepts and mission architectures for atmospheric sounding and characterization using nanosatellites in both science and technology development capacities. We focus on payloads that have flown or are planned to fly on nanosatellite platforms, such as microwave radiometers, GPS radio occultation receivers, and laser transceivers. We develop new methods for improving the science yield from nanosatellite microwave radiometer missions by using collocated GPS radio occultation measurements to help calibrate the microwave radiometers.

We also identify the need for space-based high spatial frequency wavefront control systems for atmospheric sounding using laser occultation as well as for use on space telescopes for exoplanet atmospheric characterization. We design a nanosatellite payload to demonstrate the performance of new MEMS wavefront control technology in space, enabling future missions with enhanced imaging capabilities. We prototype the nanosatellite wavefront control payload and demonstrate its performance by laboratory experiment.

The research questions and contributions addressed by this thesis are:

- How can we improve the accuracy of atmospheric sounding with microwave radiometers on CubeSats?

- Analyzed coverage, revisit and performance metrics for constellations of nanosatellites hosting microwave radiometers and GPS radio occultation receivers, and identified that high-inclination orbits are optimal for global occultation measurements. Hundreds of global GPSRO opportunities per day are possible, and six satellites per orbital plane yield revisit rates under one hour.

- Developed a model to predict the number of overlapping measurements that will occur between a microwave radiometer and GPS radio occultation sounder and showed that they meet (and exceed) the calibration requirement of one opportunity per day.

- Developed a method for assessing nanosatellite instrument GPSRO temperature errors to confirm they are below the level needed for radiometer calibration and demonstrated that commercial GPSRO receivers should be able to provide profiles with errors sufficient for calibrating a radiometer. The design requirements are 0.5-1.5 K GPSRO temperature precision to enable calibration of a microwave radiometer to 0.25 K absolute accuracy, and we show a 95% confidence of 0.1-1.7 K precision due to thermal noise for a commercial receiver.

- Can CubeSats demonstrate new wavefront control technologies for atmospheric characterization?

  - Analyzed coverage, revisit, and performance metrics for intersatellite links between two nanosatellites, and identified that dual-satellite systems comprised of one satellite in a polar orbit and one satellite in a mid-inclination orbit yield the most globally-distributed measurements.

  - Characterized atmospheric turbulence for a crosslink laser occultation measurement architecture and identified an application for wavefront control technology on space platforms to enhance atmospheric characterization of Earth using laser occultation.

- Designed a nanosatellite wavefront control payload and developed mission architecture to demonstrate and characterize MEMS deformable mirror technology in the space environment.
- Built and prototyped a laboratory experiment of the payload and performed preliminary performance validation (open-loop mirror characterization to better than 100 nm precision and static closed-loop error correction).

1.4 Thesis Organization

In Chapter 2 we go into more depth on the background and latest research in atmospheric sounding and characterization with a focus on microwave radiometry, atmospheric occultation, and wavefront sensing. We present the current state of the art and areas for potential improvements on nanosatellite platforms.

In Chapter 3 we look specifically at the use of nanosatellites for atmospheric sounding using radiometers and GPS radio occultation sensors. We show how constellations enable temporal and spatial resolution measurements specified in the decadal survey and how the orbit of the nanosatellite and architecture of the constellation affects the performance measurements. We also assess the use of GPS radio occultation as a calibration source for microwave radiometers and other weather sensing instruments based on the requirements of the MiRaTA mission. We have developed a model to calculate the expected temperature precision based on several receiver noise factors within the system.

In Chapter 4 we present methods to obtain atmospheric characterization measurements both of Earth (using intersatellite links for laser occultation) and of exoplanets (spectrometry from reflected light). We motivate the utility of adaptive optics systems to enhance Earth and exoplanet atmospheric characterization.

In Chapters 5 and 6 we present the design and laboratory validation of a CubeSat-scale wavefront sensor and control system intended for characterizing a MEMS deformable mirror in orbit. This payload, with minor modifications, is suitable for

implementation in a laser-crosslink system to facilitate and improve measurements from intersatellite links through the atmosphere.

Chapter 2

Nanosatellite Atmospheric Sounding Technology: Literature Review

We analyze how to advance the state of the art in atmospheric sounding and characterization using CubeSat platforms. The approaches to atmospheric sounding - microwave radiometry, radio occultation, laser occultation - can all be accomplished on a nanosatellite platform with current or near-term technology. With implementation of constellation architectures and novel operations, the quality of those measurements approach current operational state of the art systems with better spatial and temporal coverage. Figure 2-1 shows the three main research areas that intersect in this work.

Each area of the Venn Diagram is described in more detail in the following sections. Section 2.1 discusses the nanosatellite requirements for each of the three atmospheric sounding missions. Section 2.2 discusses microwave radiometry and challenges of implementation on a CubeSat platform. Section 2.3 discusses atmospheric occultation and methods used to improve sounding in the lower atmosphere in both radio and optical wavelengths. Section 2.4 discusses the relevance of Exoplanet atmospheric characterization and how CubeSat technology advancements can also be used in this application.

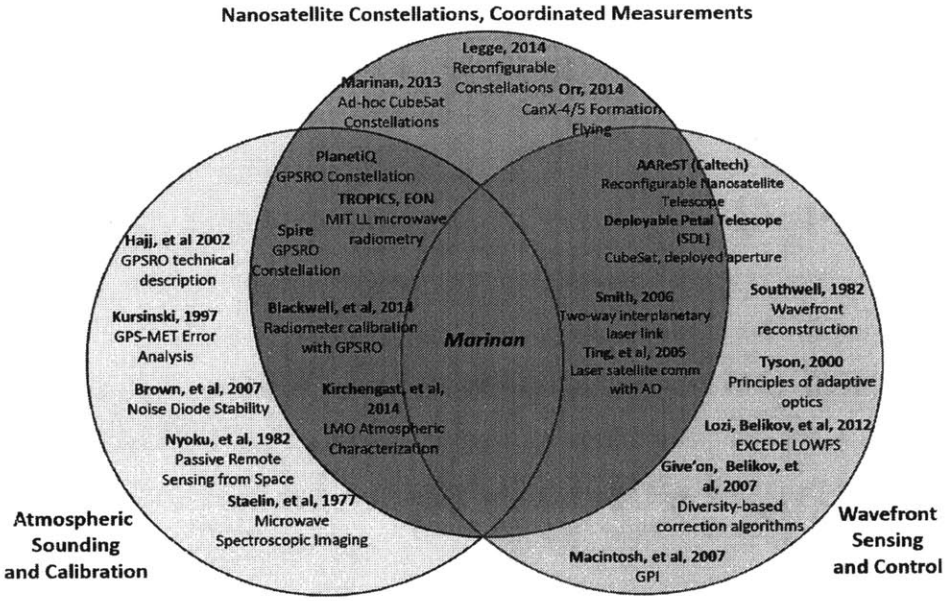

Figure 2-1: Area of contribution in context with major areas of research

2.1 CubeSat Requirements to Support Atmospheric Sensing

While there are still performance limitations on nanosatellite buses (pointing, aperture size, power generation, datarate), the requirements for radiometry, radio occultation, and intersatellite links are within the current or near-term capabilities.

2.1.1 Structure and Accommodation

Both optical and microwave imagers are governed by a wavelength (*lambda*)–dependent relationship between aperture diameter D and resolution (Equation 2.1). Larger apertures enable better resolution, but CubeSat size constraints limit the possible size of an external aperture.

$$R = 1.22 * \frac{\lambda}{D} \tag{2.1}$$

A 9-cm aperture corresponds to a ground resolution of 5-10 m depending on the spacecraft altitude for an optical imager, while a 9-cm aperture corresponds to a 2.5-

5.6 degree full width halfpower beamwidth (25 –50 km ground distance) depending on the wavelength for a radiometer. For a laser transmitter, a 9 cm aperture corresponds to a 35.8 μrad diffraction-limited 1550 nm beam [57]. Radio occultation mission performance depends on the antenna gain (rather than an aperture), requiring at least 10 dBi to achieve competitive measurement precision. High-gain patch antennas are inherently thick, and CubeSats offer limited surface area on which to mount them.

2.1.2 Power

The power subsystem comprises power generation, storage, and distribution for a given mission. Depending on the supporting subsystems, the power requirements for the bus can reach levels of 25-30 W (assuming 3-axis attitude control and off the shelf radios). For remote sensing missions, payload power draw will be on the order of 5-10 W for radiometers and GPS receivers, and could reach up to 20 W for optical transmissions. Subsections 2.2 - 2.4 go into more detail on payload power numbers.

2.1.3 Data

Science missions (and business models) are driven by the data generated onboard the spacecraft, so downlinking relevant information is critical to the success of these missions. Data throughput and latency are both parameters that must be considered for science and observation missions.

Sampling is one of the main drivers for onboard data generation. The more measurements taken, the better the resolution and precision of that data. It is not uncommon for scientific payloads to generate data at Mbps rate. With compression and selective sampling those rates can be decreased to tens of kpbs, but at the cost of data quality and measurement opportunities. With compression and selective sampling rates, radiometers can generate less than 20 kbps [15]. GPS radio occultation instruments sample at at least 50 Hz and, depending on the number of GPS satellites in the field of view, can generate up to 118 kbps.

Timeliness of data downlinked is also crucial for applications like disaster moni-

toring and weather sensing and requires a global ground network. A single satellite in LEO with one ground station can see blackout periods of 12 - 18 hours between groundpasses.

2.1.4 Pointing

Spacecraft attitude knowledge and stability is another requirement that varies with science application. For radiometry and radio occultation, spacecraft pointing to one degree or better is sufficient to achieve most CubeSat science goals. Imaging and optical communications requirements are on the order of microradians (depending on aperture size), though the spacecraft pointing requirement can be relaxed if a staged control system is used [58].

An important consideration for imaging systems is spacecraft jitter. High frequency jitter is caused by vibration induced by moving components on the spacecraft, while low frequency disturbances are typically caused by the external environment - drag pressure, gravity gradient, solar radiation pressure, and magnetic torque. The most common form of jitter on spacecraft is from reaction wheels [59], but it can also occur from any component that causes vibrations, such as propulsion, deployables, mechanisms, and active thermal management. Specific jitter requirements are mission-dependent, but for imaging systems, any spacecraft motion with timescales smaller than the camera exposure time will cause the image to blur.

2.1.5 Positioning

Positioning is important for geolocating science measurements, knowing where to point a high-gain groundstation antenna during an overpass, and coordinating inter-satellite links in constellation or formation flying satellites. For a high-gain antenna such as the Wallops 18-m dish, the satellite position must be known to 20-30 km depending on the orbit and the power and gain pattern of the on-board antenna. Geolocation requirements depend on the footprint of the sensor but are on the order of 10 km (corresponds to a 25 km ground distance from a 400 km orbit) in low-earth

orbit for a 9 cm aperture radiometer. Antenna pointing depends on the beamwidth of the groundstation. Intersatellite communication requires that the receiving satellite aperture be within the beamwidth of the transmitted signal. For a 35.8 μrad beamwidth at a 1000 km range, this corresponds to a position requirement of 2.2 km.

2.1.6 Thermal Management

Satellites in low earth orbit that periodically go through periods of eclipse and full sunlight can see very large temperature swings over their lifetime. The thermal environment on a spacecraft is important for both component operation and science measurements. Radiometers and GPS radio occultation receivers are sensitive to thermal noise and thermally-induced gain drift:

$$\Delta T_{RMS} = T_{SYS} * \sqrt{\frac{1}{B\tau} + \frac{\Delta G^2}{G}} \tag{2.2}$$

The thermal environment must be well-characterized if not actively controlled. IR imaging systems are extremely sensitive to thermal noise, and some detectors require active cooling to keep their operational temperature less than -20 deg C, sometimes much colder.

Thermal stability is a requirement from an alignment perspective for imaging systems. Thermal gradients cause the spacecraft to warp, introducing astigmatism and other aberrations, such as speckles for imaging systems. This is especially important to mitigate for high contrast imaging telescopes.

2.1.7 Global Coverage Considerations

There has been substantial research to date on constellation architectures, including optimized constellation configurations, reconfigurable satellite constellations, and ad hoc constellation configurations. Constellations of tens of nanosatellites in Low Earth Orbit are sufficient to obtain decadal-level temporal resolution [60].

Satellite constellations are typically designed to optimize coverage over specific areas or to improve global revisit times. Constellation architectures have been studied

and optimized for decades, e.g. [61] [62] [63] [64] [65] [66]. For optimized architectures, continuous worldwide visibility of one location can be achieved with as few as five satellites, with each in a separate orbital plane, assuming a horizon-to-horizon field of view [67]. In addition to the number of satellites and orbital planes, for Earth-observing missions, the effective sensor field of view also determines the coverage, revisit time, and optimal configuration.

There are several common constellation architectures [66] [68], including

- Geosynchronous —three to five satellites in GEO providing worldwide coverage (not feasible for nanosatellites);
- Streets of Coverage —polar orbits with satellite right ascensions of ascending node (RAAN) spread evenly across one hemisphere;
- Ellipso —various elliptical orbits are used to optimize coverage over a specific region or for a specific time of day;
- Polar Non-symmetric —satellites in polar orbits with varying rotational spacing designed to optimize coverage over a specific region;
- Walker/Rosette —satellites in individual rotationally symmetric orbital planes with identical altitudes and inclinations; and
- String of Pearls (A-Train) —multiple satellites in same orbital plane.

There are several nontraditional constellation and network architectures that have been studied, including reconfigurable constellations [69] and ad-hoc constellation opportunities [70]. Both these and other constellation studies have typically been for earth-looking sensors.

2.2 Microwave Radiometry

Microwave radiometry is a field of remote sensing concerned with measuring the radiation from the atmosphere at microwave wavelengths, and it is used primarily

for weather sensing and climate monitoring. One of the advantages of using microwave over other wavelengths is that clouds are transparent to microwave signals, so measurements (unlike optical imaging) can be made relatively in nearly all weather conditions. The data products include temperature, pressure, water vapor content, cloud ice, ocean ice, and the atmospheric radiation budget.

2.2.1 Measurement Principles

Microwave radiometers on orbit collect thermal radiation reflected from the surface of the Earth and the atmosphere. An antenna receives the signal and then supporting electronics amplify and detect this radiation within a certain frequency band. This received signal is used to retrieve geophysical parameters of the atmosphere, which can inform meteorological modeling [71]. Atmospheric constituents have different absorption features (see Figure 2-2), and sampling at different frequencies permits the observation of different atmospheric constituents, which probe different depths of the atmosphere; for example, the 118 GHz microwave molecular oxygen line is very good for determining temperature distribution [72].

2.2.2 CubeSat Microwave Radiometry Missions

CubeSat missions such as PolarCube [74], the Microsized Microwave Atmospheric Satellite (MicroMAS) [15], RACE [75], RAVAN [76], ICECube [77], and the Microwave Radiometer Technology Acceleration (MiRaTA) [78] have housed 1U (10 cm x 10 cm x 10 cm) sized radiometers. Future missions are planned (EON) for even more capable radiometer payloads on larger CubeSats and small satellite platforms [21]. Table 2-1 shows a size and performance comparison for representative flown or planned radiometer missions.

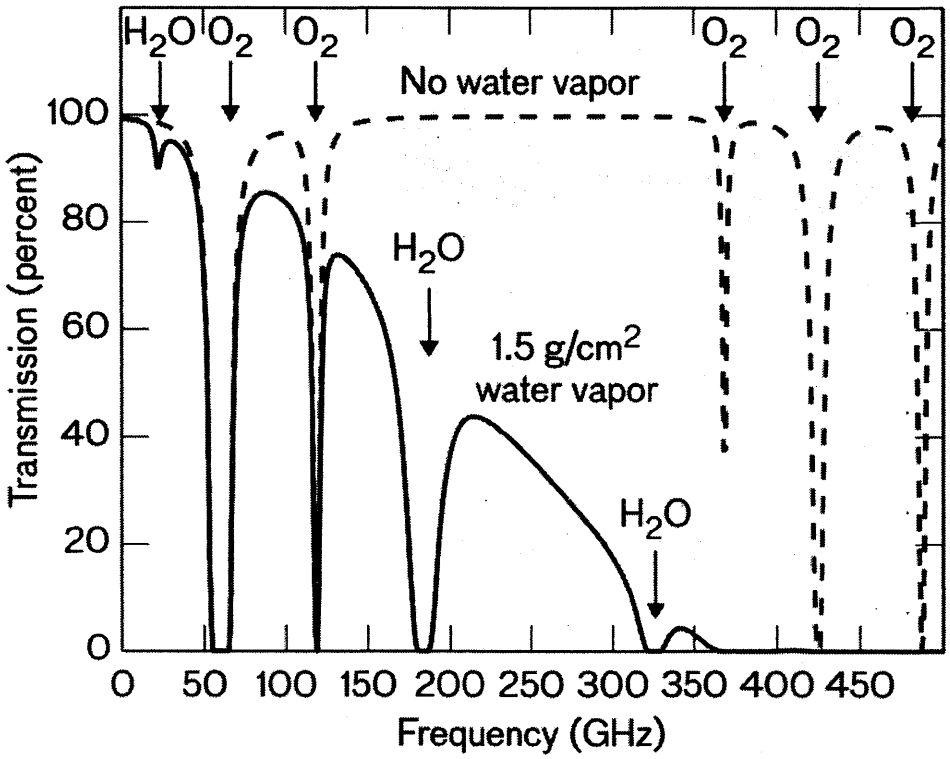

Figure 2-2: Microwave and millimeter wave absorption spectrum for dry air and air with water vapor [73]

Table 2-1: CubeSat Radiometer Mission Comparison

Mission	Size	Mass (kg)	Power (W)	Sensitivity (K)	Accuracy (K)	Bands	Channels	Design Lifetime
PolarCube	1.5U	¡2				1	8	Months
MicroMAS-1	1U	0.95	2.5	0.1-0.6	1.0	1	9	6 months
MicroMAS-2	1U	1.00	4	0.1-0.6	1.0	4	13	1-2 years
MiRaTA	1.5U	1.02	4	0.1-0.6	1.0	3	12	1-2 years
RACE	1.5U	1.5	<1.5			1	3	6 months
RAVAN	1U	1	1.9					6 months
IceCube	1.3U	1	11.2	0.25	2	1	1	1 year
AMSU	0.76 m	154	150	0.2-0.8	0.5	6	20	10-15 years

2.2.3 Calibration and Coverage Challenges

CubeSat-sized sensors may be moderately less capable than the existing large systems due to the current lack of onboard calibration sources and reduced band and channel sampling. Some antenna apertures on systems such as AMSU and MHS are comparable in size to those on CubeSats, ranging from 8–17 cm. More recent CubeSat-sized radiometers are being developed with the ability to sample at multiple bands, and novel calibration techniques are being developed to allow measurement accuracy better than 1 K [79], [17].

2.3 Atmospheric Occultation

Atmospheric occultation is a measurement technique that uses electromagnetic signal interaction with the Earth's atmosphere to infer thermophysical and compositional characteristics of the atmosphere. Occultation measurements use a number of sources, including solar, lunar, stellar, navigation satellites, and intersatellite crosslink communications. Scientific measurements obtained from occultation opportunities include neutral atmospheric temperature, density, pressure, water vapor content, and gas composition, as well as ionospheric density and electron content.

Occultation measurements offer several desirable characteristics. Regardless of source, occultation data products are self-calibrated, can be made with high accuracy and vertical resolution, can be obtained globally, and (if using radio signals) offer all-weather capability. These properties make occultation data valuable to many end-users and disciplines [25]. In this thesis we look at two regimes of occultation-based measurements: those observed in radio frequencies and those observed in optical/infrared frequencies.

2.3.1 Radio Occultation

Radio occultation commonly takes advantage of any Global Navigation Satellite System (GNSS) satellites as constantly-transmitting sources of radio waves at multiple

frequencies. Receivers in LEO track the navigation satellites as they are occulted by the Earth. In this thesis, we focus specifically on Global Positioning Satellites (GPS) for our analyses.

2.3.1.1 Radio Occultation Measurement Principles

GPS satellites transmit at several separate frequencies, and receivers are commonly designed for L1 (1.575 GHz, 19 cm wavelength) and L2 (1.227 GHz, 24 cm wavelength) frequencies. Distance from the transmitting GPS satellite to a receiver can be measured in numbers of transmitted cycles (or waves). As a GPS satelite sets behind the Earth, the signal passes through the atmosphere, which is a refractive medium that delays the signal, effectively increasing the path length. This is illustrated in Figure 2-3. The receiver counts the extra cycles in the received signal, and state-of-the-art receivers can make this measurement with a precision better than 1 mm [80].

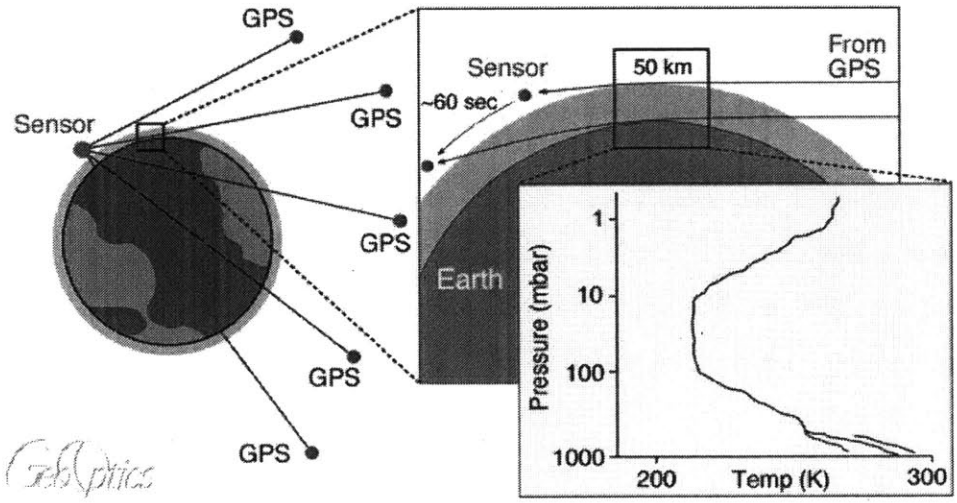

Figure 2-3: GPS radio occultation measures signal bending (elongation) through the atmosphere and retrieves temperature and pressure information. [80]

From the delay measurement, the angle by which the atmosphere bends the signal can be calculated. That bending angle is related to atmospheric refractivity, from which temperature and pressure in the neutral atmosphere and total electron content in the ionosphere can be calculated [81]. GPSRO measurements are made from the

top of the atmosphere down to the limb at 100–200 km vertical resolution, and the corresponding profiles are used in meteorological and climate modeling. GPS Radio Occultation (GPSRO) provides relatively uniform spatial/temporal coverage with an accuracy of approximately 0.1 K or higher, a precision of 0.05K or better, and a satellite-to satellite bias of less than 0.05 K [82].

2.3.1.2 CubeSat Radio Occultation Missions

There has been significant progress in the development, space qualification, and flight of miniaturized GPSRO sensors with focus on the ionosphere. In 2008, the first COTS sensor for GPSRO was flown on a nanosatellite, but unfortunately, due to spacecraft issues, no occultation products were obtained [83]. It should be noted that other nanosatellites have carried GPS receivers for position and navigation data since 2000 [84]. The first successful demonstration of a GPSRO sensor on a nanosatellite occurred in 2011 with the launch of the PSSCT-2 mission. PSSCT-2 contained the Compact Total Electron Content Sensor (CTECS) designed and built by The Aerospace Corporation. It successfully produced ionospheric TEC profiles [85]. Other CubeSat-sized sensors flown and under development include CTAGS (MiRaTA) [78], PolaRx2, FOTON [86], and Pyxis [28]. These receivers are on the order of 35–350 g and draw 1.2–5 W of power.

When considering replacements for existing monolithic weather-sensing satellites, there is interest in developing constellations of nanosatellites to provide weather products, especially utilizing GPSRO. Startups such as Spire, GeoOptics, and PlanetIQ are developing business models around this very idea [11]. The NOX payload on TET-1 used a commercial GPS receiver with only slight firmware modifications to obtain GPSRO measurements down to 7 km [87]. The MiRaTA system predicts similar in performance but is packaged for a smaller spacecraft volume, has slightly higher gain, and will sample at a 5 times higher rate. Capabilities demonstrated on the MiRaTA mission will inform future missions towards a constellation of CubeSats to provide global microwave radiometer and GPSRO measurements [79].

The NovAtel receiver [88] can have different tracking algorithms. The CTAGS

samples at 50 Hz when collecting occultation measurements and uses a dual-frequency receiver (L1 at 1575.42 MHz and L2 at 1227.60 MHz) which then allows removal of clock errors and the effects of the ionosphere in generating troposphere and lower stratosphere temperature profiles.

2.3.1.3 Lower Atmospheric Sounding Challenge

GPS radio occultation for ionospheric characterization has been successfully demonstrated on CubeSats [85], but neutral atmospheric sounding has not. Sounding deep into the atmosphere requires a high gain antenna, which typically requires a thick patch array or a deployable antenna. Both present challenges in volume accommodation given the tight structural and volume constraints, depending on the deployer [12]. As an added challenge, unlike most large instruments with a dedicated science GPSRO instrument and separate position, navigation, and tracking (PNT) system, a CubeSat GPSRO instrument typically serves both a science and a navigation purpose. The two can sometimes have competing requirements, particularly where the antenna is concerned. A GPS antenna designed for PNT application is as isotropic as possible to ensure that several satellites are within the field of view and that each satellite sees a similar gain profile. Conversely, a GPSRO antenna must be high gain to sound deep into the atmosphere.

Onboard processing capabilities also limit the effectiveness of GPSRO instruments. GPSRO receivers can operate in either a closed-loop or an open-loop fashion. Figure 2-4 shows the difference in lower atmosphere retrievals for open and closed loop operation on the CHAMP mission. The benefits of the open-loop tracking were largest at tangential heights below 10 km.

Closed loop algorithms lock onto a transmitting GPS satellite and 'zoom in'on the signal to reduce memory as the signal is tracked through the atmosphere. If lock is lost, it is very difficult to regain the signal. Open-loop tracking systems keep more information in active memory and are able to recover lost signals and provide more precise measurements. Current processing limitations make it difficult to implement open-loop tracking systems on CubeSats.

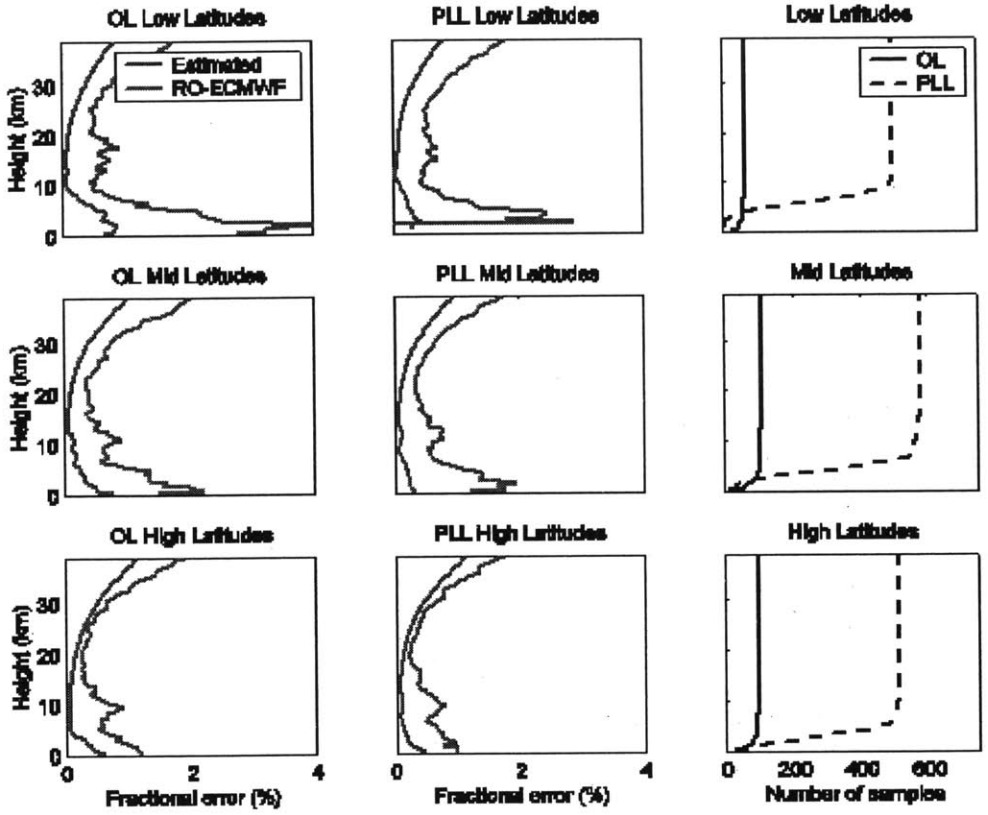

Figure 2-4: Difference in retrievals for open-loop and closed-loop tracking for the CHAMP mission

2.3.2 Laser Occultation

Optical signals (visible to infrared) transmitted through the atmosphere also experience bending, so in theory, optical occultations can provide the same atmospheric thermophysical parameters as radio occultations. In practice, however, measuring bending angles at optical and infrared wavelengths has not yet been done [89]. The expected bending through the atmosphere for an IR signal at the surface is 0.1 to 1 degrees, and it decreases exponentially as a function of height. The required pointing knowledge on both spacecraft would need to be at the μrad level with position knowledge better than 2 km. For an IR signal, that bending angle would be measured directly on the detector. Implementing optical bending angle measurements from an intersatellite crosslink requires the development of a transmitter and receiver with accurate orbit determination, accurate attitude determination and fine control, and feedback between the two satellites. Research is ongoing to enable high-accuracy pointing requirements for laser communications applications using a dual-stage pointing architecture [58].

Another limitation to bending-angle-only measurements is that in the lower atmosphere, water vapor content prevents temperature and humidity measurements to be made independently [90]. Intensity-based occultation measurements at short wave infrared (SWIR) wavelengths are made to improve those measurements. SWIR occultations are used for identifying and quantifying atmospheric constituents by observing absorption features across a spectrum of relevant wavelengths.

2.3.2.1 Laser Occultation Absorption Measurement Principles

For composition studies, measurements are made by sampling signals through the atmospheres at a range of infrared wavelengths that correspond to absorption features and continuum of atmospheric species of interest (carbon dioxide, methane, water vapor). The relative attenuation at each of these spectral bands gives information on how much of the corresponding compound is present in the atmosphere.

2.3.2.2 CubeSat Intersatellite Communications Missions

While there have not yet been nanosatellite missions specifically dedicated to atmospheric characterization through laser occultation, optical beacons have been flown on orbit and are an active area of research [91]. Beacons have primarily been used for space-to-ground communications, but intersatellite links have also been studied [92] [93]. Satellite crosslinks are useful in formation flying missions and enabling network communication, and this technology can be applied to laser occultation. The use of dual-stage pointing systems (coarse body pointing and fine control with a fast steering mirror) [58] enables smaller beam sizes, which would make a cross-link system more power efficient but would require improved pointing knowledge and stability.

2.3.2.3 Challenges of Lower Atmospheric Occultations

The main challenges in obtaining cross-linked optical occultation measurements on a nanosatellite platform are:

1. Accounting for scintillation, beamspread, and pointing offsets caused by atmospheric turbulence

2. Resilience to clouds in the crosslink path

3. For intersatellite links, maintaining pointing and orbit position to the precision required

4. For intersatellite links on a nanosatellite, supplying a transmitted signal bright enough to be received at the longest expected range

These effects are most prominent in the lower atmosphere where water vapor content is most substantial. One way to combat the challenges of sounding deep into the atmosphere is to use adaptive optics to measure turbulence-induced errors and minimize their impact on the measurements.

2.3.2.4 Adaptive Optics for Atmospheric Correction

Adaptive Optics (AO) is a method for real-time correction of wavefront distortions that may affect the performance of an optical system. For signals that pass through the atmosphere, such as a laser occultation crosslink, a typical cause of wavefront aberration is atmospheric turbulence, which encompasses changes in the atmosphere due to temperature, pressure, wind velocities, humidity, and temporal changes. In space, wavefront control systems are needed to correct for the effects of diffraction, manufacturing imperfections, the changes in an optical system after surviving launch and existing in a varying thermal environment (both local to the spacecraft and throughout the orbit and as a function of pointing), and the structural and mechanical effects of actuators and the spacecraft attitude control system, such as jitter.

The control surface in adaptive optics is a Deformable Mirror (DM). A DM is a reflective element split into 10s to 1000s of actuators that can move independently normal to the surface in order to change the shape of the mirror (and thus the shape of the wavefront reflecting off the mirror).

DMs can either be continuous (one flexible reflective coating overlaid across all actuators) or segmented (each actuator is a separate part of the mirror). Segmented actuators tend to have more degrees of freedom (piston, tip, and tilt) and can be used for spatial modulation, but they introduce diffraction patterns to an image. Figure 2-5 is a schematic of two different deformable mirror designs, one with a continuous facesheet and one with segmented apertures. Continuous facesheet mirrors can be actuated at rates of up to 6 –7 kHz. Segmented mirrors can be driven even more quickly (10 kHz).

There are several alternatives for DM actuations, though the high level operation is the same: variable voltage is applied across each actuator to bring it to the desired height. The most common actuators are piezoelectric and electrostatic (typically found in MEMS devices). Piezoelectric actuators have been in use longer and are more robust than electrostatic actuators, but those actuators exhibit hysteresis. Other methods of actuation include magnetic voice coils.

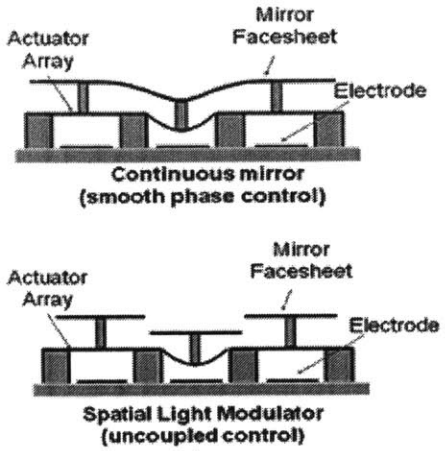

Figure 2-5: Electrostatic DM actuator architectures: (Top) continuous facesheet and (Bottom) segmented apertures.

Microelectromechanical Systems (MEMS) deformable mirrors [94], such as the devices manufactured by Boston Micromachines [95], are cheaper than piezoelectric devices, have smaller actuators (so more will fit across a given pupil), and do not exhibit hysteresis [96] [97]. The compact size of a MEMS DM of a given actuator count means the other optics in the system can also be smaller and lighter, which is crucial for space-based systems [41]. Another benefit of MEMS DMs versus conventional macro-scale DMs that use piezo or electro-restrictive actuators is that their capacitance is lower, so for comparable drive voltages they should consume less power. In practice, the amplifiers typically used in driver electronics have high slew rates that drive up the power requirements. For longer timescale applications, alternative drive electronics may be more efficient.

2.4 Exoplanet Direct Imaging

Earth atmospheric observation is not the only area in which remote sensing is relevant. Exoplanet detection and characterization is important for understanding the formation of our solar system and discovering if other habitable planets exist.

In order to image an Earth-like planet, an exoplanet direct imaging system needs to achieve a contrast ratio of 1×10^{-10}. A high-performance coronagraph is designed to

meet this requirement. Even with adaptive optics on a large ground-based telescope, it is currently not possible to overcome the effects from atmospheric turbulence to achieve the high contrast needed to obtain high resolution spectra of an Earth-like exoplanet [98] [99] [100]. While a space telescope does not have to overcome the effects of atmospheric turbulence, it is usually at the expense of smaller aperture size (e.g., due to launch cost and launch vehicle limitations) and the performance of a space telescope will still suffer from optical imperfections, thermal distortions, and diffraction that will corrupt the wavefront, create speckles, and ruin the contrast [101] [46]. Active optical control is still needed to achieve the desired contrast on a space telescope.

In order to observe the reflected light spectrum of an Earth-like exoplanet, the instrument used must first be able to resolve the planet from the star and, second, have some way of blocking the parent stars light to reduce starlight diffraction such that the reflected light from the orbiting exoplanet can be detected. The Rayleigh criterion of $\theta = 1.22\lambda$ describes the minimum angular separation between two monochromatic point sources that can be unambiguously resolved by a telescope with primary circular aperture of diameter D at wavelength λ.

An instrument called a coronagraph, originally developed to study the solar corona, uses an optical element to achieve the blocking of the parent stars light well enough that reflected light from an orbiting exoplanet can be detected. The coronagraph optical element can be as simple as an amplitude mask (e.g. [102], [103]), or it can be more complex and use both amplitude and phase to remove or relocate parent stars light ([104], [105], [106]). The coronagraph design must also consider the effect of the point spread function of each point source and the way that diffraction redistributes the light from the parent star across the image. High-performance coronagraphs are needed to achieve contrast ratios on the order of 1×10^{-10} in order to detect an Earth-like planet around a Sun-like star.

There are other proposed methods for obtaining spectra of Earth-like exoplanets. Some examples include combined-light spectra obtained from transit photometry observations (e.g. [107]), using an "external occulter"instead of an internal corona-

graph (e.g., [108]), or using interferometry (e.g., [109] [110]). The transit photometry method takes advantage of the fact that at some point during a transit observation, the exoplanet travels behind its parent star, although this is a rare occurrence and limits the sample population to planets that can be observed transiting their parent star. This is called a "secondary eclipse."When the planet is in secondary eclipse, the observation is only of the spectrum of the parent star. This can be compared with "combined-light"spectra that are obtained when both the planet and the parent star are in view. Challenges with the combined-light approach involve being able to discern the contribution of the reflected light from the planet from the much larger signal of the parent star, as well as understanding the variability of the parent star. The external occulter approach takes the occulting element from an internal coronagraph and places it at a large distance from the telescope. This approach requires precise manufacturing of the starshade used as the external occulting element as well as precise control of the starshade position. All of these methods are described in detail in [39].

In this thesis, we focus on technologies that apply to the internal coronagraph direct imaging method. Nanosatellites are not suitable platforms for coronagraphic imaging of exoplanets, but they do provide a useful technology development platform. High actuator count adaptive optics are critical to achieve exoplanet direct imaging with internal coronagraphs, and MEMS deformable mirrors are attractive for space applications because of their small size and power draw. A nanosatellite could be used to space-qualify MEMS deformable mirrors.

2.4.1 Achieving High Contrast with Adaptive Optics

A high-performance coronagraph is used to meet the high contrast imaging requirement for Earth-like exoplanet direct imaging. Even with adaptive optics on a large ground-based telescope, it is currently not possible to overcome the effects from atmospheric turbulence to achieve the high contrast needed to obtain high resolution spectra of an Earth-like exoplanet [98] [99]. While a space telescope does not have to overcome the effects of atmospheric turbulence, it is usually at the expense of

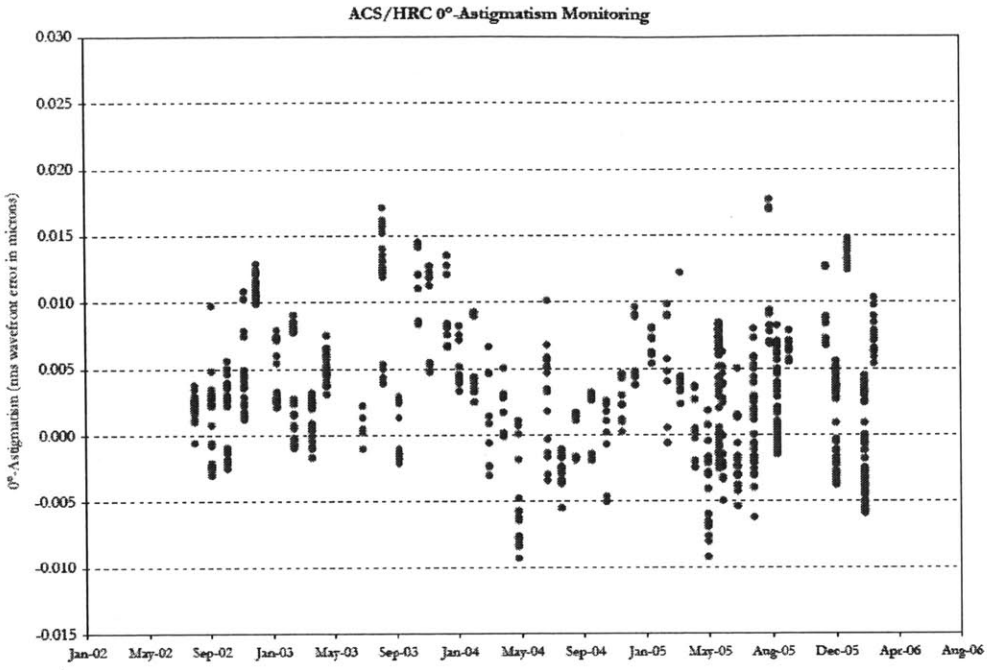

Figure 2-6: Long term 0-degree astigmatism aberrations observed on the Hubble Space Telescope [111]

smaller aperture size (e.g., due to launch cost and launch vehicle limitations) and the performance of a space telescope will still suffer from optical imperfections, thermal distortions (as illustrated in Figure 2-6), and diffraction that will corrupt the wavefront, create speckles, and ruin the contrast. Active optical control is still needed to achieve the desired contrast on a space telescope.

Optical aberrations can be decomposed into sets of orthogonal basis functions (Zernike, Fourier, etc). For Zernike modes (see Figure 2-7), low-order modes such as tip and tilt, defocus, and astigmatism have historically been managed with tight surface error requirements, vibrational and thermal isolation or with active optical elements such as the segments on James Webb Space Telescope. Higher-order modes require more sophisticated correction techniques. This is especially true of imaging through the atmosphere, where atmospheric turbulence has a significant impact, but it is also applicable for space imaging platforms very sensitive to wavefront error, such as high contrast imaging.

The need for high actuator count deformable mirrors for an exoplanet direct imag-

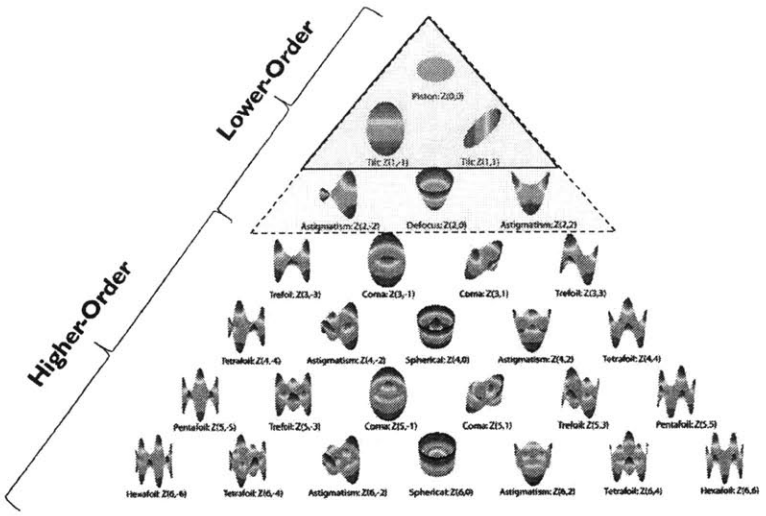

Figure 2-7: Zernike modes are a set of orthogonal basis functions used to describe the surface of a wavefront. We distinguish between lower and higher-order modes

ing mission is also driven by the angular separation from an on-axis star about which we can look for an exoplanet, as the deformable mirror must have the authority to compensate for speckles and aberrations over this region. The spatial frequency of periodic aberrations in the pupil plane determines where the speckles caused by these aberrations will land in the focal plane. The speckles represent the spatial Fourier transform squared of disturbances in the pupil plane, so the higher the spatial frequency of the aberration, the further off-axis the speckle will land in the focal plane. In a coronagraphic imaging system, once the on-axis star has been blocked, high contrast levels are still required on the detector in the off-axis regions where exoplanets may exist. High actuator count deformable mirrors have the authority to correct high spatial frequency aberrations that would otherwise degrade the contrast in these locations [39]. If a deformable mirror only has a few actuators, it can only correct for low spatial frequencies that are close to on-axis in the image plane, corresponding to larger-scale distortions in the pupil plane. To be able to correct for speckles and aberrations further out around a star so that we can look for exoplanets in the region known as the habitable zone, it is necessary to have mirrors with more actuators and the corresponding control over higher spatial frequencies (further off-axis in the image

plane).

High actuator count MEMS deformable mirrors that would enable high contrast imaging from a space platform have not yet been characterized in space over a long-term operation. MEMS deformable mirrors have been demonstrated on the ground and have flown on short-duration missions in space-like environments. A nanosatellite with an optical payload capable of characterizing the mirrors would offer a platform for on-orbit technology validation.

2.4.1.1 Space Qualification

To be considered space-qualified, a component must survive both the launch environment and long-term on-orbit operations. There are varying degrees to which NASA considers a technology space-qualified [112], and for typical missions, all component technology should be at or above Technology Readiness Level (TRL) 6 by the Preliminary Design Review. There are several testing methods and approaches to increasing space technology readiness [113]. High-actuator count MEMS deformable mirrors are currently below TRL 6 for high contrast imaging applications [41].

Potential failure mechanisms for MEMS devices have been studied and presented in detail in [114], [115], [116], [117]. For launch and on orbit operations of high actuator count MEMS deformable mirrors, the main concerns are:

- Mechanically-induced failures from launch loads
  - Detachment or plastic deformation of die attachments
  - Wire bond detachment from bond pads
  - Electrical shorting between adjacent wires
  - Plastic deformation or fracture of thin film elements
- Electrically-induced failures from on-orbit environment (radiation, plasma)
  - Actuator stiction
  - Actuator unresponsiveness

  - Actuator drift
  - Variations in actuator gain

- Mechanically-induced failures from on-orbit environment (thermal, jitter, vacuum)
  - Break of hermetic seal; actuator ringing
  - Thermally-induced surface distortions
  - Jitter-induced surface distortions

Some of these failure modes can (and should) be addressed through ground tests and modeling, particularly launch-induced failures. The loads and environment for launch vehicles is very well understood, and testing profiles (vibration, acoustic, and shock) are available from launch providers [118]. Any atypical launch configurations (e.g. helium purging) are also known ahead of time and can be successfully mimicked in ground testing. Ground testing is useful to observe mirror response to high radiation environments, and tests performed on similar devices (digital micromirror devices [119]) showed that faults due to proton and heavy ion radiation do occur but are recoverable. Thermal vacuum testing is also useful, and MEMS deformable mirrors have been successfully tested in vacuum environments at NASA Ames [55].

High-altitude platforms such as balloons, sounding rockets, suborbital flights, and microgravity flights [120] are useful platforms to test devices in near-space environments. Two sounding rocket experiments have flown MEMS deformable mirrors and a high altitude balloon [48] [49] [121]. These tests verified short-term performance of MEMS devices in a low-altitude space environment. The positive results are encouraging for future space qualification, but they are not sufficient to argue the success of long-duration operation in a higher orbit. Test spaces on the International Space Station also offer fairly low-cost methods to further space-qualify components in a controlled (and comparatively benign) environment [122]. A recent ISS test of MEMS micromirrors (different from the deformable mirrors identified in this thesis) showed

very promising performance during depressurization, heating, electrostatic charging, shock, and vibration tests. [51].

Ground and sub-orbital testing are useful to identify and substantially mitigate known failure modes in space qualifying components. However, on-orbit qualification of critical components (such as MEMS deformable mirrors for high contrast imaging) is useful for establishing heritage and understanding how the device is expected to perform in its design environment. Ground-based facilities have been used to simulate elements of the space environment for over 40 years, but thermal vacuum chambers offer only approximate on-orbit conditions, and solar and radiation simulators do not provide the vacuum intensity or full energy spectrum of particles present on orbit [123]. There is also the question of failure modes that occur due to interactions of several facets of the space environment that cannot be predicted or created on the ground.

One of the main challenges associated with on-orbit testing is the cost and complexity typically associated with space missions. Space-based platforms such as nanosatellites have the potential to bridge that gap and provide critical information about a components behavior in the space environment on a free-flying platform within an achievable cost and timeline. This does involve careful consideration and design of the platform itself and the kinds of experiments and data that will provide sufficient information to characterize the component.

2.5 Summary of Gap and Contributions

This thesis contributes to the improvement of atmospheric sensing on nanosatellite platforms that enable a new regime of science and technology missions. The contributions in this thesis and the corresponding advances in the state of the art are described in Table 2-2.

We address several gaps in the three areas of literature. Nanosatellite constellations with earth-facing sensors have been researched extensively, but there has been less work done in measurement coordination or coordinated measurements using in-

tersatellite links. Chapter 3 presents an analysis of GPSRO instruments in terms of both global coverage and obtaining measurements that overlap spatially and temporally with measurements from a microwave radiometer. Chapter 4 presents global coverage and observation opportunities for intersatellite links in Low Earth Orbit.

In the two scientific payload regimes, we model key characteristics of atmospheric retrieval on nanosatellite platforms. Microwave radiometers and GPSRO instruments have been successfully designed and flown on nanosatellites, but we show how a nanosatellite GPSRO instrument sounding through the neutral atmosphere can provide a measurement capability that has not yet been demonstrated, and neutral atmospheric GPSRO measurements can be used to achieve better than state of the art radiometry calibration.

Laser occultation missions have not yet been flown in space, and one of the challenges associated with sounding deep into the atmosphere is turbulence. We perform a preliminary characterization of crosslink atmospheric turbulence and develop a CubeSat adaptive optics payload to demonstrate critical technology (MEMS deformable mirrors) to address this challenge. MEMS deformable mirrors are useful for atmospheric compensation, thermomechanical or jitter error correction, and speckle nulling (coronagraph missions). A nanosatellite technology demonstration of this technology will enable its use in a variety of applications to improve imaging and sounding capabilities on future space platforms.

Table 2-2: Thesis Contributions

Topic	Current State of the Art	Thesis-Enabled State of the Art	Rationale
Passive Microwave Radiometry Calibration	0.75 K, 1–1.5 K on nanosatellite platforms	0.25 K on nanosatellites (pending launch validation)	Based on my predicted precision of collocated CubeSat GPS radio occultation measurements
Atmospheric Occultation —Radio	Neutral atmosphere GPSRO not demonstrated on CubeSats	0.1–1.7 K precision in neutral atmosphere from CubeSat GPSRO platform (pending launch validation)	Simulated results from COTS receiver with custom antenna
Atmospheric Occultation —Optical	Intersatellite occultation in lower troposphere (<5 km) dominated by scintillation and distortion	Sounding in lower troposphere improved with adaptive optics (mid-actuator count deformable mirrors can compensate for turbulence lower than 5 km)	Crosslink atmospheric turbulence modeling compared with control authority of MEMS deformable mirrors
MEMS Deformable Mirror Technology Readiness Level	Tests performed to date: vacuum, vibration, sounding rocket operation (NASA TRL 5-6)	Long-term on-orbit demonstration (NASA TRL 7 after successful flight)	Design and laboratory validation of mirror characterization payload

Chapter 3

Nanosatellite Atmospheric Sounding and Sensor Calibration

In this chapter we go into more detail on improving microwave radiometry on a CubeSat platform by implementing a novel calibration method using co-located Radio Occultation measurements. We motivate this work with the MIT Lincoln Laboratory-developed suite of microwave radiometer CubeSat missions, focusing on MiRaTA (Microwave Radiometer Technology Acceleration) mission. We present the expected measurement performance of a GPSRO instrument on the MiRaTA spacecraft and assess the global coverage and calibration opportunities for low-earth orbit constellations of GPS radio occultation sensors.

3.1 Nanosatellite Microwave Radiometry

There have been several microwave radiometer technology developments and demonstration missions [74] [77] [76] [75] in recent years. Here we describe the challenges of implementing and calibrating passive microwave radiometers specifically on a CubeSat platform and provide background information on relevant development efforts through the MIT Lincoln Laboratory.

3.1.1 CubeSat Microwave Radiometer Design and Calibration

The performance metrics used to determine the overall utility of a microwave radiometer are the resolution (horizontal and vertical), number of bands, sensitvity, and measurement revisit rate. Beamwidth and sample rate determine the ground resolution of the measurements, the number of channels influences the vertical resolution of the measurements, and different bands yield different science measurements [124]. For a standard 3U CubeSat platform, the aperture is limited to about 9 cm, and acceptable orbits range from 400 - 700 km in altitude. This drives a 2 —6 degree half power beamwidth depending on the sampling wavelength, and typical ground sample distances are 25 —50 km. There has been extensive research on developing constellations of radiometers (and other Earth-observing sensors) [70] [69]. By scanning the radiometer and implementing constellation missions, global coverage is possible down to 15-30 minute revisit times.

It is important to calibrate passive radiometers, ideally with a National Institutes of Standards and Technology (NIST)-traceable source. One of the main challenges in shrinking passive radiometer systems onto a CubeSat-sized platform is maintaining consistent calibration of temperature measurements. The internal calibration targets on instruments such as AMSU and ATMS are very stable, but they cannot be easily implemented on a CubeSat-sized platform due to volume constraints and challenges related to thermal gradients and stray radiation containment. Figure 3-1 shows the scale of calibration targets used for ground based calibration or flown on large satellites.

A common approach for CubeSat radiometer calibration is to use a noise diode to inject known noise in the receiver module [126]. Internal matched loads can also be used at select frequencies. Figure 3-2 shows how these types of calibration methods are implemented on the MiRaTA radiometer. The Micro-sized Microwave Atmospheric Satellite (MicroMAS), a precursor to the MiRaTA mission also developed by MIT Lincoln Laboratory and the MIT Space Systems Laboratory, featured a scanner

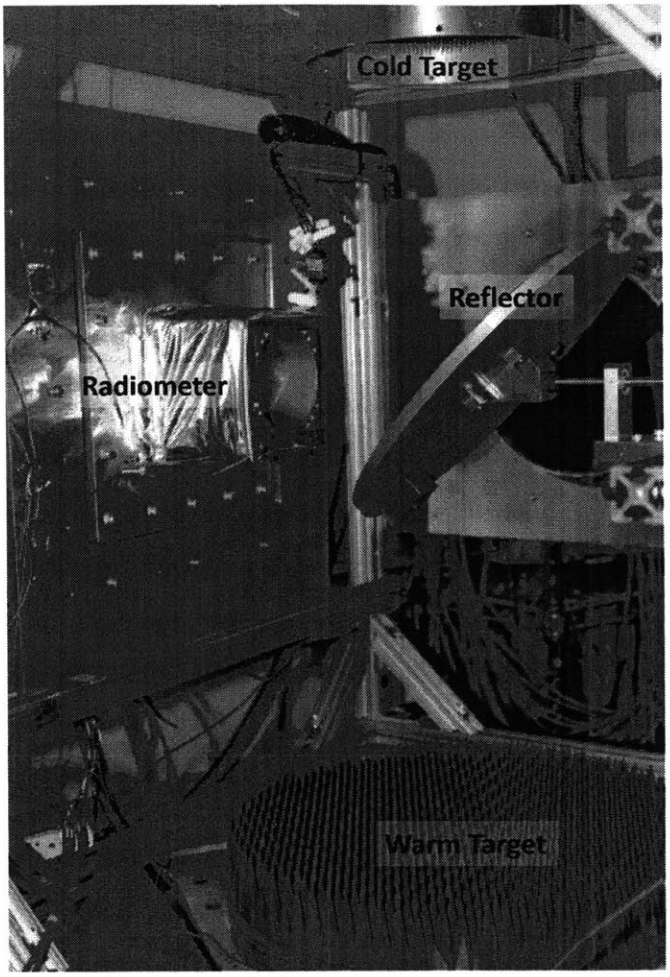

Figure 3-1: Radiometer calibration setup with warm and cold targets [125]

assembly to spin the payload at 40 rpm in order to allow the radiometer to scan across the Earth and cold space. The 3 K of deep space and an internal noise diode served as the cold and warm calibration points, respectively. The satellite experienced a loss of communication shortly after power-on, and on-orbit calibration information was not collected. MicroMAS-2, scheduled for launch in early 2017, is a re-flight of the MicroMAS mission and will host a four-band radiometer [21] The Radiometer Atmospheric CubeSat Experiment (RACE), developed by JPL, incorporated a noise diode coupled to an LNA as well as used periodic views of deep space for its internal calibration [75], but RACE experienced a launch failure in 2014. IceCube [77] and PolarCube [74] also inject noise using an internal diode.

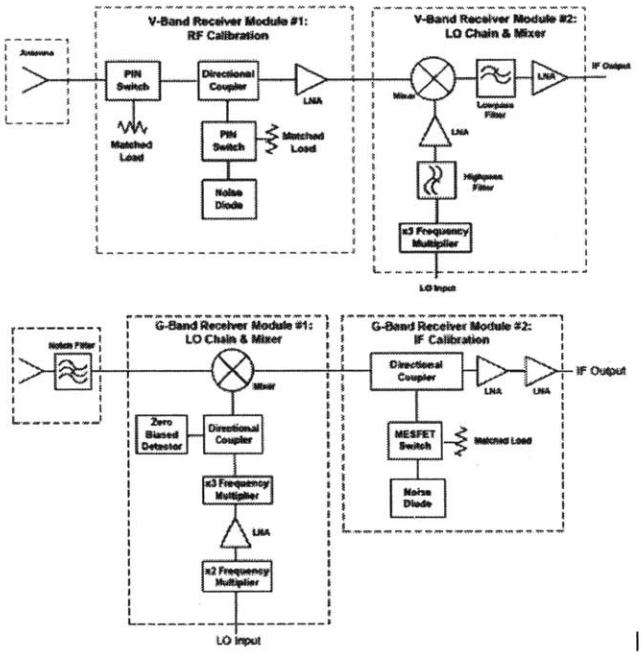

Figure 3-2: Diagram of MiRaTA radiometer internal electronics. Top: The V-band receiver modules include an internal matched load as well as a noise diode. Bottom: The G-band receiver modules include a noise diode.

Switches for internally matched loads can be lossy (or unavailable), and the long-term stability of noise diodes can vary widely between components. Noise diode drift can range from 0.5% to 3%, which is not currently as low as the larger heritage calibration targets [126]. Additional calibration methods are needed on these systems to enable absolute calibration accuracy better than 1 K over mission lifetimes [79]. It is possible to characterize noise diode drift on the ground, and research has shown that for some diodes, drift is predictable and stabilizes after about 6 months [127]. One goal of MiRaTA is to provide a way to calibrate the noise diode using GPSRO profiles.

3.1.2 MiRaTA Radiometer and Mission Overview

The Microwave Radiometer Technology Acceleration (MiRaTA) mission is another MicroMAS follow-on mission, but unlike MicroMAS-2, TROPICS, and EON, the payload does not spin independently of the bus. The primary science payload on

MiRaTA is a tri-band microwave radiometer, and it also flies a GPS radio occultation instrument, Compact TEC (Total Electron Content) and Atmospheric GPS Sensor (CTAGS). The GPSRO instrument generates both science data and position, navigation, and tracking information [78].

The primary science payload on MiRaTA is a tri-band microwave radiometer. For MiRaTA, the mission requirements stipulate that the radiometer measurement accuracy shall be no worse than 1.5 K and 2.0 K at V band and G band, respectively, which is roughly double (e.g. worse) the requirements for the state of the art ATMS instrument [128]. The plan for MiRaTA is to calibrate its radiometer using cold space and a noise diode. The noise diode drift will be characterized based on radiometer measurements and GPSRO measurements sampled from overlapping volumes of atmosphere with the goal of significantly improving our requirements.

MiRaTA will be launched into a sun-synchronous elliptical (440 $\times$ 811 km) orbit through NASAs Educational Launch of Nanosatellites 14 (ELaNa) initiative. Because of the configuration of the sensors on the spacecraft as well as navigational and power subsystem requirements, MiRaTA will use two operational modes [125]. In the first, or 'nominal'mode, the radiometer is pointed nadir and the CTAGS antenna is directed zenith. This configuration allows the satellite to maintain a low drag profile and adjust the orientation of the solar panels with respect to the sun for optimal power draw. CTAGS provides position information as it includes a GPS receiver. A second operational mode, 'pitch-up'mode, is required to enable the CTAGS calibration measurements. Figure 3-3 illustrates the spacecraft orientation and sensor pointing in both of these modes.

The satellite performs a periodic 'pitch up'science maneuver, shown in Figure 3-4. For each science maneuver, the satellite starts in a local vertical local horizontal (LVLH) stabilized orientation with the radiometer pointed towards Earth and the GPS antenna toward deep space. The radiometer is powered on and the satellite pitches up to allow the radiometer to scan the Earth's limb and holds its attitude between 113 and 118 degrees from local horizontal (with the CTAGS antenna boresight at or slightly below the limb).

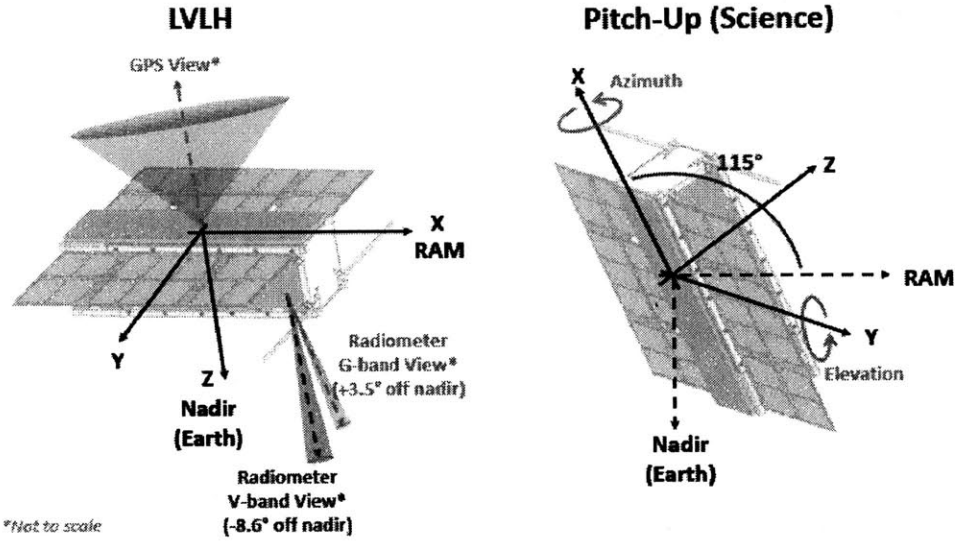

Figure 3-3: MiRaTA Axes and Orientation Nomenclature. Left: Local Vertical Local Horizontal (LVLH) orientation. Right: Pitched-up orientation to achieve GPS Radio Occultation with assumed 115 degree pitch-up angle

To estimate the performance and spacecraft resource utilization, we developed a simulation of the transition from normal mode to pitch-up mode. The simulation assumes MiRaTA reaches a final pitch-up angle of 115 degrees regardless of its altitude (tailoring the simulation for the actual pitch-up profile given the elliptical orbit and constraints of the onboard attitude control system is an item for future work). This allows the CTAGS antenna to point towards the limb of the Earth, and as the satellite flies it collects occulting GPS signals from nearly the same volume of atmosphere as that scanned by the radiometer. The GPSRO and radiometer measurements need to overlap at a minimum tangential height of 18-22 km within 100 km (horizontal) of the radiometer boresight. The desired overall precision of the CTAGS temperature measurements is less than 1.5 K (goal of 0.5 K).

3.1.3 MiRaTA Radiometer

The MiRaTA tri-band radiometer samples at V-band (50-57 GHz) and G-band (175-191, 205 GHz). The half-power beamwidth (HPBW) of the radiometer at V-band is 5.6 degrees and G-band is 1.7 degrees. The G-band beam is about 3.5 degrees off-

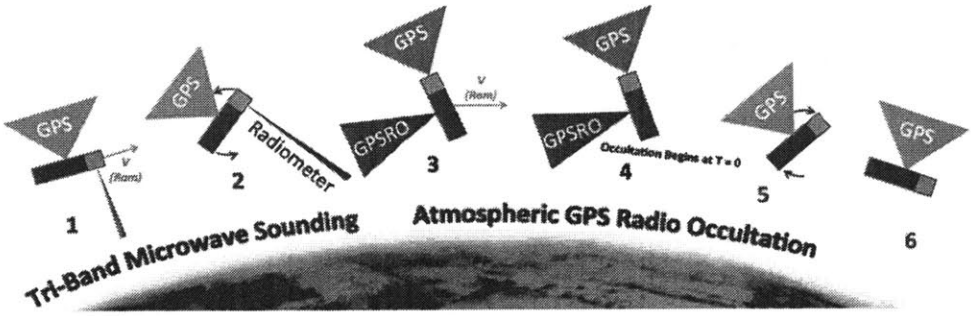

Figure 3-4: The MiRaTA CubeSat primary mission validation Concept of Operations pitch-up maneuver

axis from spacecraft z-axis, and the V-band beam boresight is offset by 8.6 degrees in the other direction (see Figure 3-3). The V-band nadir footprint ranges from 45 km to 84 km through the orbit. The radiometer is expected to achieve absolute radiometric accuracy of 1.5 K at V-band and 2.0 K at G-band [125]. Radiometric precision at V-band is expected to be better than 0.1 K NEdT (noise equivalent delta temperature), and at G-band better than 0.3 K NEdT. The GPSRO measurements are primarily used for V-band calibration. In simulations investigating the utility of hosting both the radiometer and GPSRO on the bus, Blackwell et al. showed that absolute calibration accuracy down to 0.25 K is achievable for temperature sounding channels in this band for a total-power radiometer using a weakly coupled noise diode for frequent calibration and proximal GPSRO measurements (assuming 0.3-0.4 K temperature error) for infrequent (approximately daily) calibration [79].

3.1.4 MiRaTA GPSRO Sensor

The Compact TEC (Total Electron Content) and Atmospheric GPS Sensor (CTAGS) consists of a COTS GPS dual frequency (L1 at 1575.42 MHz and L2 at 1227.60 MHz) receiver (NovAtel OEM628) [88] with custom firmware modifications, a custom 3-element dual-frequency patch antenna array, and LNA/RF front-end. The CTAGS antenna is mounted on the MiRaTA spacecraft on the opposite face as the radiometer field of view (in nominal mode, the radiometer faces nadir and the CTAGS antenna

faces zenith providing navigation data). The MiRaTA CTAGS payload is designed to accept customizable commands. Specifically, it allows differing sampling rates depending on the elevation and azimuth of the GPS constellation satellite location relative to MiRaTA. In the nominal operating mode CTAGS samples at 0.1 Hz for non-occulting satellites and 1 Hz for occulting. In the occultation mode, CTAGS samples at 50 Hz for occulting satellites and for a single above horizon reference satellite. The use of a dual frequency receiver supports straightforward removal of clock errors and the effects of the ionosphere from troposphere and mesosphere observations.

Measurements made by the radiometer will be compared to radio occultation measurements of the nearly same volume of atmosphere. For this mission, CTAGS provides exclusively 'setting'or 'ingress'occultations providing a solid lock on signals as they pass through the mesosphere and troposphere. 'Rising'or 'egress'occulting signals may not be locked on until they are well above the troposphere/mesosphere.

3.1.5 MiRaTA Radiometer Calibration Process

Blackwell et al [79] related GPS-derived refractivity error (nominally 0.002 fractional error for altitudes between 10-20 km) to radiometer brightness temperature calibration error, using 0.002 fractional refractivity error to produce an absolute radiometer calibration accuracy of 0.25 K. The calibration method presented in [79] takes place in two parts. First, a quadratic relationship between the GPSRO refractivity profile versus tangent height, N(h), and radiometer brightness temperatures at a particular observing angle and frequency band of interest, TB(, f), is derived. Second, the radiometer gain, g, (in Kelvin/count, where count is the output of a 16-bit A/D converter) is chosen to minimize the residual between the calibrated and GPSRO-derived brightness temperature. Errors due to the quadratic estimation are treated in a weighted least squares sense.

Figure 3-5 shows the science data validation process for the MiRaTA mission with the contributions from this paper (CTAGS data products) called out in the light blue box. The refractivity from the GPSRO measurements are used to calibrate the radiometer as described in [79]. Truth data (middle line) are obtained from Numerical

Weather Prediction (NWP) model outputs (e.g., ECMWF) and radiosonde measurements and are used to validate the radiometer data. The intrinsic GPSRO retrieval performance is also assessed through comparison against the NWP and radiosonde data to evaluate the fundamental utility (accuracy and precision) of the GPSRO temperature retrievals.

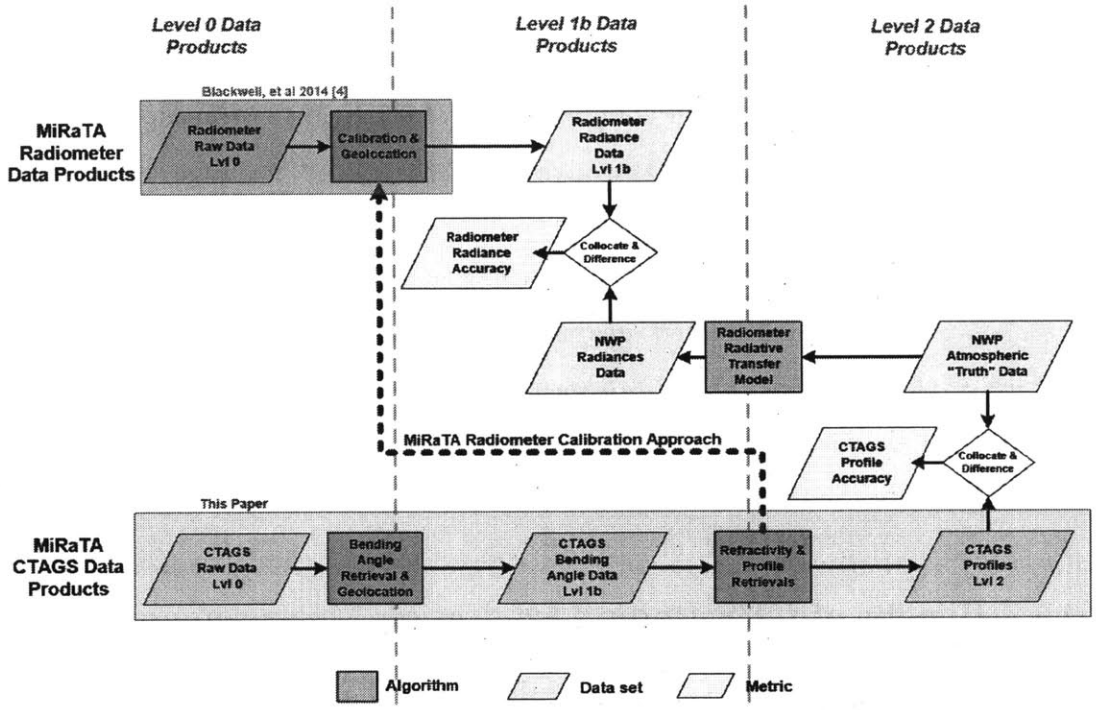

Figure 3-5: Ground processing and validation flow for the MiRaTA mission data products (blue highlight box indicates contributions from this thesis)

We characterize the precision associated with the GPSRO retrieved profiles. While the radiometer calibration process uses GPSRO-derived refractivity profiles in its calculations, [27] relates GPS refractivity error to temperature profile retrieval error, showing that a fractional refractivity error of 0.002 (value assumed in the radiometer calibration calculations in [79] corresponds to a temperature error of approximately 0.5 K for altitudes between 10-20 km. We therefore use 0.5 K GPSRO temperature error as the threshold requirement to achieve the 0.25 K brightness temperature error reported in Blackwell, *et al.* We present an analysis of the MiRaTA GPSRO retrieved temperature and compare with the 0.5 K requirement.

3.2 Nanosatellite GPS Radio Occultation

GPS radio occultation, as introduced in Chapter 2, uses information on atmospheric and ionospheric delay in received GPS signals to measure the local pressure and temperature of the atmosphere. Neutral atmospheric sounding has not yet been successfully proven on a CubeSat, though there are several missions that have flown or plan to fly instruments for this purpose. The current state of the art for GPS radio occultation temperature precision is on the order of 0.1 K in the troposphere, and for the MiRaTA mission, the requirement is better than 1.5 K precision in order to calibrate the radiometer to the required levels as explained in Section 3.2.

Challenges of implementing GPSRO on a CubeSat include limited data processing and storage capability, and limited area and volume for a high gain dual frequency GPS receive antenna. The limited processing and data storage capability means it is generally easier to accommodate a closed-loop GPSRO receiver than an open-loop receiver. COTS receivers are restricted to phase-locked loop, closed-loop tracking.

3.2.1 Benefit of GPS Radio Occultation Measurements

Radio occultation measurements are frequently used as calibration sources for sondes and passive radiometers [17], because they provide highly accurate (0.1 K or better) and precise (0.05 K or better) measurements with relatively uniform spatial/temporal coverage. There is also very little satellite-to-satellite bias (less than 0.05 K) [82].

3.2.2 Achieving Global Occultation Measurements with CubeSats

It is widely acknowledged that GPSRO instruments are capable of providing global measurement coverage. We look at different orbit parameters and constellations of GPS radio occultation satellites to assess whether this is true for instruments that also require position, navigation, and tracking information. The 2007 National Academy of Sciences decadal study calls for 2500+ occultations per day at 200 m resolution in

the lower atmosphere [3]. The following subsections describe a model for determining the number of valid anticipated measurements, the SNR for those measurements, and the revisit coverage for low Earth orbits between 400 and 700 km altitude and inclinations ranging from equatorial to sun synchronous.

3.2.2.1 Orbits and GPSRO Model for Global Measurements

The orbit and instrument parameters assumed for our study are summarized as follows:

- Orbit Altitudes: 400, 500, 600, 700 km
- Orbit Inclinations: 0, 30, 60, 98 degrees
- Antenna gain pattern: Gaussian
- 1 degree binning for latitude and longitude
- Satellites per orbital plane: 1, 3, 6

In the GPSRO model (Figure 3-6) we used Analytical Graphics, Inc's Systems Toolkit software to generate access profiles for sixteen combinations of altitude and inclination (400–700 km, 0–90 degrees) that include the numbers of occultations, the position of the occultations in relation to the antenna boresight, and the range of GPSRO accesses. This information was then fed into a model for revisit times and received SNR based on the antenna gain pattern.

A link budget analysis gives the primary metric – the SNR of the signal as is seen at the receiving spacecraft. The system-level inputs to the model—antenna max gain, the gain pattern (Gaussian or other), and antenna field of view—are also taken into account. There is generally a trade between antenna gain and antenna field of view, and both are important for GPSRO. Higher gain allows for signal penetration deeper into the atmosphere, while a larger field of view enables multiple satellites to be viewed at once (this is required in order to maintain positioning knowledge and to have non-occulted signals for comparison).

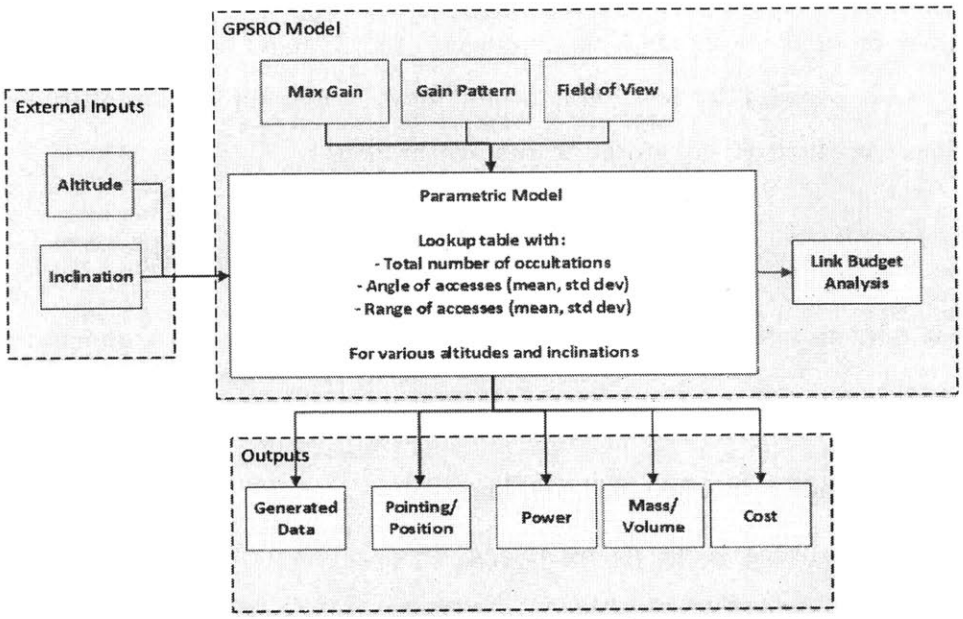

Figure 3-6: Model architecture for a GPSRO payload

3.2.2.2 Global GPSRO Coverage Results

For a setting occultation through the neutral atmosphere to be considered valid, there must be more than 4 GPS satellites in the GPSRO instrument antenna field of view. As seen in Figure 3-7, we see that high-altitude orbits are better for maintaining required access to GPS satellites during occultations and that mid-range inclinations tend to yield lower performance.

	400 km	500 km	600 km	700 km
0°	80%	84%	87%	89%
30°	60%	63%	66%	69%
60°	62%	65%	68%	71%
98°	69%	72%	75%	77%

%Time (out of 3 months) with 4 GPS satellites in view

	400 km	500 km	600 km	700 km
0°	36820	36570	36180	35530
30°	31150	31830	32330	32510
60°	33480	34490	35190	35600
98°	38780	39560	39990	40240

Number of GPS RO occultation opportunities below 200 km tangent height

Figure 3-7: Summary of occultation opportunities for a range of possible orbits over 3 months

The SNR of GPS signals should be more than 300 V/V in order to yield satisfactory retrievals of atmospheric thermodynamic properties below 20 km. With a 60 degree field of view for each satellite, the expected signal to noise ratios as seen at the receiver are shown in Figure 3-8 for the L1 frequency. This does not take into account atmospheric loss, so the antenna gain must be higher than 9.5 dB for useful science. Higher gain antennas can improve the overall SNR, but typically at the expense of the overall antenna field of view.

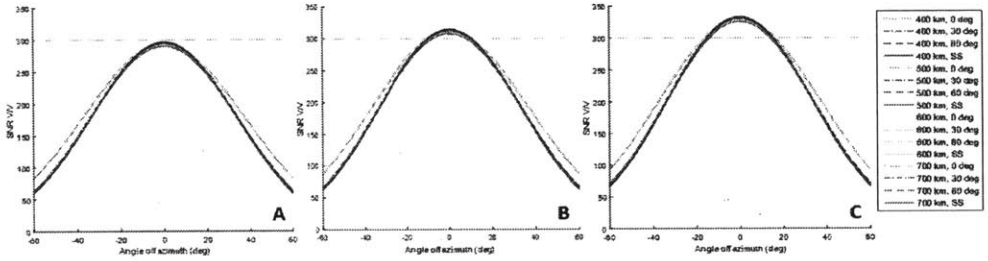

Figure 3-8: GPSRO Signal to noise ratio for (A) antenna gain of 9 dB, (B) antenna gain of 9.5 dB, and (c) antenna gain of 10 dB for varying orbit parameters (assuming a Gaussian antenna profile)

Figure 3-9 shows the impact of having more than one satellite per orbit plane on the coverage of occultations and the frequency of revisit measurements. The results shown are for a 600 km, 30 degree orbit. The more satellites in the orbital plane, the lower the median revisit time, with six satellites reaching median revisit times on the order of hours.

3.3 Radiometer Calibration with Radio Occultation - Overlapping Measurements

The MiRaTA radiometer calibration depends on obtaining coincident GPS and radiometer measurements. Understanding and predicting the occurrence of coincident occultations is critical to mission operations related to scheduling the calibration maneuver. The atmosphere observed by the radiometer and CTAGS should overlap as much as possible in order to accomplish the calibration objectives of the MiRaTA

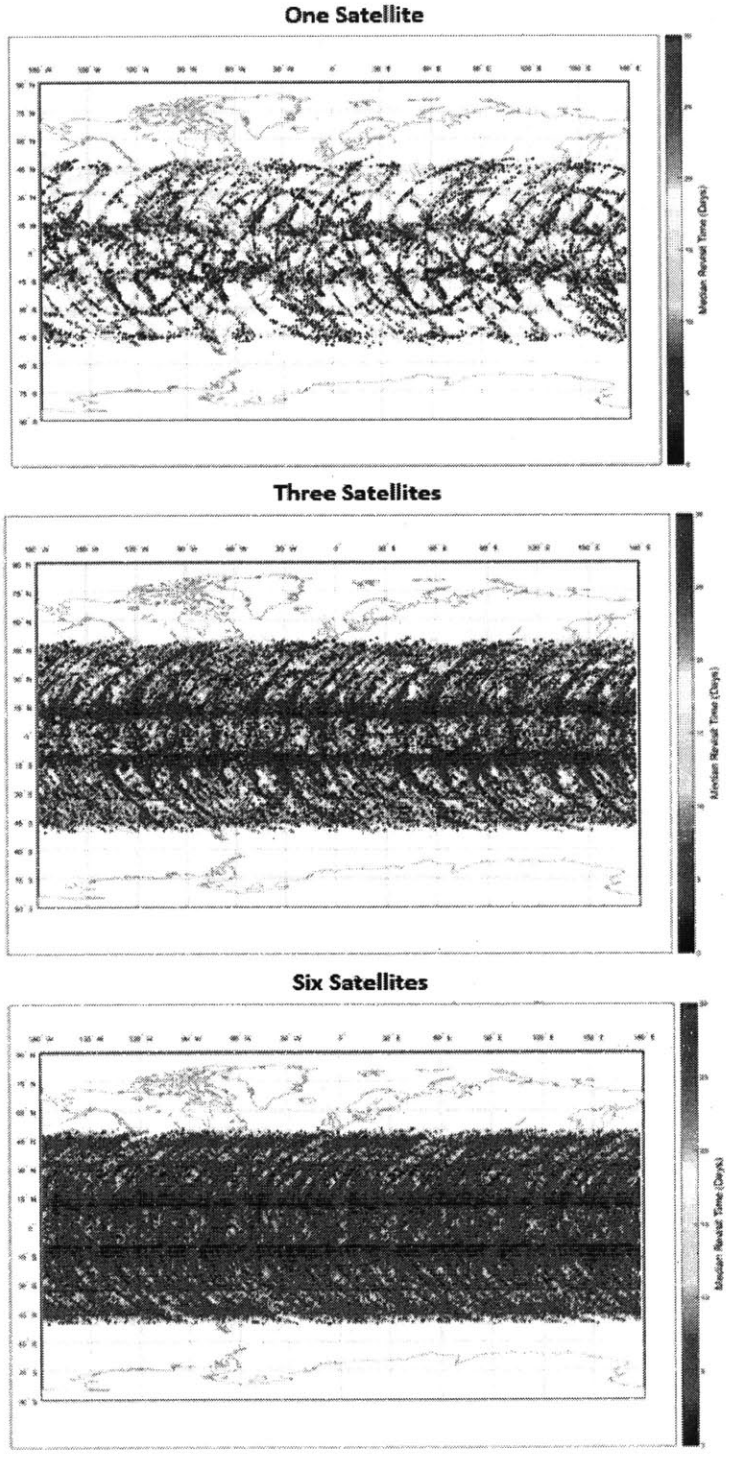

Figure 3-9: Revisit Times for (top) One (middle) Three and (bottom) Six GPS RO satellites. Color bars are consistent across all three plots.

mission [79]. The design orbit is elliptical, so the timing of each science maneuver will have to take into account the radiometer sampling location (making sure it scans the limb at the correct latitude and longitude) and the amount of time it will take the satellite to propagate to the location where it can capture the occultation. It takes less than a minute for the GPS satellite to set once line of sight to the GPS satellite from the perspective of MiRaTA has reached a tangential height of 25 km.

In order to calibrate the radiometer by comparing observations of temperature from both GPS radio occultation and radiometer measurements, measurements from the CTAGS and radiometer instrument must overlap spatially and temporally. This minimizes errors due to mismatched conditions during each measurement [129]. Based on the MiRaTA orbit geometry, measurements from CTAGS and the radiometer will overlap within a 10-15 minute window, and we specify that CTAGS measurements valid for calibration must fall within 100 km of the radiometer field of view. Over these temporal and spatial scales we can assume the upper tropospheric/lower stratospheric temperature is invariant [130]. In this simulation, which is focused on sounding overlapping atmospheric volumes and developing an approach for estimating GPSRO temperature profile accuracy, we are not concerned with radiometer signal to noise ratio, just the geometric field of view, 'FOV'. When the radiometer is pointed to the limb, depending on the spacecraft location in the elliptical orbit, the 100 km overlap range corresponds to an angle of about 2 degrees as seen by the spacecraft. Thus the radiometer receive field of view in the simulation (limb-facing) is defined as 2 degrees based on the 100 km overlap requirement, rather than the full V-band 5.6 degree HPBW. The radiometer 'FOV'boresight is offset from the anti-ram direction by 8.6 degrees so in order to compare CTAGS and radiometer temperature measurements, an occultation needs to occur when a GPS satellite passes through an azimuth window between 187.6 189.6 degrees with respect to MiRaTA (refer to Figure 3-3 for orientation convention).

The desired tangential height range for the overlapping radiometer and CTAGS calibration measurements is 18 km to 22 km. This tangential height was chosen based on the weighting functions for each of the MiRaTA radiometers 12 channels.

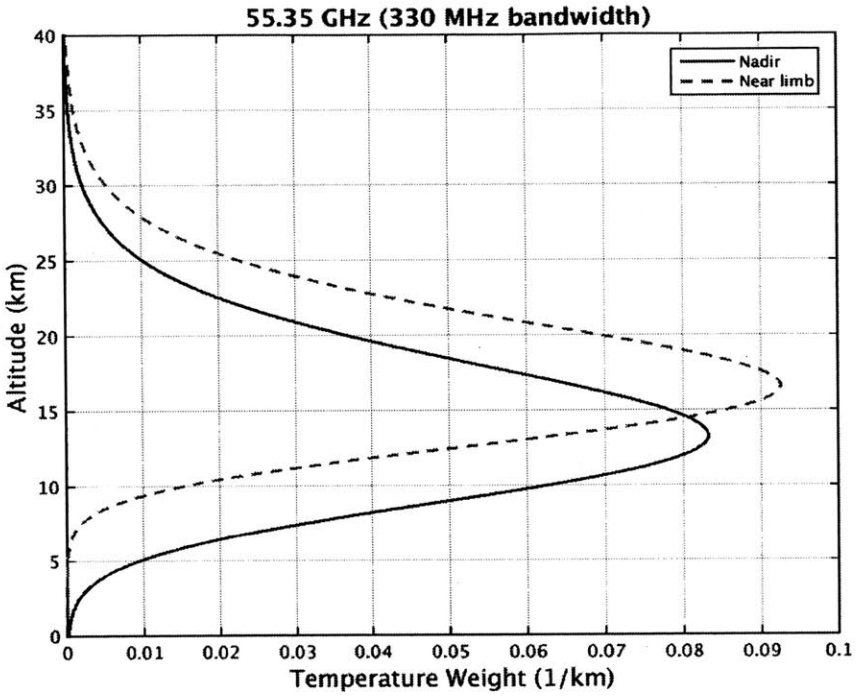

Figure 3-10: When limb-facing, the radiometer weighting function is about 3.5 km higher than when the radiometer is nadir-facing

The weighting function is for a nadir-facing beam. When the radiometer faces the limb, the weighting function peak height will be a few kilometers higher as shown in Figure 3-10. Ideally we would like to sample at lower altitudes, but this will depend on the ability of the CTAGS instrument to maintain lock on signals through the lower atmosphere.

3.3.1 Calibration Opportunities for the MiRaTA Mission

Here we assess the frequency, duration, and latitude and longitude locations of overlapping radiometer and GPS radio occultation measurements for the MiRaTA mission. In section 3.3.3 we expand this study to look at measurement overlap opportunities for other low Earth satellite orbits.

3.3.1.1 MiRaTA Calibration Overlap Model

An occultation needs to occur when a GPS satellite passes through an azimuth window between 187.6 189.6 degrees with respect to MiRaTA. This corresponds to a region within 100 km of the V-band radiometer boresight, where we assume the limb temperature is roughly invariant for a wide area of latitudes and longitudes [130].

This modeling effort does not take into account atmospheric bending, and the simulation currently considers two dimensions of overlap, one dimension in azimuth with respect to the MiRaTA spacecraft, and one dimension with respect to tangent height line-of-sight to the GPS satellite). For the CTAGS measurements, this volume can be estimated using the geometry of the first Fresnel zone, which depends on the tangential height and the relative positions of the GPS satellite transmitter and MiRaTA receiver, and in the atmosphere on the ratio of SNRv to SNRv0 (1-second signal to noise ratio in free space) [131]. We also plan to include a more detailed rendering of the radiometer sampling pattern and the sensitivity of the system to pointing and timing offsets in future model updates.

The orbit and model parameters assumed in this study are as follows:

- MiRaTA orbit (440 $\times$ 811 km, 13:25:30 LTAN)
- January 1, 2017 - April 1, 2017
- 10-second timestep
- V-band 8.5 degrees off nadir, 5.6 degree beamwidth

3.3.1.2 MiRaTA Calibration Overlap Results

Figure 3-11 illustrates the expected latitude and longitude distributions of all possible GPS occultation opportunities with tangential heights under 25 km over a period of 24 hours. The tangential heights are captured in the color bar (0 to 25 km scale). MiRaTA will see a daily average of 6 setting occultations that occur within the FOV of both the CTAGS antenna and the radiometer.

Over three months, there are 520 occultations that fall within the azimuth and elevation viewing requirements and reach a tangential height of less than 25 km. The

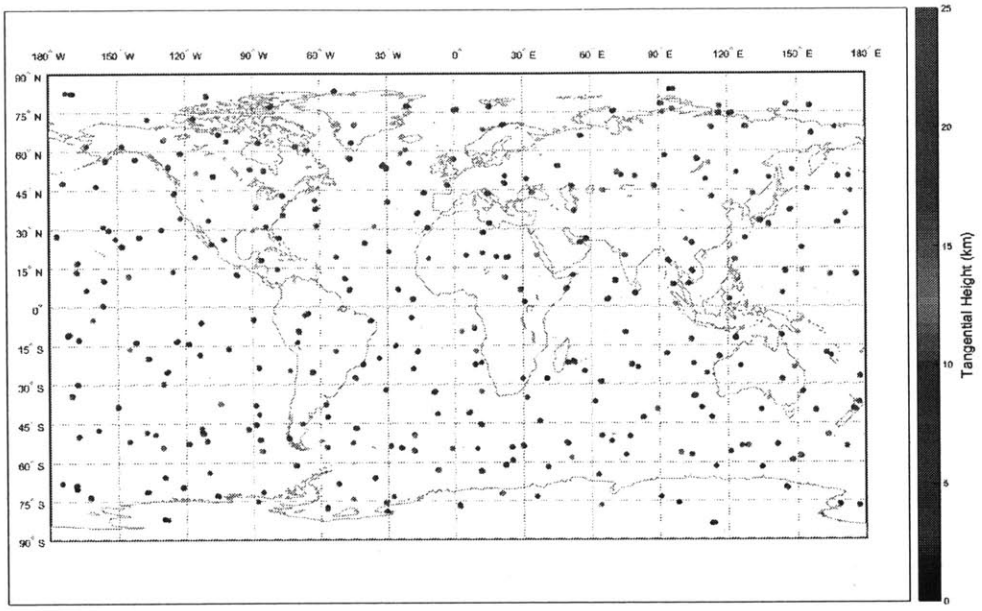

Figure 3-11: Tangential height (< 25 km) as a function of latitude and longitude for all visible setting GPS satellites over one day

latitude and longitude positions of these events are depicted in Figure 3-12 (which uses the same color scale as Figure 5).

Another metric is the duration of occultations that pass within the atmospheric volume sampled by the radiometer. Figure 3-13 shows that the average occultation duration is 3.5 minutes, and all occultation opportunities will only last eight minutes or less.

3.3.2 Calibration Opportunities for other Low Earth Orbits

Using the orbits as described in Section 3.2, we analyze the potential radiometer overlap conditions. The metrics used in this study include the total number of overlapping occultations over three months of simulation as well as the location of those overlapping measurements on the Earth.

In Figure 3-14, we show that there is a slight orbital dependence on how well the radiometer calibration with the GPSRO instrument will perform. The numbers in that figure are the number of occultations that overlap within 100 km of the radiome-

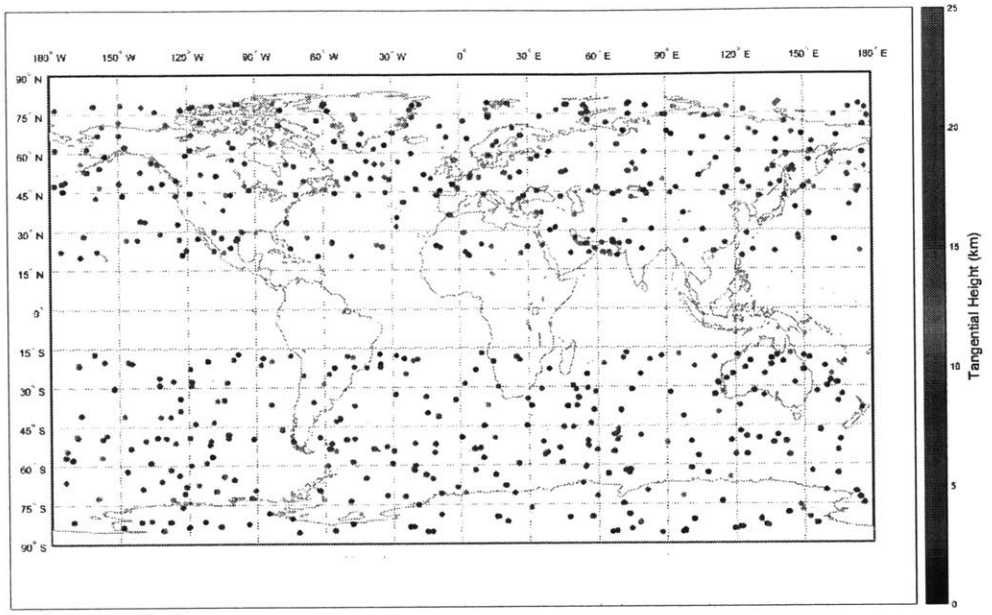

Figure 3-12: Tangential height (< 25 km) as a function of latitude and longitude for all visible setting GPS satellites within the radiometer field of view over three months

ter boresight (limb-facing) over 3 months. For comparison, the number expected for the MiRaTA mission (440 km × 811 km sun syncronous orbit) is around 900. All orbital configurations satisfy the one overlapping measurement per day requirement.

In Figure 3-15 we show how the distribution of overlapping radiometer and GPSRO measurements changes with orbit inclination. The results are intuitive based on the assumption of a nadir-facing radiometer boresight (overlapping observations are limited to the inclination range of the spacecraft). One interesting note is that for sun synchronous inclinations, the overlapping measurements do not occur within tropical latitudes.

3.4 Radiometer Calibration with Radio Occultation - Measurement Errors

GPS radio occultation, as introduced in Chapter 2, uses information on atmospheric and ionospheric delay in received GPS signals to measure the local pressure and

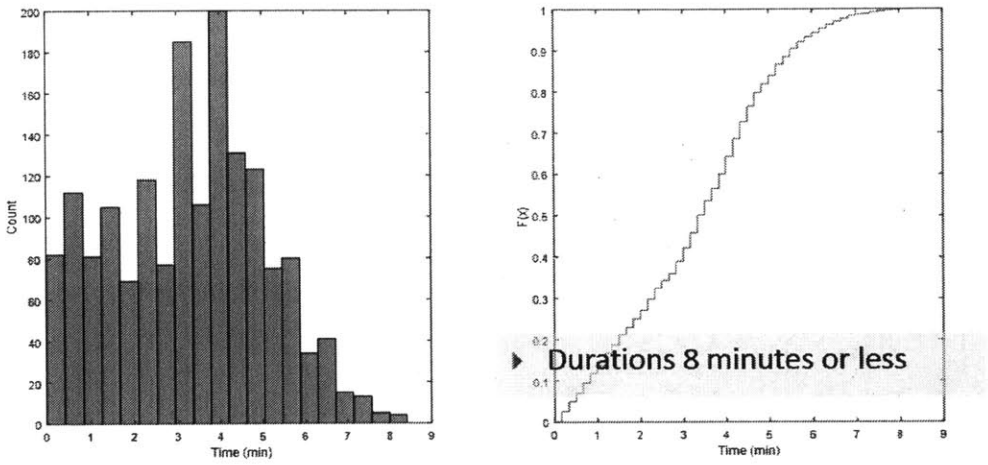

Figure 3-13: Histogram and CDF of expected overlapping occultation durations for the MiRaTA mission

	400 km	500 km	600 km	700 km
0°	255	478	438	197
30°	458	344	384	333
60°	298	254	248	249
98°	509	327	372	413

Figure 3-14: Number of occultations that overlap with a given radiometer field of view over 3 months

temperature of the atmosphere. Neutral atmospheric sounding has not yet been successfully proven on a CubeSat, though there are several missions that have flown or plan to fly instruments for this purpose [11]. The current state of the art for GPS radio occultation temperature precision is on the order of 0.1 K in the troposphere [27], and for the MiRaTA mission, the requirement is better than 1.5 K precision in order to calibrate the radiometer to the required levels as explained in Section 3.2.

Challenges of implementing GPSRO on a CubeSat include limited data processing and storage capability, and limited area and volume for a high gain dual frequency GPS receive antenna. The limited processing and data storage capability means it is generally easier to accommodate a closed-loop GPSRO receiver than an open-loop receiver.

In Section 3.1.3 we described the process by which the radiometer calibration is

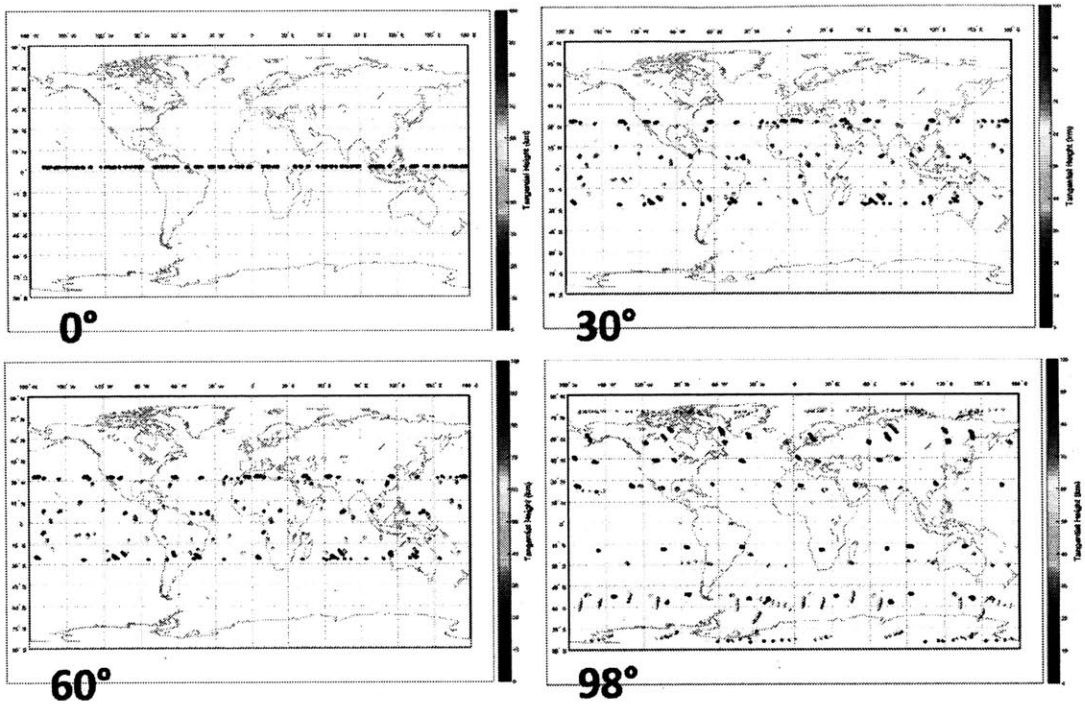

Figure 3-15: Latitude and Longitude Locations of Overlapping Radiometer and GPSRO limb measurements over three months (400 km altitude)

obtained using assumed GPS RO profiles based on the GPS MET mission. Here we assess the capability of the CubeSat-sized CTAGS instrument in providing measurements within the required error bounds.

3.4.1 Sources of Error in Radio Occultation

The analysis presented in this section only considers measurement error due to thermal noise. Table 3-1 summarizes the effects of several other sources of error for radio occultation sounding in the lower atmosphere [27]. The other main sources of error, particularly local multipath, horizontal along-track errors, ionospheric effects, and Abel boundary, are important to characterize but are dependent on the environment and measurement conditions or the retrieval algorithm rather than on parameters specific to the instrument hardware itself.

Table 3-1: Temperature error for a variety of noise sources based on the Kursinksi study of GPS-MET, with values specifically pulled for MiRaTAs altitude range of interest [27]. The conditions are: Thermal error, 1 s SNR(W) = 5e4; Local multipath, 10 mm rms spread over 0.01 Hz; Horizontal refractivity structure, along track from simulation and horizontal motion of ray path tangent point from tropospheric and stratospheric climatologies near 30S for June-July-August; Ionosphere error, daytime, solar maximum conditions; Abel boundary error, 7 % in α, 5 % in H_ϕ; Hydrostatic boundary error, 5 K; Tropospheric water vapor, 0 latitude with 8 km vertical correlation length

Noise Source	Temperature Error		
	10 km	20 km	30 km
Thermal Error	0.03	0.1	0.4
Local Multipath	0.07	0.2	0.5
Horizontal Along-Track	0.3	0.2	0.2
Horizontal Drift	0.1	< 0.01	0.03
Ionosphere day, solar max	< 0.01	0.2	0.7
Abel boundary, 5% H_ϕ	< 0.01	< 0.01	0.04
Abel boundary, 7% $d\alpha$	0.04	0.2	0.7
Hydrostatic boundary	< 0.01	< 0.01	< 0.01
H2O at 0 latitude, 0.5 km correlation length	< 0.01	< 0.01	< 0.01
RSS Temperature Error	0.6	0.4	1.1

3.4.2 Assessing Nanosatellite Temperature Retrieval Error

For this analysis we follow the framework set by of Hajj, et al., 2002 [132] to calculate bending angle precision based on the expected received SNRv (voltage signal to noise ratio) at CTAGS. Figure 3-16 illustrates the steps taken in this process.

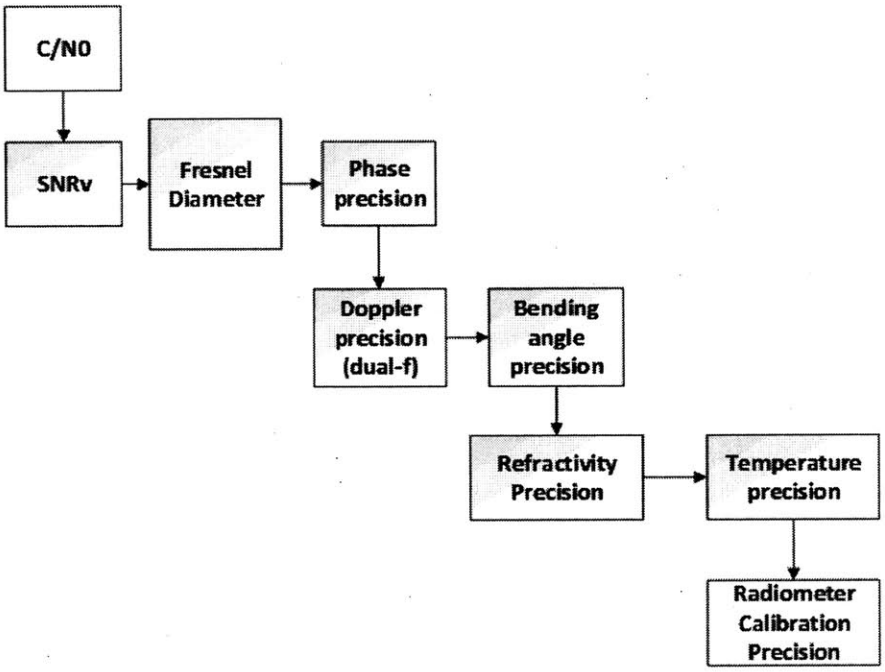

Figure 3-16: Process for estimating temperature precision for the MiRaTA GPSRO measurements based on thermal phase noise.

Due to the similarities between the MiRaTA mission and the GPS-MET instrument (closed-loop receivers, similar SNR), we compare our results to the simulated performance of that mission. The radiometer calibration analysis performed in [79] and summarized in Section 3.1.3 assumed stratospheric radio occultation retrieval accuracy of 0.4 K based on the error assessment made by Kursinski for the GPS-MET radio occultation instrument [27].

3.4.2.1 The CTAGS Instrument

The Compact TEC (Total Electron Content) and Atmospheric GPS Sensor (CTAGS) consists of a COTS GPS dual frequency (L1 at 1575.42 MHz and L2 at 1227.60 MHz)

receiver (NovAtel OEM628) with custom firmware modifications, a custom 3-element dual-frequency patch antenna array, and LNA/RF front-end. The CTAGS antenna is mounted on the MiRaTA spacecraft such that in local vertical local horizontal (LVLH) stabilized configuration, the antenna faces zenith.

The MiRaTA CTAGS payload is designed to accept customizable commands. Specifically, it allows differing sampling rates depending on the elevation and azimuth of the GPS constellation satellite location relative to MiRaTA. In the nominal operating mode CTAGS samples at 0.1 Hz for non-occulting satellites and 1 Hz for occulting. In the occultation mode, CTAGS samples at 50 Hz for occulting satellites and for a single above horizon reference satellite. For this mission, CTAGS provides exclusively setting or ingress occultations providing a solid lock on signals as they pass through the stratosphere and troposphere. Rising or egress occulting signals may not be locked on until they are well above the troposphere/stratosphere.

The use of a dual frequency receiver supports straightforward removal of clock errors and the effects of the ionosphere from troposphere and stratosphere observations.

3.4.2.2 SNR and Signal Acquisition

Signal to noise (SNR) calculations require an understanding of the link budget of the system. We start by confirming that the CTAGS instrument is able to receive signals through the atmosphere with enough SNR to lock and track the transmitting GPS satellite through a complete occultation event (i.e. signals encounter solid Earth). A link budget calculation supports this assumption and is included in Appendix B. The transmit power and gain are simulated using Analytical Graphics Inc. System Tool Kit (AGI STK) GPS transmitter models at L1 and L2 frequencies. The CTAGS antenna gain pattern was provided by The Aerospace Corporation during the design model phase for their custom array (maximum gain 9.7 dBi at L1 and 9.4 dBi at L2). The ideal pointing for the antenna is for the minimum elevation angle of observation (at or slightly below the limb of the Earth) to lie within the half power beamwidth (HPBW) of the antenna boresight. For an elliptical orbit, the ideal pitch-up angle

will vary with orbit altitude, but for the results in this work, the pitch-up angle is assumed to be a constant 115 degrees (pointed directly at the limb at an orbit altitude of 625 km).

Noise parameters were either calculated or taken from component datasheets. The system noise temperature includes antenna noise (150 K assuming that the Earth will be in half of the antenna field of view), receiver noise figures, and interference from other GPS satellites in the field of view (assuming total 200 K). The Novatel OEM628 receiver that was modified for the CTAGS instrument is a COTS component, and as such, specific noise parameters are proprietary information. While we will have as-measured values after testing, these are not expected to alter the result significantly, as the external low noise amplifier (LNA) noise dominates the receiver noise. Future studies will incorporate noise figures as measured from open-air (and eventually on-orbit) tests of the integrated system. Atmospheric losses are currently based on the ITU-R P676-9 model up to 100 km [133]. Bending due to refraction is not included in the current model.

The Novatel receiver can lock onto and acquire signals between 20 and 50 dB-Hz. We have accounted for all major losses, and while there are likely some loss contributions that are not fully captured, we can show that there is more than enough margin (>20 dB) for the receiver to the able to track through the atmosphere down to the required altitude. Our calculations are consistent with similar calculations done for GPS-MET [27].

3.4.2.3 Measured Bending Angle Error

In addition to considering the ability of the receiver to acquire and maintain lock, the voltage SNRv also impacts temperature error. From the Novatel receiver datasheet [88], for a sampling frequency of 20 Hz (0.05-s integration time) we can expect a thermal phase noise mean square error of 0.5 mm for the L1 frequency (and 1 mm for L2). From the following relationship

$$< \delta\psi(\tau)^2 >^{1/2} = \frac{\lambda}{2}\pi(2SNR_0\tau)^{-1/2} \tag{3.1}$$

where $< \delta\psi^2 >^{1/2}$ is the rms phase error (units of length), λ is the sampling wavelength (L1 or L2), τ is the integration time, and SNR_0 is the power signal to noise ratio based on a 1-second integration time ($SNR_0 = SNR_{v_0}^2$) [132] we calculate that the 1-second L1 SNRv of the receiver is 271 V/V (174 V/V for L2). The CTAGS instrument will be sampling at 50 Hz, but for retrieval measurements we assume that the integration time is the time it takes the signal to vertically travel a Fresnel diameter through the atmosphere. The Fresnel diameter is dependent on the SNRv and will vary as the signal gets lower through the atmosphere as shown in Equation 3.2.

$$Z_F = 2\sqrt{\frac{\lambda D_t D_r}{D_t + D_r}\frac{SNR_v}{SNR_v^0}} \tag{3.2}$$

where Z_F is the Fresnel diameter, λ is the wavelength, D_t is the distance from the transmitter to the tangent point, D_r is the distance from the receiver to the tangent point, SNR_v is the V/V signal to noise ratio through the medium (*e.g.* through the atmosphere), and SNR_v^0 is the V/V signal to noise ratio in a vacuum. As the signal penetrates deeper into the atmosphere the Fresnel diameter gets smaller, bettering the measurement resolution. In the upper troposphere and lower stratosphere, the Fresnel diameter is on the order of 200 - 500 m, and 1.4 km in free space.

We use the vertical speed of the tangent point during the setting occultation to calculate the integration time for each measurement - the time it takes the signal to vertically move a distance equal to one Fresnel diameter. The average integration time for the MiRaTA orbit (450 km x 810 km) is 0.5s, which corresponds to a 0.16 mm phase precision (0.32 mm for L2) as per 3.1. Phase precision feeds into Doppler noise and ultimately to bending angle precision through the following relationships [132]:

$$\sigma_{Doppler} = \frac{\sigma_\phi\sqrt{12}}{\Delta N^{3/2}} \tag{3.3}$$

$$\sigma_\alpha = \frac{\lambda\sigma_{Doppler}}{V_0} \tag{3.4}$$

$$\sigma^2_{\alpha_{neut}} = (2.54)^2\sigma^2_{\alpha_1} + (1.54)^2\sigma^2_{\alpha_2}\Delta N^{3/2} \tag{3.5}$$

where Δ is the time between successive measurements (50 Hz sampling), N is the number of samples averaged over one measurement, which we calculate based on Δ and the time it takes for the signal to cross one Fresnel diameter, V_0 is the vertical speed of the signal tangent point through the atmosphere in m/s, and the phase error σ_ϕ is in units of cycles. The neutral atmosphere temperature retrieval comes from the L1 frequency and L2 is used for ionospheric correction, but sampling at both frequencies contributes to the measurement error and is taken into account in Equation 3.5.

Figure 3-17 shows the estimated bending angle error ($\sigma^2_{\alpha_{neut}}$) through the neutral atmosphere as a function of tangential height for the SNRv values used above. In Section 3.4.2.4 we describe how this calculated bending angle propagates to temperature precision.

3.4.2.4 Calculating Nanosatellite Temperature Precision

The Abel transform [134] is applied to the bending angle to calculate refractivity, and then temperature can be derived using standard atmospheric temperature assumptions (for details see [131]). Our approach to the Abel transform was to use a low-noise power law approximation of atmospheric refractivity [Hinson, pers. corr. 2010]. We assume a one-degree bending at the surface [27] and a scale pressure height of 7.5 km [135]. Because the Abel transform of a power law function model input has an analytic solution, we can compare the analytic solution with numerical calculation to assess the contribution of the numerical calculation to the retrieval error. As shown in Figure 3-18, the numerical error contribution from performing the transform on a representative Earth bending angle profile is negligible.

The results from the bending angle error simulation represent the standard deviation of measured bending angle expected for the CTAGS instrument. We generate a Gaussian noise distribution with this standard deviation (0.3 nanoradians) and add

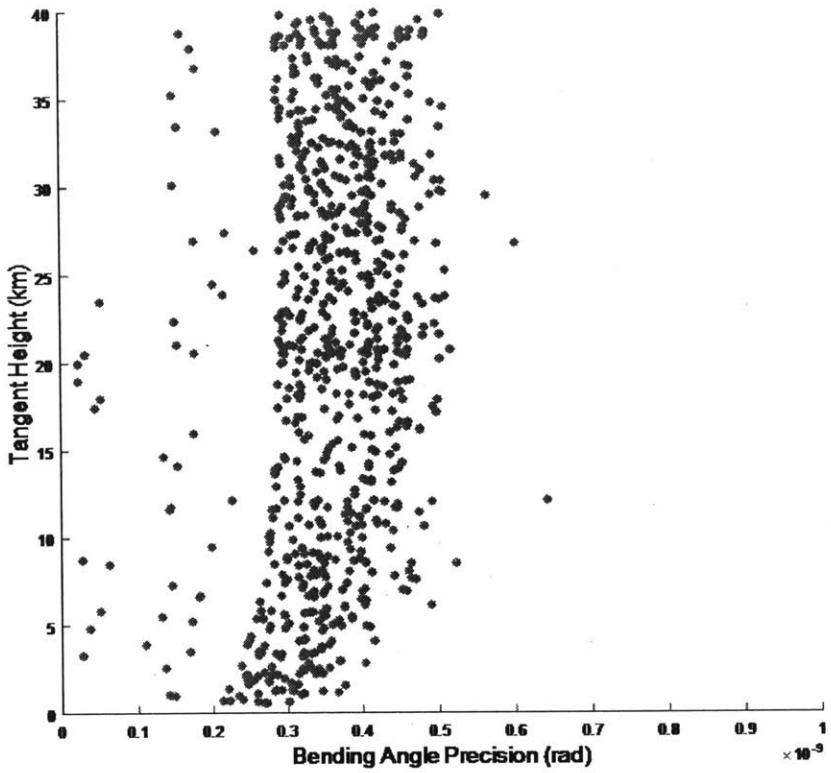

Figure 3-17: Bending angle precision vs. tangential height predicted for thermal noise error contributions (does not include atmospheric conditions, clock noise, position/velocity errors, or multipath effects)

it to a simulated vector of bending angles using the power-law approximation described above. Two vectors of bending angles vs. atmospheric height are fed into the Abel transform simulation, one with added noise, and one without. For this initial assessment we do not yet take into account any bias or offset in these measurements. Figure 3-19 shows the profile of the noise added to the power-law approximation of bending angle in the model. The temperature error that comes out of this (measured as the absolute difference between the results with and without the bending angle error) is between 0.1 and 1.7 K for the heights of interest.

The flight retrieval process will involve smoothing measurements across a Fresnel zone scale window. This smoothing process will reduce the observed data spikes in the current approximation.

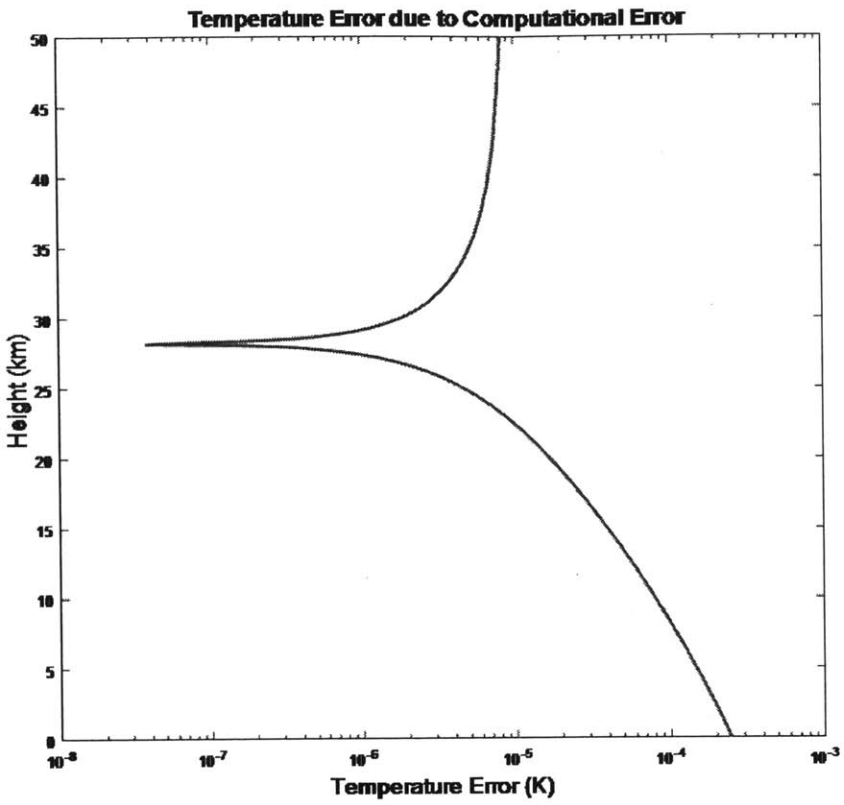

Figure 3-18: Error in temperature calculations due to numerical approximations in performing the Abel transform. For a detailed treatment of the radio occultation mapping kernel, see Ahmad 1998 [136]

3.4.2.5 Results

The MiRaTA mission requires a 1.5 K temperature retrieval precision in the neutral atmosphere through GPSRO measurements with a goal of 0.5 K precision. The 0.5 K goal would satisfy the conditions necessary to achieve a 0.25-K calibration of the radiometer in V-band as shown in [79] (note: the requirement for state of the art ATMS measurements is 0.75 K). The thermal noise error calculated in this simulation has a 95% confidence interval between 0.1 and 1.7 K. This thermal noise impact on temperature precision indicates that the CTAGS instrument should be able to meet its temperature retrieval requirements in support of radiometer calibration. At the lower end of the 95% confidence interval, the instrument has comparable performance

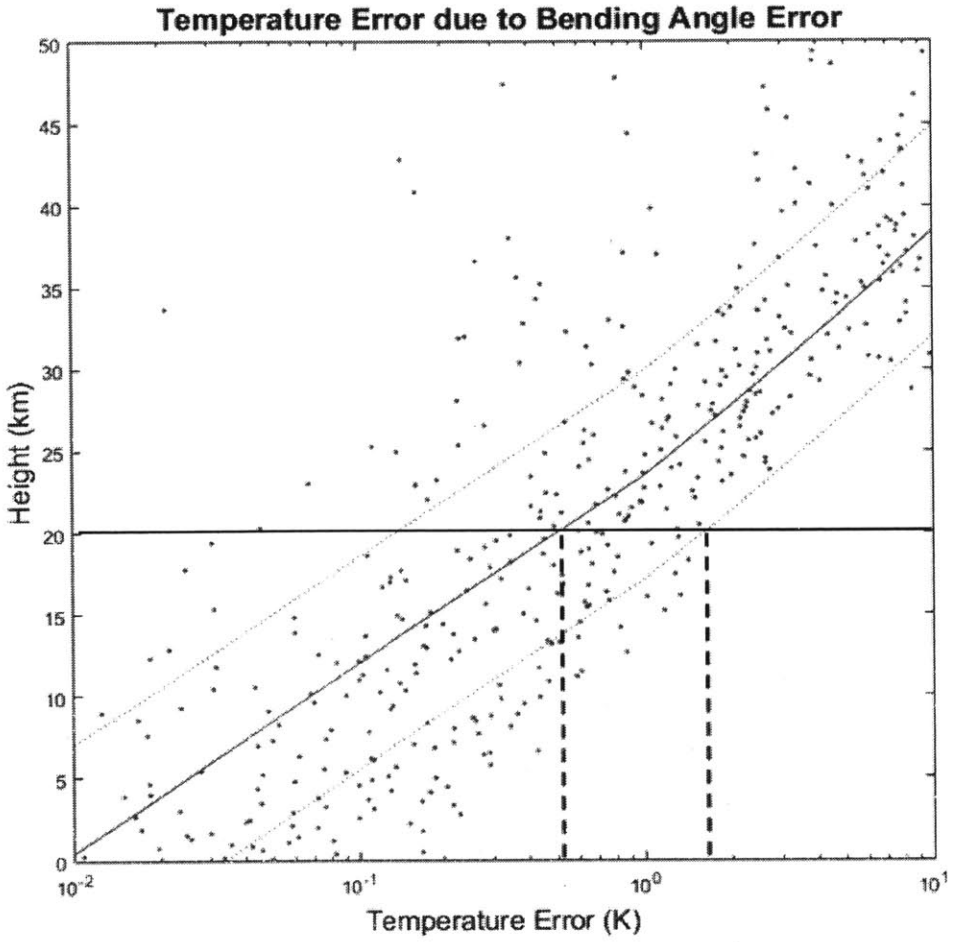

Figure 3-19: Temperature retrieval error with 95% confidence interval (red). The error used for input was based on thermal noise contributions and does not include atmospheric conditions, clock error, velocity/position errors, or multipath effects. It also does not include averaging performed in post-processing software.

to missions such as GPS-MET, which saw a worst-case overall temperature error of 0.4 K (taking into account more than just thermal error) at the altitudes of interest for MiRaTA [131].

Our analysis shows that from a hardware perspective, CTAGS performance should be able to contribute to an overall improvement of radiometer calibration state of the art on a CubeSat platform. There are still several sources of error that have yet to be characterized, and future analysis will include measurements from hardware testing as well as use of the planned mission retrieval software in order to assess the

end-to-end performance of the instrument. These results will better inform mission operations and the feasibility of meeting the science objectives.

3.5 Summary of Contributions

In this chapter we motivated the need for innovative calibration methods for passive microwave radiometers on nanosatellite platforms. One approach is to use GPS radio occultation measurements. We presented orbit architectures that provide global coverage for GPS radio occultation, both from a global measurement standpoint and the perspective of sounding in volumes that overlap with microwave radiometers. For both applications, high-inclination orbits yield greater return in number and global distribution of measurements.

We also presented the challenges associated with sounding into the neutral atmosphere with GPS radio occultation on a CubeSat platform. We developed a model to assess the error of temperature retrieval from the neutral atmosphere for the CubeSat-sized CTAGS instrument and showed that this instrument is capable of sounding down to the surface (the first such mission to do so on a nanosatellite platform). Based on a model we developed of the measurement precision due to thermal noise effects and design parameters of the COTS instrument, CTAGS is expected to achieve measurement precision between 0.1 and 1.7 K (95% confidence). This performance supports the goal of calibrating a microwave radiometer to state of the art levels or better.

Chapter 4

Nanosatellite Atmospheric Characterization

Like radio occultation, bending angle measurements of occultation of electromagnetic signals in optical and infrared regimes can be used to calculate atmospheric thermophysical parameters. Optical measurements through an atmosphere (or reflected by an atmosphere as in Exoplanet Direct Imaging) are also used to identify species and abundance in the atmosphere.

4.1 Laser and Stellar Occultation

Stellar occultation uses a distant star as the transmitting source and probes ring systems and atmospheres of an intervening body (planet, moon, asteroid). The main advantage of stellar occultation is that it enables km-level resolution for bodies in the outer solar system, which is unachievable with Earth-based observation systems.

Earth atmospheric characterization (as well as Venus) have been performed with solar occultation methods. A telescope in orbit around the Earth collects light from the sun as it sets, and by implementing a spectrometer or a set of filters observes the intensity of the received light to generate an absorption spectrum. The absorption spectrum gives information on the type and abundance of atmospheric constituents.

In this section we analyze potential mission architectures for achieving laser oc-

cultation measurements on nanosatellites in LEO. We present challenges of obtaining lower atmospheric occultation measurements, potential applications of adaptive optics to improve measurements, and observation opportunities for a range of orbit configurations.

Figure 4-1 shows the absorption spectrum of Earth's atmosphere over a range of infrared wavelengths.

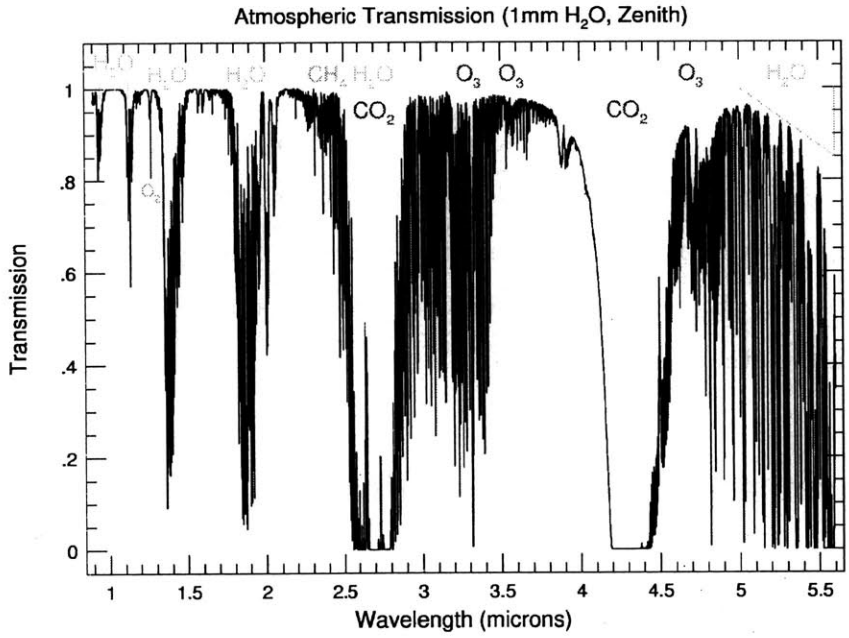

Figure 4-1: Earth atmosphere absorption spectrum for short wave infrared wavelengths

We do not specifically address the requirements of spectral resolution and post-processing techniques necessary to achieve the final data product, but those studies exist in the literature [89], [16], [137], [138].

4.1.1 Achieving Global Measurements with LEO Intersatellite Links

As was shown for radiometers and radio occultation payloads, here we do an analysis of how representative CubeSat orbits affect the observational opportunities for a mission with an optical payload for both astronomical imaging and intersatellite link/occultation opportunities.

We vary the orbit altitudes (400 - 700 km) and inclinations (30 degrees - Sun Synchronous, including retrograde orbits) of pairs of satellites. We calculate the number of occultation events that occur, the geographical location of these occultation measurements, and the rate of change of tangential height through the atmosphere. All the analyses were performed in STK with post-processing in MATLAB (see Appendix B).

Figure 4-2 shows the number of occultation opportunities available for each of the studied orbit pairs over three months. These numbers assume no initial RAAN offset for the satellites. There are several configurations for which the satellites never set with respect to each other, and more occultation events are observed with satellites in orbits with dissimilar parameters.

		400 km			500 km			600 km			700 km		
		30	60	SS	30	60	SS	30	60	SS	30	60	SS
400 km	30	965	1	965	11	71	271	21	68	279	31	67	289
	60		965	1	71	11	129	68	21	117	67	31	110
	SS				271	129	11	279	117	21	289	109	31
500 km	30				944	1	944	11	61	298	20	59	295
	60					944	1	61	11	109	59	20	99
	SS							298	109	11	295	99	20
600 km	30							924	1	924	10	54	301
	60								924	1	54	10	94
	SS										301	94	10
700 km	30										905	1	905
	60											904	1
	SS												

Figure 4-2: Number of setting occultations between pairs of satellites in varied orbits

There is a trade between total number of occultations and the quality of those occultations as seen in Figure 4-3.

Figure 4-4 shows how quickly an occulting signal will set through the atmosphere

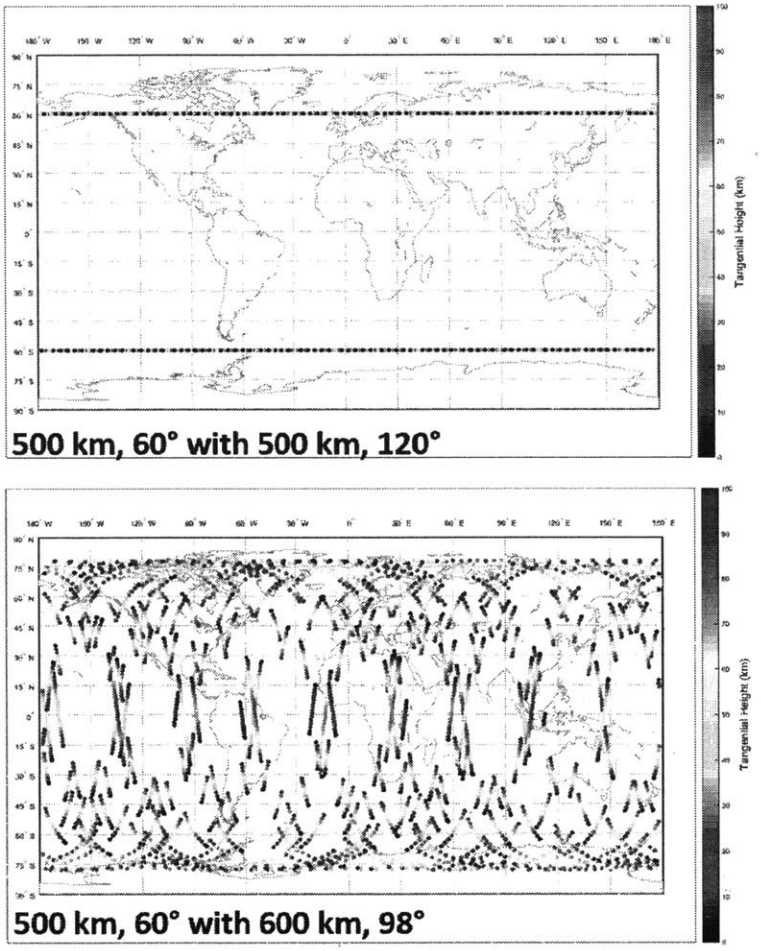

Figure 4-3: Geographical location of setting occultations for (top) a prograde/retrograde pair of satellites and (bottom) a mid-latitude and sun-synchronous satellite

for four main groups of dual-satellite orbital configurations. figure 4-5 shows the corresponding intersatellite range distributions.

From these studies, we see that within our orbit design parameters, for global occultation measurements with manageable setting rates and ranges, one satellite should be in a polar orbit and the other in a mid-inclination orbit.

There are several other factors to consider for the implementation and operation of an intersatellite laser occultation mission. Satellite location and pointing knowledge become more complicated for satellites in vastly different orbits.

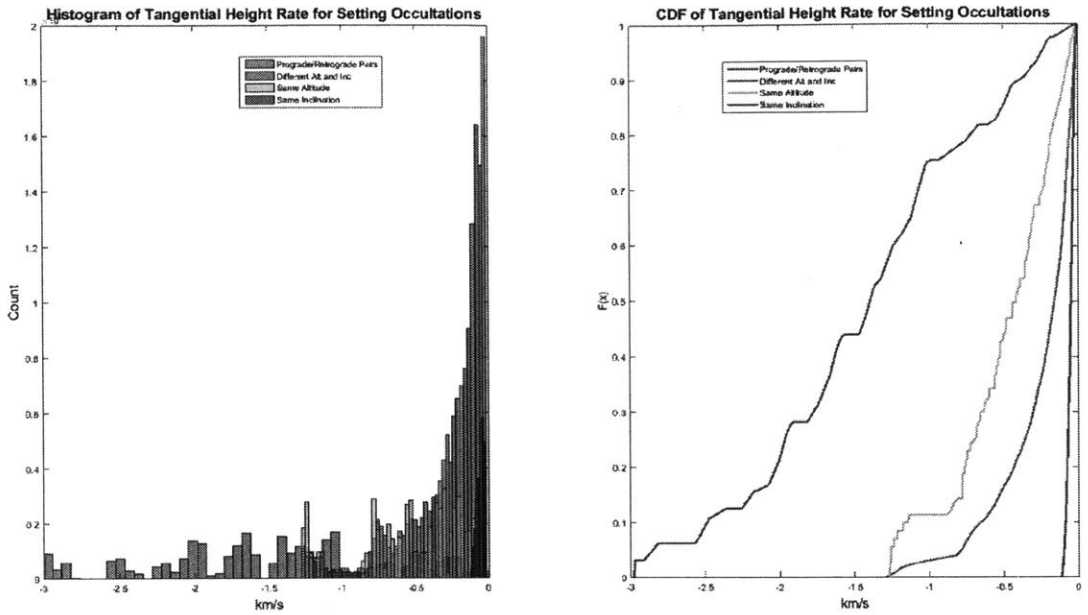

Figure 4-4: Histogram and CDF of tangent height rates during setting occultations for several dual-satellite configurations

4.1.2 Sources of Error for Laser Occultation - Atmospheric Turbulence

Atmospheric modeling for signals traversing vertically through the atmosphere has been developed extensively both for astronomical and optical communications applications. Turbulence on a horizontal (cross-link) path is less well known. Previous work [89] [16] [139] has shown that the primary disturbances in atmospheric transmission are manifest as coherence loss, beam spread and beam wander, and that turbulence-induced error is significant for narrow beams (divergence angle around 1 μrad). For laser occultation and intersatellite communications links, the beam divergence will be about an order of magnitude larger (30-40 μrad) for 9-cm apertures. Turbulence is most significant in the lower troposphere where the concentration of water vapor is highest.

We are interested in characterizing the turbulence profile that a laser crosslink will see as a function of tangential height. The parameters studied here are the Fried parameter, r_0 and Greenwood frequency, f_G, which can be used to calculate the

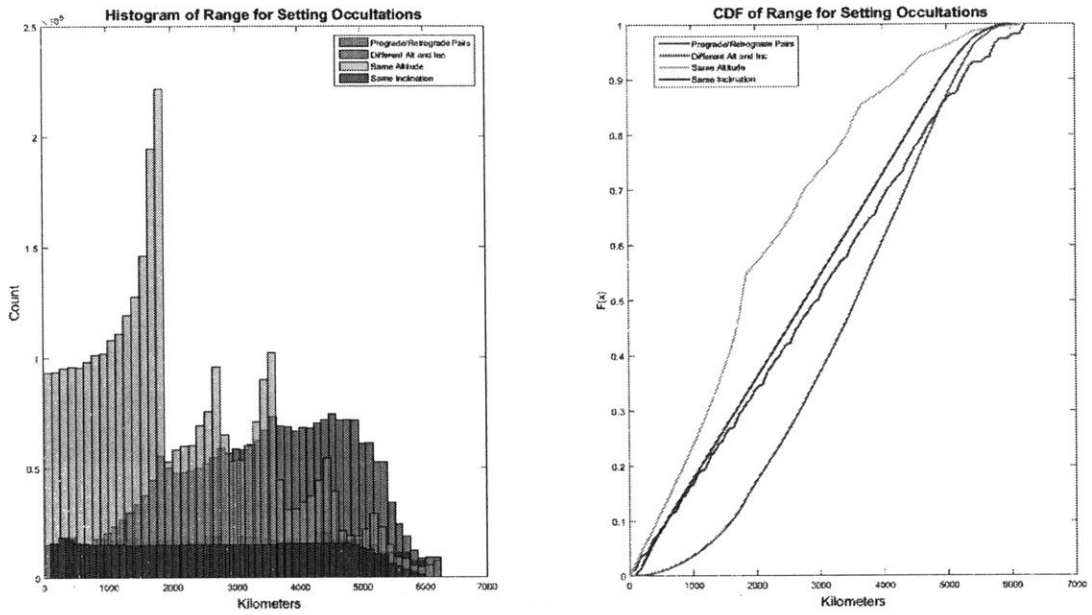

Figure 4-5: Histogram and CDF of access range during setting occultations for several dual-satellite configurations

degrees of freedom and response rate from an adaptive optics system as described in Section 4.1.3.

4.1.3 Turbulence Calculation Approach

Our approach is to model the Earth's atmosphere as a series of thin shells and calculate the expected turbulence in each shell. We integrate over the path of the crosslink signal to determine the total effective turbulence encountered. Figure 4-6 illustrates this concept. Once calculated, the turbulence profile is treated like a thin phase screen in the subsequent calculations.

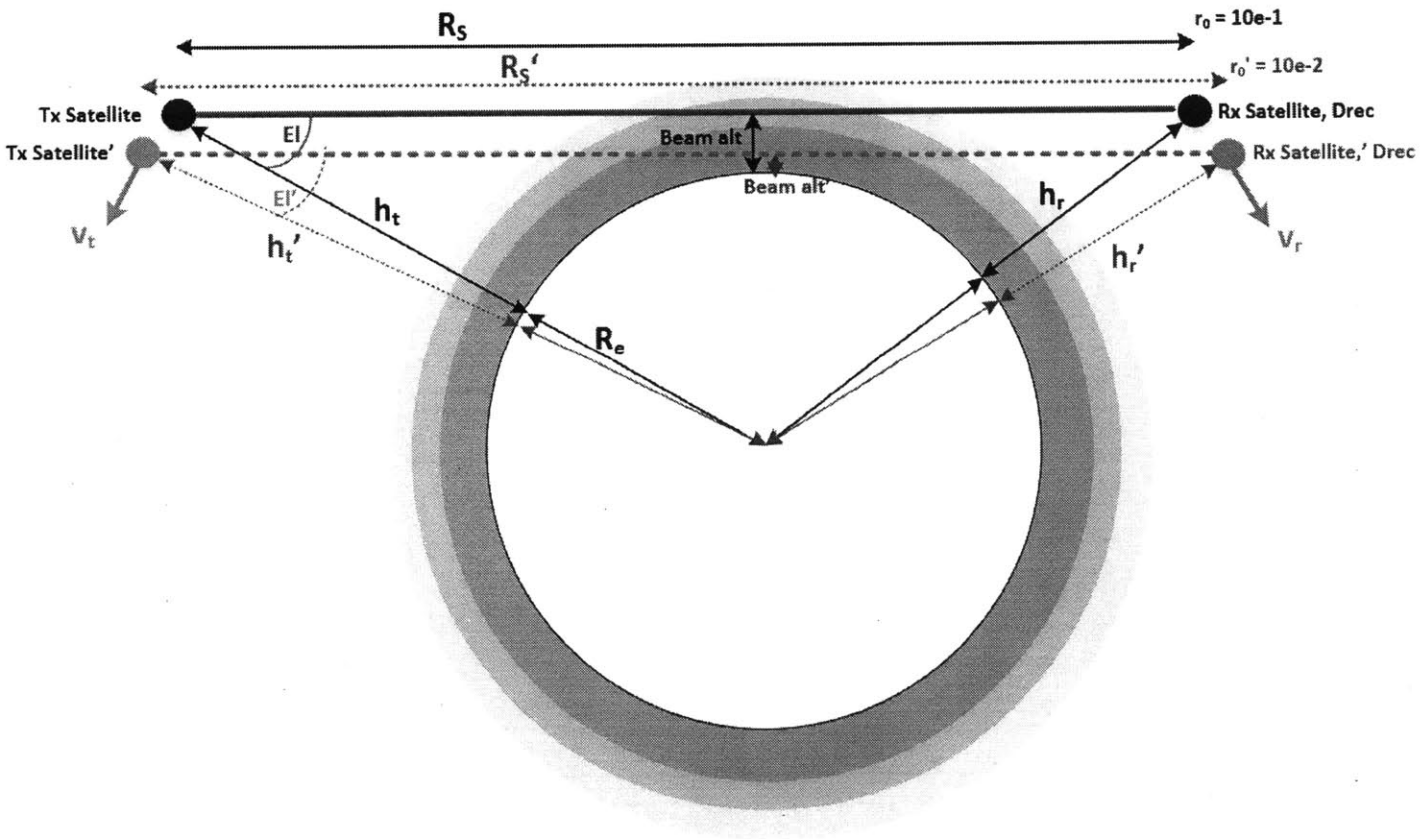

Figure 4-6: Diagram of intersatellite laser occultation through layers of the atmosphere

The parameters of interest in this model unique to the intersatellite link architecture (compared with ground or air-based systems) are the relative velocity of the transmitter and receiver and the slant range. The model is adapted from atmospheric modeling performed at Lincoln Laboratory (pers. corr. Youmans, 2016) and is based on the atmospheric model described in [139].

The tangential height (depicted in Figure 4-6 as 'beam alt') depends on the geometry of the transmitting and receiving satellites. In the model, we vary the elevation angle of the transmitted signal (elevation measured from nadir-pointing as shown in Figure 4-6). For tangential heights of 0-100 km, the elevation angle for a satellite at 500 km altitude ranges from 68-70 degrees, as shown in Figure 4-7.

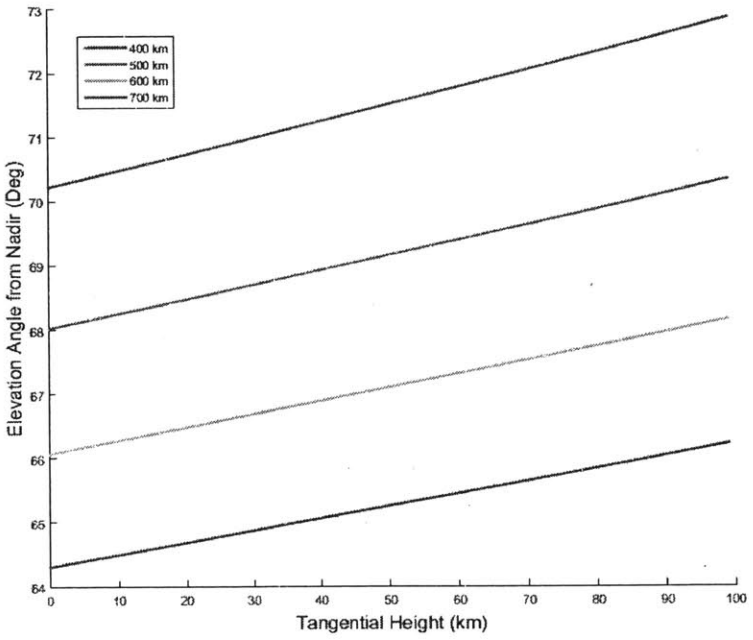

Figure 4-7: Elevation angle from the transmitting satellite (nadir = 0 degrees) for tangential heights of interest

There are several assumptions built into the model that can be improved for a more detailed future analysis. We currently assume a Komolgorov atmosphere, and we have not varied the relative velocities of the spacecraft. The calculations done are for a laser transmission of 1550 nm.

4.1.3.1 Refractive Structure Index

We first calculate a vertical profile of the refractive structure index, C_n^2, a parameter that represents how the refractivity of the atmosphere varies over the propagation path. Ground-based imaging applications assume a Komolgorov profile for atmospheric turbulence. We do the same and calculate a Hufnagel-Valley approximation modified with the Gurvich model for upper altitudes as described in [139]. Figure 4-8 shows what the refractive structure index looks like as a function of atmospheric height.

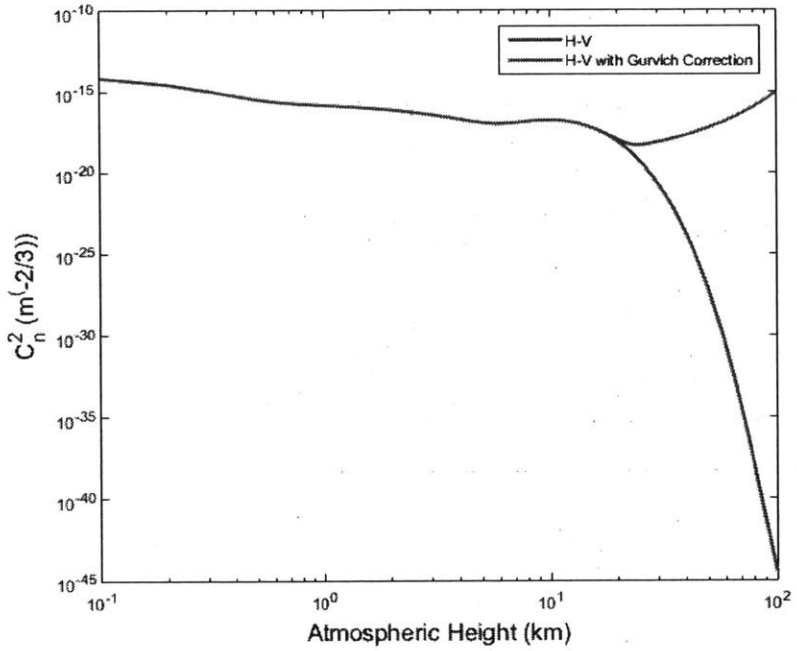

Figure 4-8: Refractive Structure Parameters for several models. We assume a Hufnagel-Valley model modified with the Gurvich correction for upper altitudes [139]

4.1.3.2 Fried Parameter

The Fried parameter (turbulence coherence length), r_0, represents the propagation distance over which the transmission maintains an acceptable degree of coherence. A lower value of r_0 is indicative of a more turbulent medium. It is calculated from

the zero-order turbulence moment, the integral of the refractive structure parameter through the height of interest, and it is wavelength-dependent. Figure 4-9 shows how the coherence length changes as a function of crosslink tangential height for a 1550 nm beam.

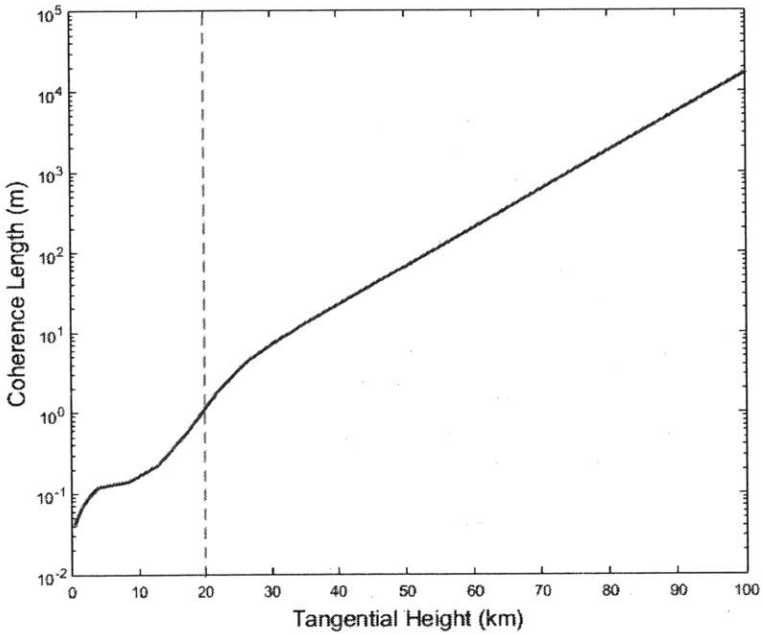

Figure 4-9: Coherence Length for an Intersatellite Crosslink as a Function of Tangential Height. The dotted line denotes the altitude below which we want to sound.

4.1.3.3 Greenwood Frequency

The Greenwood Frequency is a characteristic frequency of atmospheric turbulence [140]. In a single layer of turbulence, it can be approximated as:

$$f_G = 0.427 * v/r_0 \tag{4.1}$$

where v is the wind velocity in the turbulence layer, though in practice, the relative satellite velocities will dominate the wind velocity (as seen in Figure 4-4). The relationship between Greenwood frequency and tangential height is shown in Figure

4-10.

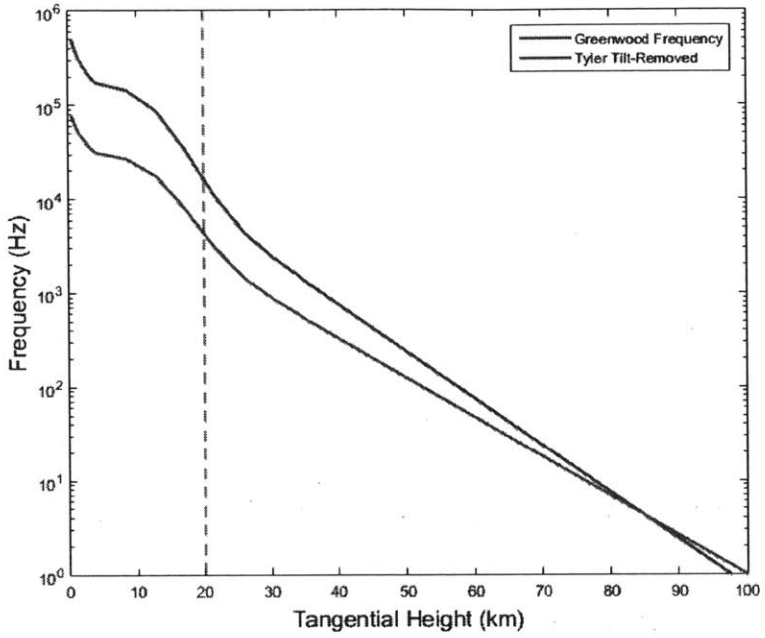

Figure 4-10: Greenwood Frequency (and Tyler-Tilt Removed Frequency) as a function of Tangential Height. The dotted line denotes the altitude below which we want to sound.

The Greenwood Frequency can be used to characterize wavefront control errors based on the control bandwidth of the adaptive optics system and the time scale of mirror actuation.

4.1.4 Adaptive Optics System Correction and Error

Errors in adaptive optics systems can be both spatial and temporal and come from mismatching in either the magnitude or frequency of correction. In order to correct for wavefront aberrations, a deformable mirror needs to have control authority on the same scale as the amplitude and spatial frequency of the required phase correction, and the wavefront sensor needs the dynamic range necessary to measure wavefront error. The Boston Micromachines MEMS deformable mirrors can typically manage 1.5 –5.5 μm of stroke, and the actuator pitch is 300 μm.

The error associated with fitting the mirror to the measured wavefront is given by:

$$\sigma^2 = 0.24 * (d/r_0)^{5/3} \tag{4.2}$$

where d is the projection of the mirror actuator pitch onto the telescope aperture, and the error term is in units of $radians^2$. The coefficient comes from empirical data assuming that the influence function of the actuators is approximately Gaussian [140]. Figure 4-11 shows what the resulting correction error is for four different mirror sizes available through Boston Micromachines –32-actuator, 144-actuator, 492-actuator, and 952-actuator (all 300 μm actuator pitch) –for a nanosatellite with a 9 cm aperture.

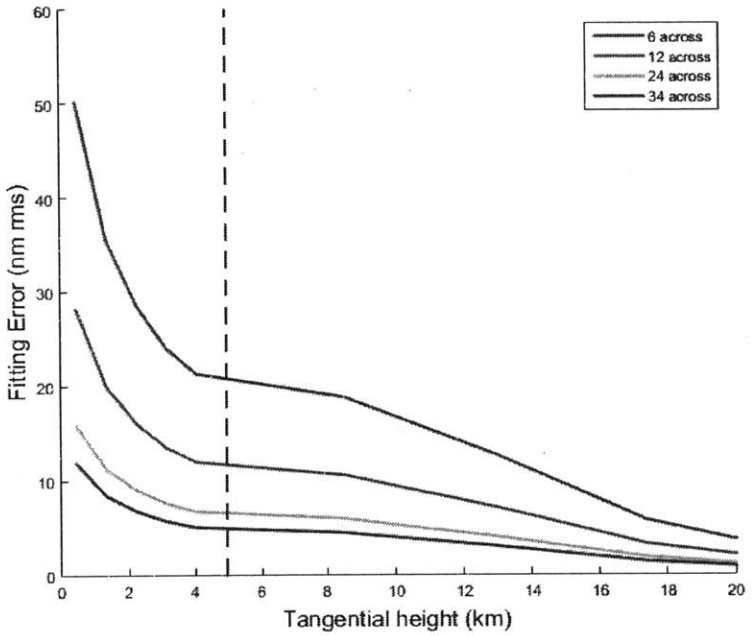

Figure 4-11: Wavefront fitting error for different mirror architecture options. Below 5 km (dotted line) is the optimal desired sounding depth

Fitting error is only one source of error that need to be accounted for in adaptive optics systems. Others include wavefront sensor measurement error, temporal error, angular isoplanatic error, atmospheric dispersion, and phase error due to residual tilt. Temporal error is dependent on the Greenwood Frequency and limitations due

to system servo bandwidth and time delays. Equation 4.3

$$\sigma_s^2 = \kappa * \frac{f_G}{f_S}^{5/3} \tag{4.3}$$

where f_S is the servo bandwidth and κ is a coefficient that depends on the behavior of the servo bandwidth cutoff [140].

The total wavefront error in the system impacts the performance of an adaptive optics wavefront correction system. The system performance is characterized by the Strehl Ratio:

$$S = e^{-\sigma_p^2} \tag{4.4}$$

where σ_p^2 is the total wavefront error variance. The expression of Strehl in Equation 4.4 is commonly called the extended Marechal approximation [140]. Figure 4-12 shows the Strehl ratio through the atmosphere as a function of tangential height for different numbers of actuators when only fitting error is taken into account. Figure 4-13 shows the Strehl ratio based on temporal errors assuming a fairly high control bandwidth of 2 kHz. At altitudes below the stratosphere, the temporal contribution to the error term is very large, driving down the attainable Strehl ratio.

4.1.5 Feasibility of Adaptive Optics for Crosslink Correction

We performed a preliminary analysis of the turbulence environment of intersatellite crosslink architectures. Based on the results, the correction requirements for a nanosatellite-scale aperture (9 cm without deployables) can be accomplished by a coarsely actuated mirror with neglible fitting errors. While the error due to fitting is manageable, temporal errors based on the servo bandwidth make sounding into the troposphere infeasible.

As deployable aperture architectures and larger nanosatellites are further developed, adaptive optics technology may be useful for enabling crosslinked laser occultation deeper into the atmosphere. As a technology development platform, nanosatellites can validate in-space use of MEMS DMs for use on future spacecraft.

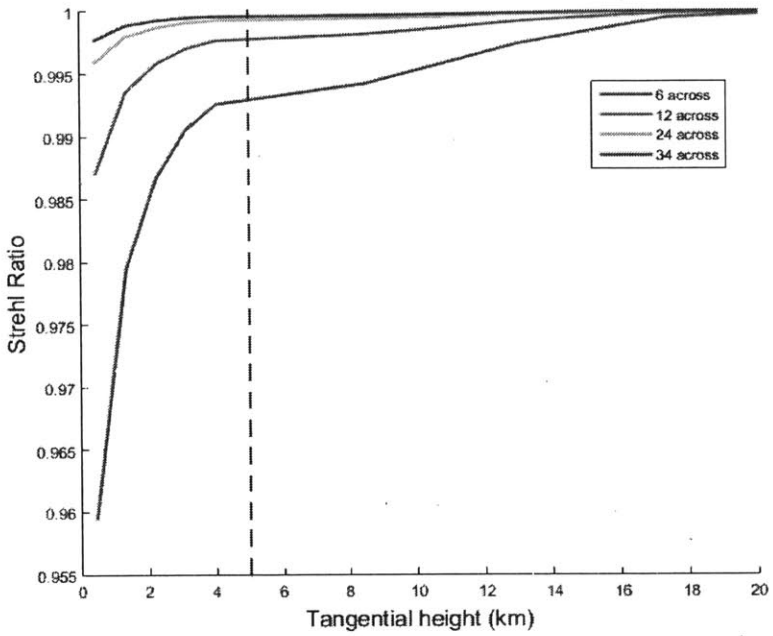

Figure 4-12: Strehl ratio from fitting error only for different sizes (number of actuators) of MEMS deformable mirrors. Below 5 km (dotted line) is the optimal desired sounding depth

4.2 Exoplanet Direct Imaging

Atmospheric characterization of outer planets and exoplanets through direct imaging is done by measuring reflection absorption spectrum, versus transmission absorption spectrum obtained through occultations. Figure 4-14 shows what reflected light from Earth's atmosphere looks like over a spectrum of near-infrared frequencies.

Exoplanet Direct Imaging is an active area of research. Observing dim planets with very small angular separation to a bright parent star requires high precision optics and wavefront control systems.

4.2.1 Principles of High-Contrast Imaging with AO

In order to observe a faint object at very close angular separation to an object 10 orders of magnitude brighter, the bright light must be blocked from the system. This can either be done with a star shade or an internal coronagraph [141] as shown in

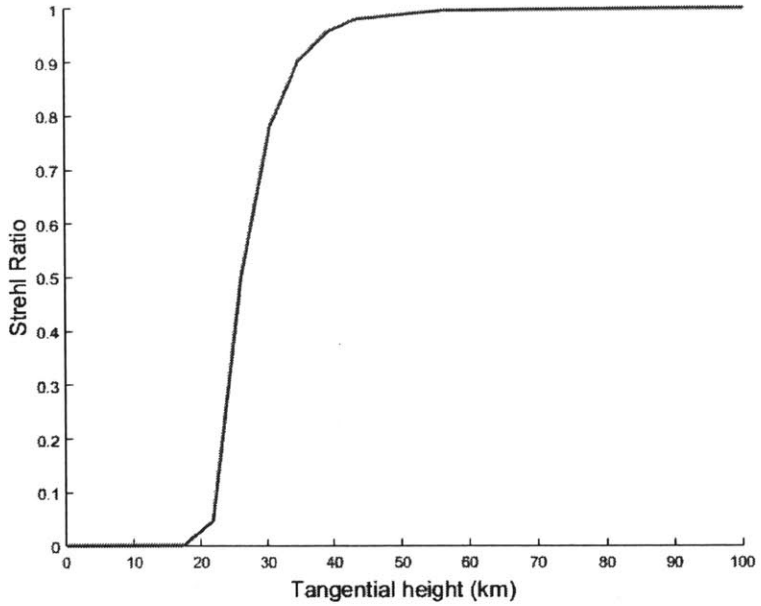

Figure 4-13: Strehl ratio from temporal error as a function of tangential height. Temporal error dominates the system in the troposphere, making sounding at low altitudes challenging.

Figure 4-15.

For a perfectly stable system with no surface roughness or mechanical imperfections, this would be sufficient to acquire images of dim sources. In real optics, surface errors, edge diffraction, and supporting structures (spindles) cause speckles and stray light from the star to escape the occulting spot and be imaged on the detector as shown in Figure 4-16.

Digging dark holes and correcting for aberrations due to thermomechanical issues typically happen on long timescales compared with atmospheric correction, but high spatial frequency is still an important requirement. The number of actuators across a deformable mirror drives the angular separation that can be observed on the detector. The more actuators across the aperture, the larger the Field of View where speckles can be nulled.

The angular separation of exoplanets from parent stars also drives the telescope aperture diameter [54]. Apertures under about 2 m start to be less useful for observ-

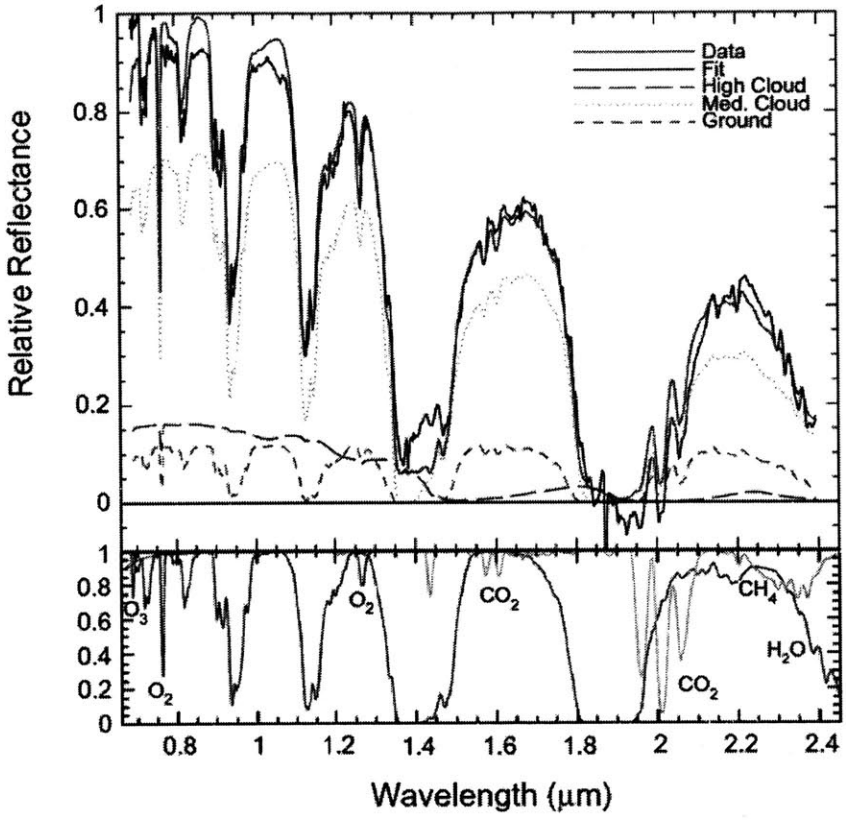

Figure 4-14: Earth atmospheric reflection absorption for short wave infrared wavelengths [141]

ing planets in the habitable zone of a star (with an exception for Alpha Centauri, which is close enough that an aperture of 30 cm is potentially useful [56]). For this reason, nanosatellites are infeasible platforms to perform direct imaging, but they are useful platforms for demonstrating the required technology needed on larger space telescopes, namely high actuator count MEMS deformable mirrors.

4.3 Nanosatellite Deformable Mirror Validation

MEMS deformable mirrors offer technology enhancements critical to achieving high-contrast imaging of Earth-like exoplanets on a space telescope. Wavefront measurement and control may also be useful in improving intersatellite link laser occultation measurements. To reduce risk and understand their behavior in a space environment,

these devices must be flown and tested in a relevant space environment.

4.3.1 Need for Space Qualification

Space is a hostile environment - it is a cold vacuum, and depending on the orbit a satellite is surrounded by plasma and sees a flux of highly energetic particles from the sun or the galactic.

The launch environment is also a potential source of failure for sensitive components, inflicting intense vibrations and acoustics and shocks on the payload. Some instruments require helium purging of the payload fairing as well. The main concern with MEMS deformable mirrors in a launch environment is the electrical connections and plastic deformation of the supporting structure [116].

MEMS deformable mirrors have been operated in vacuum and undergone vibration tests to increase their space readiness. These tests have been successful so far, but there has been no testing of how the temperature fluctuations or high radiation environment of space will affect the devices.

From an operational standpoint, it is also useful to understand how to diagnose and adjust operations if an actuator were to become stuck. On the ground, there are several human-in-the-loop solutions, but in space all debugging and correction would have to happen remotely.

4.4 Summary of Contributions

We address the challenges and requirements associated with atmospheric characterization with laser occultation and Exoplanet Direct Imaging. Laser occultation requires signals that pass through the lower atmosphere and must differentiate between attenuation caused by atmospheric turbulence and attenuation caused by absorption features of species in the atmosphere in order to measure percent content and atmospheric composition. Exoplanet Direct Imaging involves collecting light from a faint source (planet) close to a very bright object (star). In order to collect reflected light from the planet and analyze absorption features, the bright star light must be blocked

and suppressed in the region of interest.

Both of these measurement approaches can benefit from adaptive optics. Laser occultation could benefit from characterization and removal of aberrations and distortions caused by atmospheric turbulence, though more analysis is needed to determine the effects of turbulence on low-altitude crosslinks. For Exoplanet Direct imaging, speckle nulling and correction for thermomechanical distortions are the key applications for adaptive optics systems, and these corrections are on much longer timescales and require comparatively small stroke. Both laser occultation and Exoplanet Direct Imaging require the use of high actuator count deformable mirrors in order to correct for high-order aberrations (laser occultation) and to null speckles far off-axis on the detector (direct imaging).

In the next chapter we introduce a nanosatellite-compatible design for a technology demonstration of a MEMS deformable mirror. Adaptive optics on nanosatellites can be applied to both improving atmospheric sounding and enabling future space telescope missions with the capability to achieve high contrast imaging of objects several orders of magnitude dimmer than is achievable on Earth.

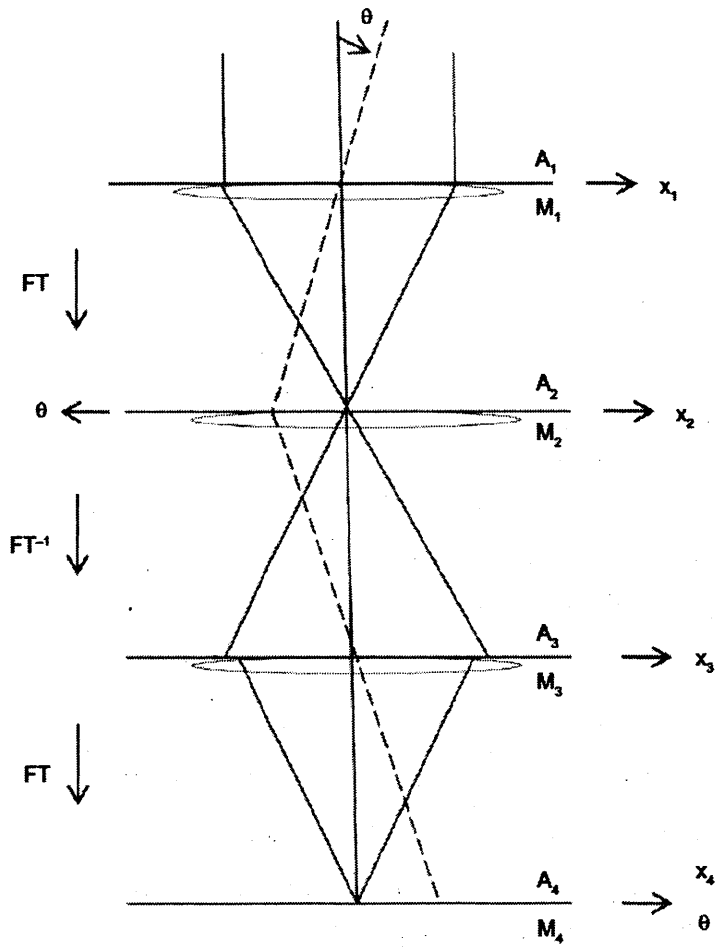

Figure 4-15: Example architecture of a coronagraph. A Telescope is configured in a 4f system and on-axis light is blocked at the focal plane by a small opaque spot, allowing dimmer light from an off-axis object to reach the detector. Adaptive from [141]

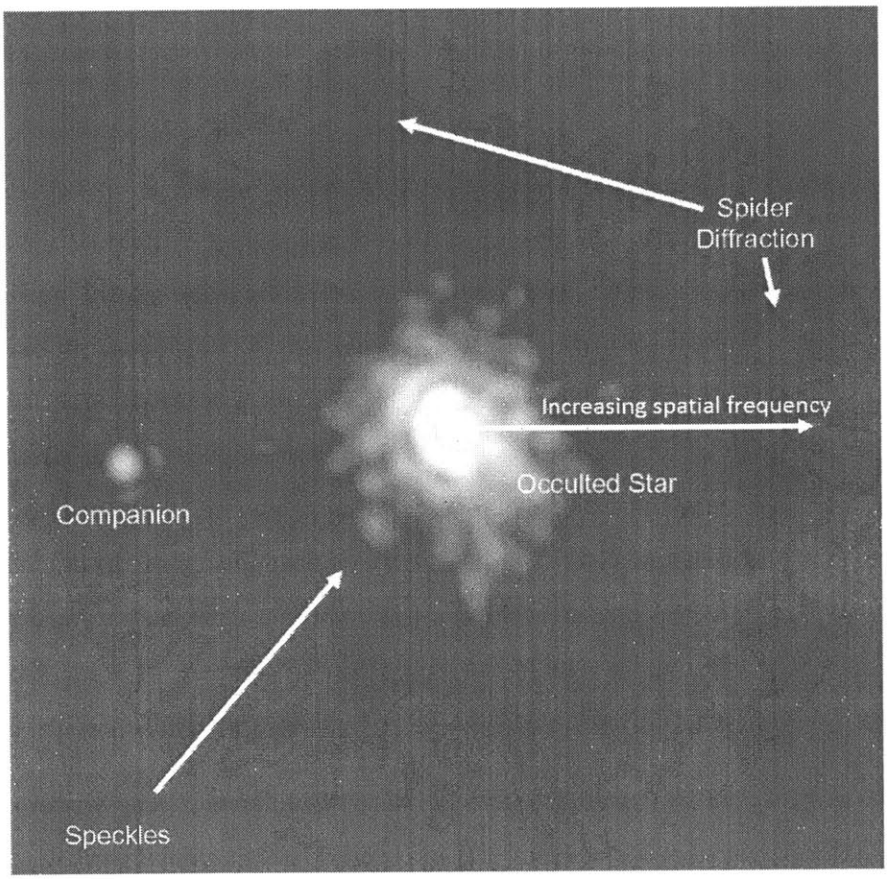

Figure 4-16: Speckles and spider diffraction on an occulted star with a binary companion (Adapted from [141])

Chapter 5

CubeSat Wavefront Sensor Design to Enable Earth and Exoplanet Atmospheric Characterization

As shown in Chapter 4, atmospheric characterization to understand both Earth and Exoplanets can benefit from adaptive optics systems. On a space platform, each of these applications brings a different set of requirements - atmospheric characterization requires fast measurement and correction that can be relatively large in amplitude, while Exoplanet Direct imaging requires high spatial frequency correction on slower timescales to negate thermomechanical disturbances and enable observations at high levels of contrast. Nanosatellites offer both a platform to demonstrate in-situ correction for Earth-based measurements from Low Earth orbit and a platform to test and characterize technology required on future space telescopes for high-contrast imaging.

This chapter focuses on DeMi - a CubeSat **De**formable **Mi**rror Demonstration mission. This mission is primarily a technology demonstration for MEMS deformable mirrors, but adaptive optic technology on a nanosatellite platform can also be used to improve intersatellite links and obtain occultation-based atmospheric measurements. We present an overview of the techology demonstration mission, including requirements and detailed payload architecture. Chapter 6 presents in-laboratory hardware validation of this design.

5.1 DeMi Mission Overview

The development of a space telescope equipped with a high performance coronagraph and deformable-mirror wavefront control system that is capable of the 1×10^{10} contrast needed to directly image Earth-like exoplanets is expected to be on the order of several hundreds of millions of dollars to over a billion dollars [54]. The goal of the CubeSat Deformable Mirror Demonstration is to provide a low-cost way to quickly test small, low-power, higher actuator-count deformable mirror technologies over extended periods of time on-orbit and raise their technology readiness level (TRL) for use on larger, more capable space telescopes.

While several important environmental tests can be performed using these mirrors on the ground (thermal vacuum, vibration, life cycle testing, and to a limited extent, radiation), it is important to demonstrate that simple wavefront control systems utilizing new deformable mirror technologies have stable, well-calibrated, and predictable performance on orbit. This is particularly important to emphasize, as there is no opportunity to tweak or adjust a wavefront control system on orbit after launch. It is also important to fully develop robust flight software to control these mirrors and systems, to incorporate them as sensors with spacecraft ADCS, estimators, and fine pointing algorithms, and to determine how best to capture performance and calibration data along with science observations and transmit it to the ground, as well as to monitor for degradation in performance over time and assess the rate of failures, potential causes of failures, and the impact of failures or anomalies on performance [116]. Nanosatellite experiments with MEMS deformable mirrors are also useful in starting to characterize how well the mirrors can be used to obtain information about stellar point spread functions (PSFs) and their variability.

5.1.1 DeMi Mission Goals

NASA characterizes technology planned for use in space by its Technology Readiness Level [112]. To reduce program risk, critical components on large-scale missions must be at TRL 6 or higher before system integration. A successful flight of the CubeSat

Deformable Mirror Demonstration would raise the technology readiness level (TRL) of a BMC Mini (32-actuator) Deformable Mirror to TRL 7 (analog mission flown in a relevant space environment). As a technology demonstration, this mission will not perform any high-contrast imaging from the nanosatellite platform. Rather the goals of DeMi are to :

1. Characterize and calibrate the performance of a MEMS deformable mirror over a long-duration on-orbit mission
   (a) Measure mirror surface to <100 nm
2. Demonstrate the use of these mirrors as intended for high contrast imaging
   (a) Correct in situ aberrations to < 100 nm rms

The mirror performance will be assessed based on the observed mirror response to commands (time and deflection). Successful demonstration will be determined based on the ability of the mirror to correct an image or a signal using closed-loop control. The degree to which the mirror is expected to correct will be determined through hardware experimentation as well as optical modeling. The optical modeling will incorporate expected operational conditions as well as satellite platform stability, a subject for future work.

The mirror chosen for demonstration is the Boston Micromachines Mini DM (32 actuators). A 64 × 64 array with the same technology from this manufacturer is currently used on the Gemini Planet Imager (GPI) [46], and the PICTURE missions [48] have flown kilo Boston Micromachines deformable mirrors.

5.1.2 DeMi Operation

DeMi will be launched into a low-earth orbit as an auxiliary payload. The baseline orbit design for this mission is 415 km altitude, 52-degree inclination based on International Space Station CubeSat deployments (exact orbit unknown). From this orbit the satellite will have an expected operational lifetime of approximately 4 months.

There are two modes of operation for the satellite experiments: mirror characterization with an internal source, and observation and image correction of a bright star through an external aperture. While the mirror characterization goals can be achieved with an internal source, the ultimate goal of using this technology on space telescopes motivates the use of an external aperture in demonstration. The observation environment in space is harsher than on Earth, and effects from energetic particles and extreme UV radiation that could enter the system interact with the mirror can be better characterized with the addition of an external aperture. The inclusion of an external aperture also drives the CubeSat system design in a way that would bring value to future wavefront sensing space telescope missions, such as developing the ADCS algorithms that include both pointing and closed-loop wavefront control.

For the first part of the mission, an internal laser illuminates the mirror to characterize the performance of the deformable mirror through open-loop actuator deflection measurement and closed loop correction with a Shack-Hartmann wavefront sensor. Once the mirror has been characterized, the telescope will target bright stars and use the deformable mirror for closed-loop image correction based on the quality of the focal plane image. The intended targets for star imaging are very bright objects such as Vega, Alpha Centauri, Arcturis, Sirius, and Canopus, but the feasible targets for this mission depend on the final design. The external observation requires much finer pointing and stability control than the internal laser experiment.

The intended experiments are defined based on the source and detector used, as summarized in Table 5-1. Each of the experiments is designed to measure an aspect of mirror functionality necessary to characterize its on-orbit performance. The desired outcome of these experiments inform more specific subsystem and component requirements for the DeMi CubeSat optical payload. The metrics measured are based on characterization of deformable mirrors on ground-based adaptive optics systems [43]. The metrics of interest for mirror characterization are corrected and uncorrected mirror surface figure, actuator stroke, and actuator influence function (how each actuator affects the behavior of the surrounding membrane). The control-loop performance requirements are driven by the expected system disturbances (magnitude

and frequency).

Table 5-1: DeMi Optical Payload Experiment Summary

Experiment	Source	Sensor	Purpose
0	Internal Laser	Wavefront Sensor	Open and closed-loop mirror characterization
1	Internal Laser	Focal Plane	Closed-loop wavefront sensing and correction demonstration
2	External Object	Focal Plane	Closed-loop imaging, wavefront sensing and correction demonstration

5.1.2.1 Experiment 0: Mirror Characterization

Experiment 0 (Table 5-2) characterizes basic mirror functionality with the internal source and wavefront sensor. This is an open-loop experiment that would run at intervals throughout the mission lifetime in order to characterize the mirror behavior. The wavefront sensor measures the influence function (how each actuator affects the overall surface of the mirror) from each actuator at a range of commanded strokes. The repeatability of each actuation is assessed, and through periodic measurements over the duration of the mission, we can quantify any long-term drifting. The overall rms surface error of the mirror is also characterized.

5.1.2.2 Experiment 1: Wavefront Correction on Internal Source

Experiment 1 (Table 5-3 still uses the internal laser, but it tests the ability of the deformable mirror to correct for internal disturbances (from thermal gradients, misalignment, etc).

5.1.2.3 Experiment 2: Wavefront Correction on External Object

Experiment 2 (Table 5-4 uses an external source to demonstrate that the mirror and control system are able to perform closed loop correction on the aperture arm of the

Table 5-2: Experiment traceability for open-loop mirror characterization

Experiment	Description	Observables	Observable Performance	Success Criteria
Individual actuator pokes	Command each of 32 actuators in order to: - 33% stroke - 67% stroke - 100% stroke	- X-Y displacement (in pixels) of spot after actuation - Image of spots before and after actuation	- Maximum expected spot displacement: 1.5 μm stroke - Minimum detectable spot displacement correspondin g to 50 nm actuator motion	- Measured mirror deflection is within 100 nm rms of commanded deflection - Mirror meets success criteria for 95% of all tests
Individual actuator pulls	Command all 32 actuators to 100% deflection. Command each of 32 actuators in order to: - 67% stroke - 33% stroke - 0% stroke			
Zernike surface maps	Command actuators to the following Zernike modes at 50% and 100%: - Tip - Tilt - Defocus - Astigmatism			

payload. This is the most operationally relevant experiment, as it tests the mirror's performance on an external target. This is also the most complex experiment and requires a three-axis stabilized pointing system to maintain observation on a target star.

5.2 Design and Performance Analysis

5.2.1 Science Traceability

The high-level mission requirements for characterizing the mirror and performing closed-loop correction flow down to requirements on the wavefront sensor, focal plane telescope design, and requirements levied on subsystems (particularly pointing). Table 5-5 shows how each of the experiments flows down to detailed design decisions.

Table 5-3: Experiment traceability for closed loop wavefront correction with the internal source

Experiment	Description	Observables	Observable Performance	Success Criteria
Correct static imperfections in optical system (Source: internal laser)	- Image focal plane and wavefront sensor with mirror unactuated - Apply closed-loop correction with wavefront sensor in the loop - Image focal plane and wavefront sensor with optimal mirror deflection	- Strehl before and after correction - Optimal commanded mirror voltage array for each parameter - Focal plane image before and after correction	- Mirror actuations of $\lambda/100$ rms detectable on focal plane - Strehl or encircled energy improves with each iteration	- Resulting Strehl >85% - Converge to correction within 8 minutes (TBR based on access times) - Actuators stay within 10%-90% stroke range

5.2.2 DeMi Design Overview

Due to the need to accommodate a deformable mirror and reduce complexity, it is not practical to try to design the CubeSat as a reflecting telescope using mirrors. While it may be possible to integrate a larger standard lens in the aperture (current design is 100 mm), the corresponding longer focal length is not an option due to the limited space available for all components, and resizing the beam would be difficult. A smaller aperture and lens will limit the angular resolution ($1.22\ \lambda/D$) and sensitivity as well as increase the size of the PSF (which must also be Nyquist sampled by the pixels on the detector), but tight angular resolution is not a requirement for this technology demonstration. For a 1-inch (25.4 mm) or 0.5-inch lens (12.7 mm) diameter lens, which have minimum focal lengths on the order of their diameter, the angular resolution (width of the center of the point spread function) at 500 nm would be 1.2 arcseconds (1-inch) and 2.4 arcseconds (0.5-inch).

The optical layout shown in Figure 5-1 was designed to accommodate both an

Table 5-4: Experiment traceability for closed loop wavefront correction with an external source

Experiment	Description	Observables	Observable Performance	Success Criteria
Correct static imperfections in optical system (Source: external object)	- Image focal plane with mirror unactuated - Apply closed-loop correction with wavefront sensor in the loop - Image focal plane with optimal mirror deflection	- Focal plane image at beginning and end of observation - Strehl during observation	- Mirror actuations of $\lambda/100$ rms detectable on focal plane - Strehl or encircled energy improves with each iteration	- Resulting Strehl >80% - Converge to correction within 8 minutes (based on access times) - Actuators stay within 10%-90% stroke range

internal and external source as well as a wavefront sensor and focal plane detector within a 2U volume. The aperture is an inch in diameter, and all other optics are 1/2-inch diameter elements. Where possible, f-numbers larger than 2 are used to avoid distortion from edges of refractive optics. Light from either an internal laser diode or an external object (imaged through a 1-inch aperture) is routed to bounce off the Deformable Mirror, after which it is split to send some of the light to a wavefront sensor while the rest is focused to an image plane.

The detectors are Aptina 2.2 μm pixel black and white CMOS arrays. A lower-powered fiber coupled laser serves as the known monochromatic light source for mirror characterization. All of the optical elements are COTS components available from vendors such as Thorlabs, Newark, and Edmund Optics. The refractive optics will be made out of a radiation hard material for the flight version and may require some custom manufacturing.

Table 5-5: Science Traceability for high-level DeMi mission goals

Objectives	Measurement/ Experiment Required Capabilities	Instrument Performance Requirements		Projected performance (certainty)	Mission Requirements	Data Products
		Accuracy	Precision			
Verify mirror performance (a) Observe that mirror responds to known commands (b) Internal laser illumination (c) Long-term (>12 month) duration	Command the mirror to open-loop actuation			C drivers available for mirror 14 bit step resolution on controller Maximum ~200 V	Power: 200 V input, >5 W draw Volume: 95 x 130 x 1.8 mm Interface with BMC mini mirror driver	
	Measure displacement of individual mirror actuators (high-order)	50 nm	100 nm (TBR)		Implement a high-order wfs	Wavefront measurement sent to ground for post-processing
	Measure low-order Zernike modes Z(1,-1) - Z(2,2)	50 nm rms	100 nm rms		Implement a low-order wfs	Wavefront measurement sent to ground for post-processing
	Illuminate with internal laser	Laser power > 1pW and < 100 pW		Commercial lasers available that meet this requirement	Power: <1 W	
	Long-term mirror operation	Lifetime > 12 months		CubeSat missions historically have lasted longer	Orbit altitude Rated component lifetimes > 15 months Communications support over lifetime	
Wavefront Correction (a) Correct static aberrations in optical path (b) Correct dynamic aberrations	Correct static aberrations in optical path	Correct to <100 nm rms		6x6 mirror control authority: defocus, astigmatism, limited tip/tilt	Wavefront sensor precision 10 nm rms, accuracy 5 nm rms	Focal plane images sent to ground for post-processing
	Correct dynamic aberrations in optical path	Correct to <100 nm rms at 0.1 Hz		Mechanical response <20 us	Wavefront sensor calculation time <1 s	Focal plane images sent to ground for post-processing
	Closed-loop mirror control			Driver frame rate 8 kHz	Power: 200 V input Volume: 95 x 130 x 1.8 mm	Focal plane images sent to ground for post-processing
Observe a star (a) Achieve detectable signal from star (b) Keep star centered on detector	Observation wavelength	500 - 720 nm		COTS filters and detectors meet this requirement	Detector QE >60% over range System throughput >20% over range	Image sent to ground for post-processing
	SNR at detector	10		>10 with sources brighter than magnitude 3		
	Observation duration	5 – 8 minutes (Satellite slew rate of 0.3 deg/s with pointing accuracy <0.5 deg)		Existing reaction wheels and ADCS systems can meet this on CubeSats	Spacecraft must keep star on detector over entire observation duration	
	Exposure time	0.001 s (Spacecraft jitter over 1 kHz must be below TBD threshold)		COTS CMOS detector limit	Spacecraft jitter over 1 kHz must be less than detector plate scale	

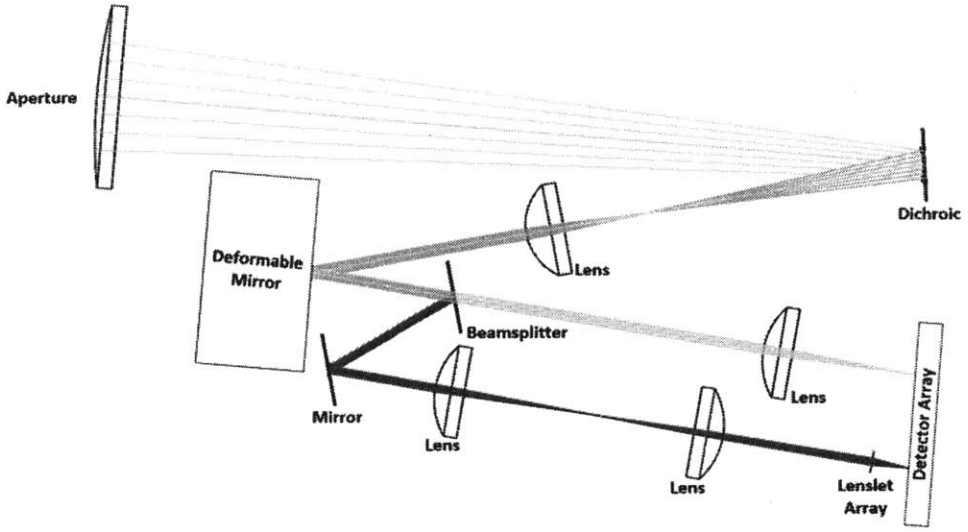

Figure 5-1: Optical layout of the 2U adaptive optics characterization payload. Blue: light path to the wavefront sensor (mirror characterization and closed loop demonstration). Green: light path to the focal plane sensor (closed loop demonstration).

5.2.3 Wavefront Sensor Design: Shack Hartmann

A wavefront sensor or surface metrology sensor is required to provide high spatial frequency information on the mirror surface. It has a secondary use as the source of wavefront error measurement in a closed-loop operation. There are several alternatives to wavefront sensing in adaptive optics systems: Shack-Hartmann, pyramid, and curvature sensors are commonly implemented on existing systems, while there are several methods such as Zernke phase dimples and sensorless reconstruction algorithms that are under development. There are also methods to obtain high accuracy measurements on surface metrology, such as the Phased Aperture Wavefront (PAW) or interferometry. For the DeMi payload, the Shack Hartmann sensor was selected because of its heritage and ease of application for both mirror and wavefront measurements. It also doesn't involve moving parts and is fairly robust to misalignments. Performance-wise there are several potential alternatives that would offer better measurements but would add risk and complexity to the system.

The requirements for the sensor itself are driven by the high level characterization

requirements as illustrated in Figure 5-2.

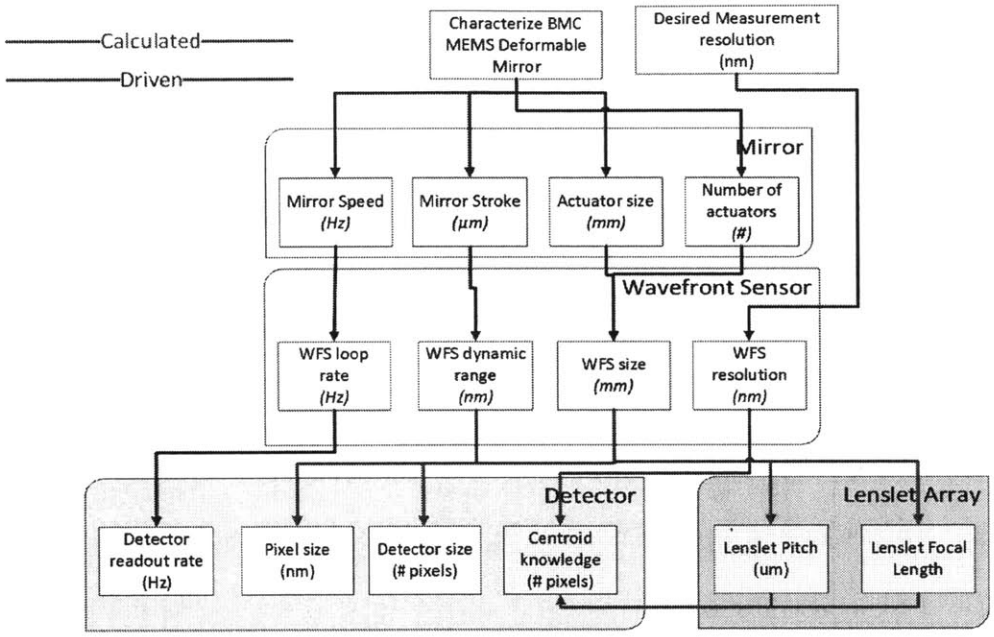

Figure 5-2: Requirements flow for the Shack Hartmann sensor design. Final design decision variables are lenslet size and focal length, and detector pixels.

To decide on a final Shack Hartmann design, the lenslet array and detector parameters were optimized for desired system performance. A list of COTS lenslet arrays and detector arrays was compiled and the elements that most closely matched the desired specifications were chosen for implementation.

The main design knobs on a Shack Hartmann sensor are the lenslet pitch and focal length. The lenslet pitch is driven by the desired maximum detectable wavefront error. The idea is to keep the spots within the designed grid to avoid crosstalk and confusion of spot movement on the detector.

The lenslet pitch is calculated by

$$L_p = 2 \times P_p \times F/\# \times \epsilon_{wf} \tag{5.1}$$

where P_p is the pixel pitch, $F/\#$ is the f-number of the optical system downstream of the mirror, and ϵ_{wf} is the desired detectable or expected wavefront error. For the mirror demonstration mission, the lenslet pitch is driven by the mirror stroke, 1.5

μm.

The lenslet focal length is calculated by

$$L_f = F/\# \times L_p/M \tag{5.2}$$

where M is the magnification of the system before the wavefront sensor.

The chosen lenslet array has a pitch of 150 μm and focal length 6.7 mm. With this lenslet array, the mirror actuators are oversampled, and each lenslet is capable of measuring wavefront errors up to 5 μm. The resolution of the spot motion is centroid-algorithm dependent, but subpixel resolution yields $\lambda/10$ measurement precision.

5.2.4 Science Image Design: Focal Plane Sensor

In order to demonstrate external correction, the focal plane sensor must be able to detect objects of interest. Figure 5-3 shows the requirements flow for the focal plane sensor. This drives the available source opportunities and serves as a point of information for determining requirements on the aperture and source beam for an intersatellite link.

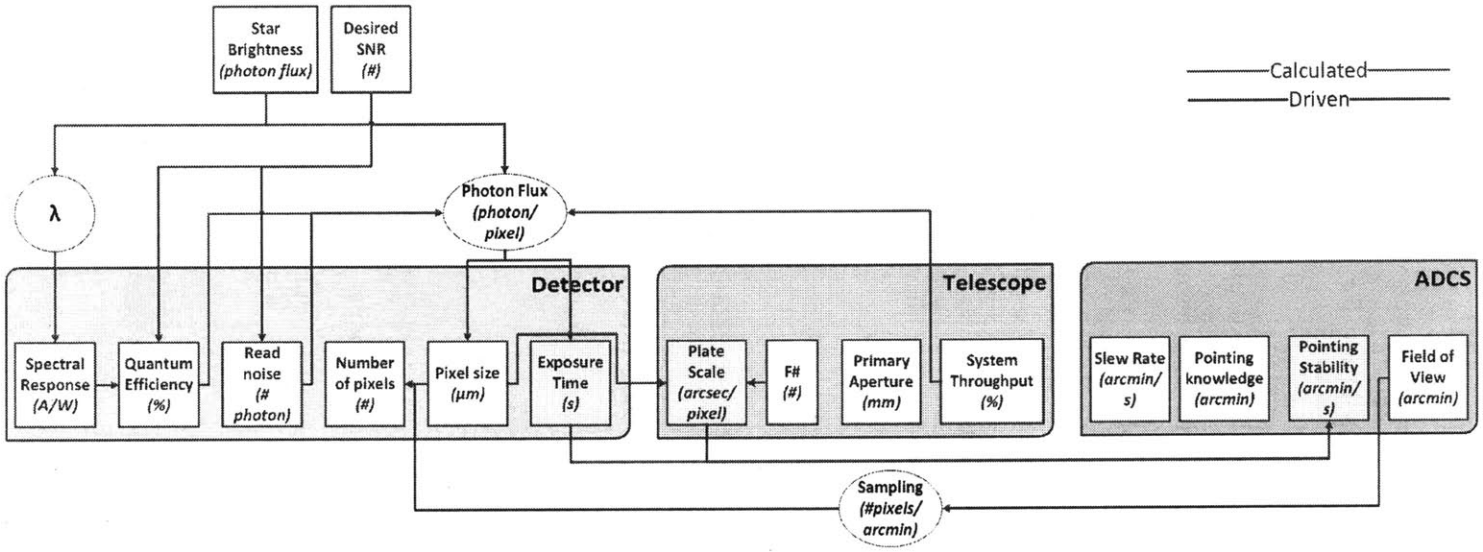

Figure 5-3: Requirements flow for external object observation and correction. The exposure time, platescale, and stability are the main driven design variables.

The final telescope design was driven by the desired signal to noise ratio on the detector. There is a trade-off between exposure time, spacecraft pointing requirements, and measurement opportunities. Each of these parameters was varied iteratively in order to determine the most effective and realistic solution for this demonstration mission.

The telescope exposure time versus star magnitude was calculated two ways. One was a 'Top-down'approach with a star magnitude driving the exposure time based on a desired signal to noise ratio. The second was a 'Bottom-up'approach with a detector-dependent exposure time and desired signal to noise ratio driving the minimum detectable star brightness. A similar analysis can be applied to a transmitter on an intersatellite link, but for this mission we focus on stars.

The exposure time, telescope parameters, and detector drive the pointing and jitter requirements.

5.3 DeMi Satellite System Requirements

The payload design and observation requirements impose requirements on other CubeSat subsystems. Table 5-6 gives a summary of the key parameters and spacecraft requirements associated with each of these experiments.

The power requirements are driven by the mirror driver and laser system. There are several options for mirror driver. One option has a 14-bit driver but runs upwards of 40 W, which cannot be easily accommodated on a CubeSat from both a power generation and thermal management standpoint. The other option is slightly lower resolution (10-bit) and is cited at 5 W.

Depending on the instrument architecture, there is the potential to generate several Mbps worth of data on this payload. By duty-cycling the experiment, and because there are not continuous measurement opportunities, these can be accommodated with current CubeSat technology. There are modifications in operations that can be made to accommodate lower data rates. CubeSat radio systems are limited in their bandwidth downlink capability. The current most capable systems reach levels of up

Table 5-6: Requirements on the spacecraft from the two experiment configurations on DeMi

Parameter	Open Loop	Closed Loop	Notes
Mass	< 500 g		Estimated based on COTS mounts
Volume	10 cm × 10 cm × 20 cm		Currently constrained to 2U
Power	< 6.5 W	< 6.2 W	Based on estimates of controller power draw. Internal laser required for mirror characterization.
Attitude Control	N/A	Pointing: 0.1 degree, Jitter: <20as over 1 ms	Mirror characterization all done internally.
Total Data	15 kb	2.6 Mb	Minimum required per experiment for experiment success

to 3 Mbps, but amateur band radios are limited to several hundreds of kbps downlink.

5.3.1 DeMi Pointing and Jitter Requirements

Image correction requires that a star or extended object (Earth, moon, etc.) stay within the field of view of the external aperture for at least 5 consecutive minutes. Based on our preliminary models using STK looking at five bright stars (Alpha Centauri, Arcturis, Canopus, Sirius, and Vega), a satellite in the same orbit as the International Space Station (400 x 425 km and 51.6 degree inclination) would expect to see the same bright star every orbit for an average of three to five minutes for a 1.0 deg × 0.8 deg sensor limited to a 0.5 deg/s slew rate. During this time, a closed-loop algorithm will run to improve the image quality of that external object within the control authority of the mirror.

The jitter requirements are driven by the exposure time and the pixel field of view of the focal plane sensor. The minimum exposure time (software-limited) for the chosen Aptina detector is 1 ms, and the pixel field of view is 20 as. So all high frequency jitter (above 1000 Hz) must be below a total 20 as threshhold in order to prevent blurring. While there has been some work in characterizing CubeSat reaction wheel jitter performance [59], this is an area that will need to be assessed in more detail for the flight program.

We plan to investigate, for a follow-on nanosatellite mission whose goal is to image specific stars, or for a technology demonstration implementation on a 6U platform, whether or not a fast steering (tip-tilt) mirror will be needed. It is generally accepted that a fast steering mirror will be needed on a larger space telescope. The fast steering mirror would allow for much more accurate pointing than a reaction wheel assembly can provide, and would also correct for tip and tilt errors in the wavefront that may be larger than the stroke of the deformable mirrors can correct for.

5.3.2 Other Considerations

There are aspects of the system design and satellite operation that are left for future work. Specific electronic and software interfaces between the bus and payload (on-board processing, command protocol, drivers) have not been defined, nor has the flight optomechanical design.

Specific satellite operation considerations that are orbit-dependent also remain to be determined. There is no shutter on DeMi, so it is possible that the spacecraft will need operational modes that avoid looking at the sun.

5.4 Summary of Contributions

In this chapter we presented the mission architecture and design for a CubeSat-compatible adaptive optics payload. We develop an experiment architecture for mirror characterization and closed-loop demonstration, and we provide rationale for an

optical design that meets the performance requirements. We also presented the system design and operational considerations.

The following chapter describes the in-laboratory validation of this nanosatellite technology demonstration mission. Flying and characterizing a MEMS DM on a space platform will contribute to future missions with enhanced imaging and scientific capabilities.

Chapter 6

Laboratory Validation of CubeSat Adaptive Optics Payload for Atmospheric Characterization

The goal of the laboratory hardware validation is to demonstrate that the system as designed will provide the expected performance in terms of both mirror characterization and providing closed-loop correction that provides substantial improvements to imaging systems on a nanosatellite scale.

The metrics described in Chapter 5 for mirror characterization are quantified for the CubeSat adaptive optics payload through laboratory tests. Measuring mirror performance is critical for understanding how the behavior of the mirror changes over time spent in on-orbit operation. The metrics we use to characterize the mirror are based on in-laboratory or ground characterization of deformable mirrors [43]. We use procedures and lessons learned from existing ground systems to inform the functionality and autonomous operation modes needed for our on-orbit experiments. The metrics of interest for the mirror are the stroke variability between actuators and the actuator influence function (how each actuator affects the behavior of the surrounding membrane).

We are interested in how well the nanosatellite payload design can make the measurements of interest on the mirror. The laboratory validation is meant to assess

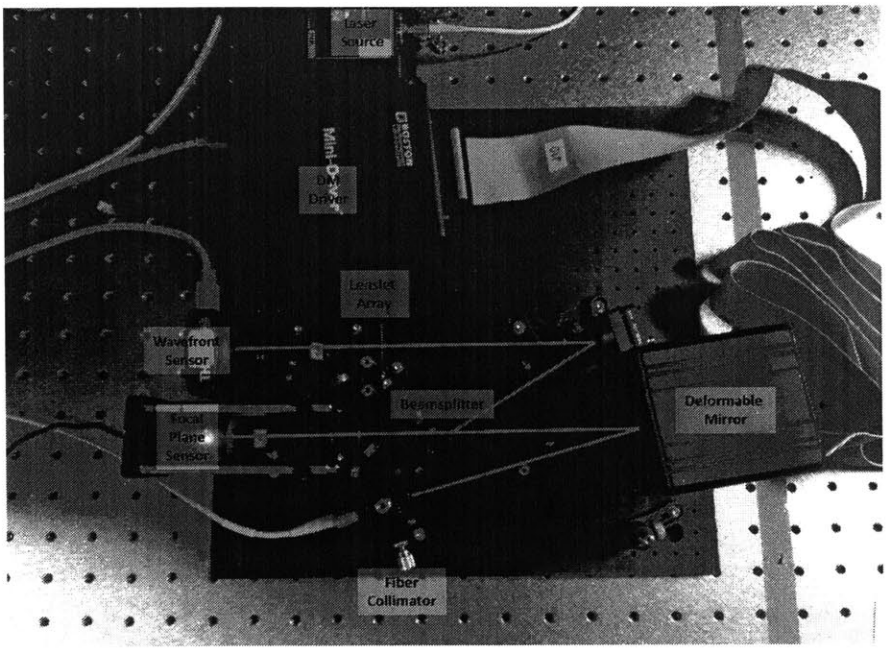

Figure 6-1: Laboratory Hardware Setup of CubeSat-Scale Wavefront Sensor

the repeatability and accuracy of the wavefront sensing measurements

6.1 Hardware Setup

The hardware setup is shown in Figure 6-1. The layout is based on the design presented in Chapter 5, with some modifications including re-imaging of the lenslet spots due to plastic packaging around the mirror and detector. There is also not an external science source in this setup; instead all measurements are taken with a fiber-coupled 635 nm laser.

The fiber-coupled laser is attached to a collimator and iris that can be re-sized to match the diameter of the mirror. A beamsplitter splits the beam into the science and wavefront sensing arms of the payload. The science arm is focused onto a detector. The wavefront sensor is set up such that the mirror is conjugate to the lenslet array, and there is a factor of 2 magnification between the mirror and lenslet array to allow more lenslet sampling per actuator. The focal plane of the lenslet array is re-imaged onto a Thorlabs CMOS detector, and this spot field is read in for each iteration of

the control algorithm.

All optomechanical components were procured from Thorlabs. The mirror is a Boston Micromachines continuous facesheet mini deformable mirror (32 actuators, 300 μm actuator pitch, 1.5 μm stroke. The Shack Hartmann detector is an off-the-shelf Thorlabs camera that includes an Aptina detector (monochrome CMOS, 5.2 μm pixels). The focal plane detector is from a Microsoft WebCam device (front optics removed).

6.2 Software Setup

The control software and drivers for the mirror and wavefront sensor camera are written in MATLAB. The approach to the open and closed loop software architecture is shown in Figure 6-2. There are several modules that encapsulate software functionalities –open-loop mirror characterization, closed-loop initialization, and closed-loop control –as depicted in the diagram.

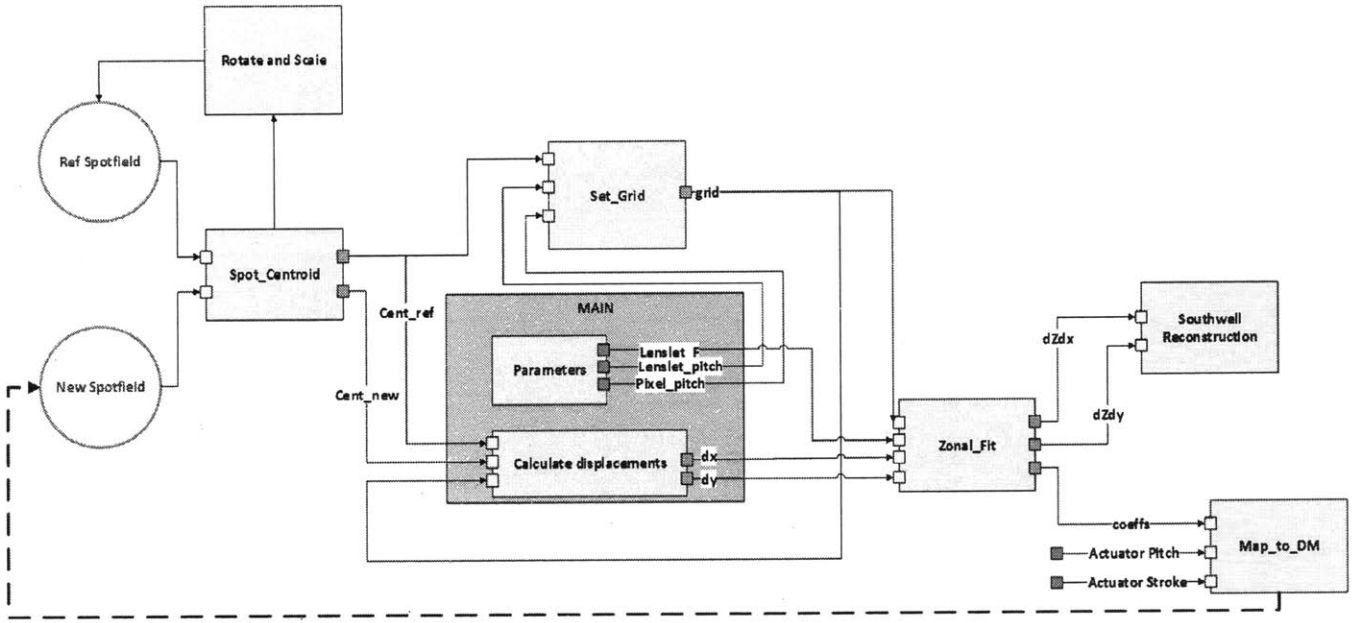

Figure 6-2: Diagram of internal control structure (depicts both open and closed-loop paths)

6.3 Open-Loop Wavefront Reconstruction

Open-loop wavefront reconstruction is a software mode that enables mirror measurement based on spotfield deltas. There is no wavefront correction associated with this operation.

6.3.1 Reconstruction Algorithm

For the open-loop characterization, the reference spotfield is measured from an unactuated mirror. To characterize the shape of the mirror with different actuator and surface commands, we look at the deltas between the actuated and unactuated mirror.

The wavefront reconstruction algorithm is based on upgrades to the Southwell algorithm [142] as shown in Figure 6-3. There are other versions of zonal wavefront reconstruction that offer improvements to the Southwell algorithm [143], [144], [145], [146] but they have not yet been implemented in this work. There are also modal (Zernike [147], [148], Fourier, etc) wavefront reconstruction methods that have been proven effective in adaptive optics systems. Those are also not implemented here, though they are under consideration for future work.

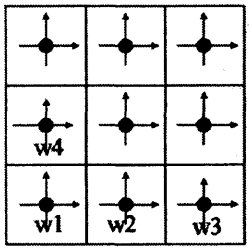

$$\frac{s_1^x + s_2^x}{2} = w_2 - w_1$$

$$\frac{s_1^y + s_4^y}{2} = w_4 - w_1$$

Figure 6-3: Pictoral Representation of the Southwell Reconstruction Algorithm [142]

Open-loop wavefront (mirror) measurements were taken by collecting and averaging 10 frames of spotfield measurements for mirror actuation. Each actuator was poked to 100% of its stroke, pulled to 100%, and tip, tilt, and defocus shapes were commanded on the mirror. These spotfield measurements were compared to those taken from an unactuated mirror to determine the stroke and influence functions of each actuator. The mirror specifications list an individual actuator stroke of 1.5 μm

[95].

6.3.2 Truth measurements with Zygo Interferometer

To validate the wavefront measurement, we use truth data from a Zygo interferometer. A Zygo interferometer is a commercial insrument used to obtain high-precision metrology of an optical surface [149]. The version of the instrument used to measure the BMC deformable mirror is a Fizeau interferometer with wavefront measurement repeatability better than 0.35 nm rms [150].

The Boston Micromachines Mini Deformable Mirror was placed in front of the Zygo interferometer as shown in Figure 6-4. Due to zoom limitations and the small size of the mirror (1.5 mm) compared to the Zygo aperture (10 cm), we could not obtain reliable Zygo measurements for actuator strokes larger than 20%. Figure 6-5 shows the output from the Zygo interferometer using the MetroPro software [151]. To obtain surface measurements for the mirror, each actuator was poked and pulled, and the entire mirror was commanded to tip and tilt and defocus. The phase and intensity information was saved for each of the measurements and processed in MATLAB to determine the overall stroke and influence function for each actuator.

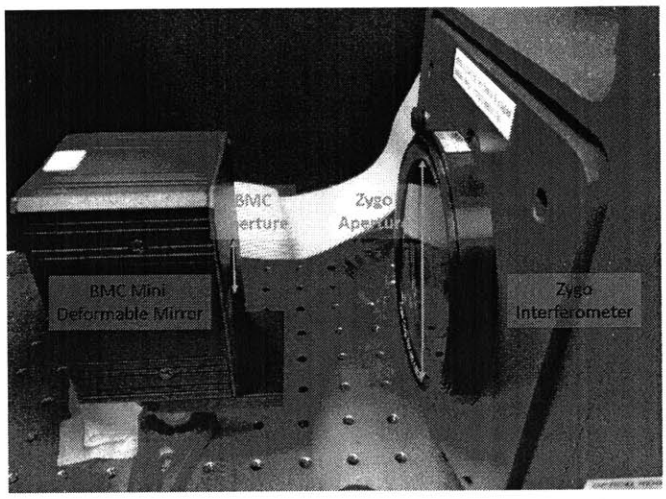

Figure 6-4: Hardware Setup for BMC Mini DM measurements

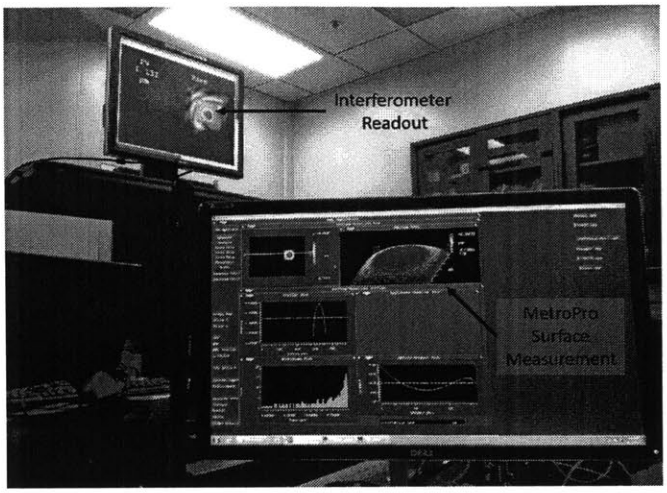

Figure 6-5: MetroPro software output for BMC Mini DM measurements

6.3.3 Results

The overall effectiveness of the open-loop wavefront reconstructor is evaluated based on measurement repeatability and accuracy. The measurement repeatability is calculated from a series of 10 measurements for each commanded mirror deformation. The measurement accuracy is determined by comparing the results of the CubeSat wavefront sensor reconstruction to the measurements obtained from the Zygo interferometer. It is characterized by error in overall stroke measurement as well as variation in influence function for each actuator. Figure 6-6 shows the results from both of these approaches. The figure shows surface maps (color scale on the right in μm) of the entire mirror for each individual actuator poke. The location of the surface maps on the grid corresponds to the location of the actuator on the mirror.

Figures 6-7 and 6-8 show cut views if the influence functions from perpendicular directions on the mirror the measured influence functions for each of the 32 actuators poked at 20 percent of their maximum stroke. The actuators are offset to illustrate the shapes of the influence functions. There is clear variation over the magnitude of each actuator's influence function, and this is partly due to noise in the measurements. While there is general agreement in the shapes of the actuator influence functions, there is a scaling discrepancy between the results for the Shack Hartmann sensor versus the Zygo measurements. This could be due to nuances in the reconstruction

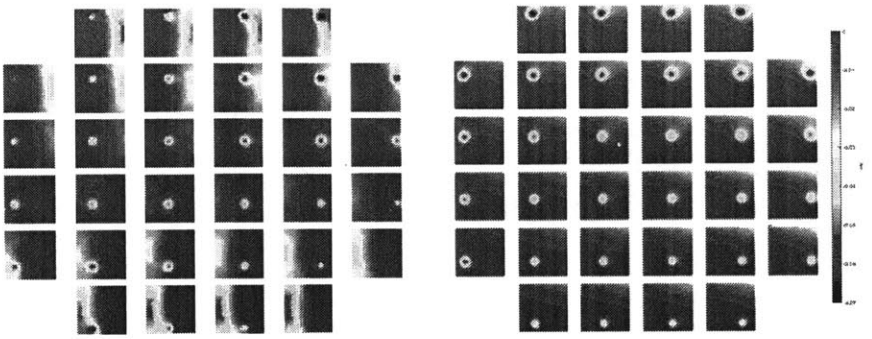

Figure 6-6: Side by side comparison of the Zygo interferometer surface measurement and the Shack Hartmann wavefront sensor for each Boston Micromachines Mini actuator poke. Each grid figure represents the entire surface of the mirror with one actuator poked, and the grid is laid out to reflect the position of each actuator

algorithm and will be investigated further.

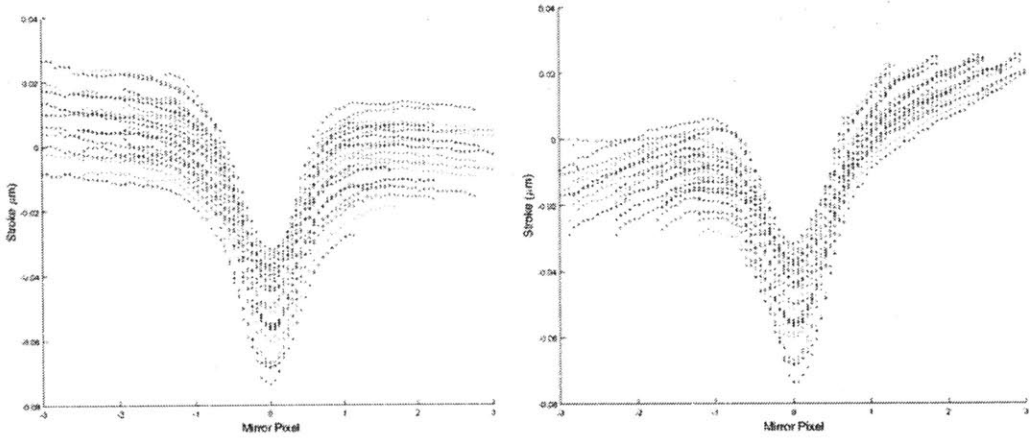

Figure 6-7: Influence functions of the BMC actuators as measured with a Zygo interferometer. Top: horizontal, Bottom: vertical. Each actuator is represented by a different colored dashed line. Each actuator exhibits a Gaussian-type influence function, but there is variability in the measured performance of each actuator

6.3.4 Limitations and Future Modifications

The measurements obtained from the nanosatellite-scale wavefront sensor are encouraging in terms of capability (mirror movement at less than 100 nm is detectable by the sensor), but there is some discrepancy in the results from the Zygo interferometer. Peformance from the test platform may be enhanced by the use of a more controlled

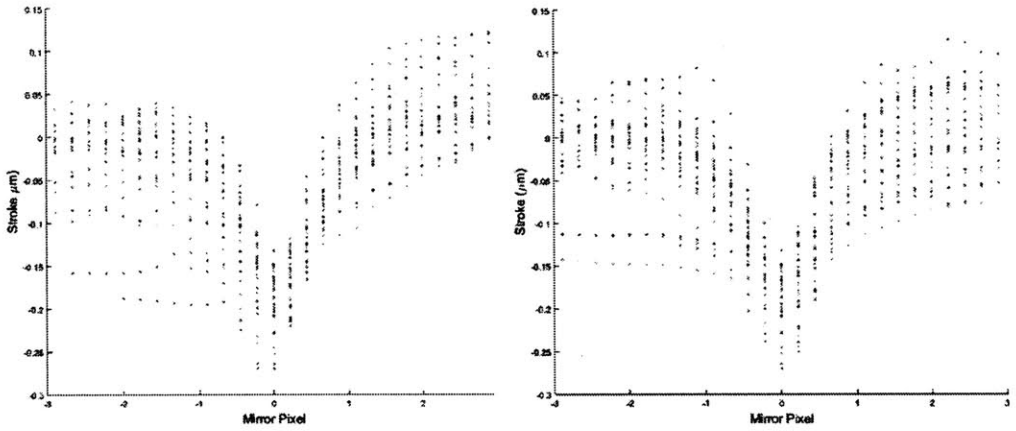

Figure 6-8: Influence functions of the BMC actuators as measured with a Zygo interferometer. Top: horizontal, Bottom: vertical. Each actuator is represented by a different colored dashed line. Each actuator exhibits a Gaussian-type influence function, but there is variability in the measured performance of each actuator

environment. The laboratory setup is on a floating optical table surrounded by optically thick curtains, but an enclosed testing area would be useful.

There are other options for the wavefront reconstruction algorithm that are worth exploring in future development of the nanosatellite payload [143]. Other options for reducing the noise and improving the resolution of the system are looking into better spot centroiding algorithms (a weighted centroiding method is currently used as the spots are over sampled on the detector) or implementing a mask or weighting function in software to mitigate the effects of noisy (nominally unmoving) spots on the wavefront reconstruction.

The Shack-Hartmann sensor design was chosen for its widespread use and relative ease in implementation as well as its usefulness in both mirror characterization and closed loop implementation. A Shack-Hartmann sensor has limitations, however. For example, it is not capable of measuring high spatial frequency surface figures that come from the mirror printthrough. For better mirror characterization it would be useful to look into other options such as interferometers or metrology sensors.

6.4 Closed-Loop Wavefront Control

The second goal of the laboratory hardware characterization is to evaluate the effectiveness of closed-loop correction. There are two overarching steps to implementing the closed-loop control algorithm. The first is the characterization of the closed loop system in order to quantify the mirror/wavefront sensor interaction and calibrate out any system-level errors (e.g. lenslet rotation). The second is running the control algorithm with mirror commands.

The overall performance of the closed-loop wavefront control system will dictate how effective this system would be for measuring and correcting both thermomechanical distortions and atmospheric distortions. The metrics used to determine this (and the results for this system) are described in Section 6.4.3.

6.4.1 System Characterization

6.4.1.1 Theoretical Reference Grid

From the fundamental design of the Shack-Hartmann sensor, a perfectly flat wavefront will manifest itself on the detector as an array of uniformly-spaced focused spots. The distance between spots in pixel-space is drive by the size of the lenslet array, the size of the pixels, and any magnification between the lenslet array and detector.

For this system, the lenslet pitch is 150 μm and the detector pixel pitch is 5.2 μm. There are seventeen lenslet actuators across the pupil.

The control algorithm uses measured offsets from the center of each grid to calculate wavefront error and corresponding corrective mirror commands.

6.4.1.2 Calibration and Registration

Before running the closed-loop algorithm, several system parameters need to be measured and understood.

Wavefront measurement and control in closed-loop is performed in actuator space. In order to represent measured wavefront error in terms of actuator commands, we calculate an interaction matrix - a matrix that quantifies x and y spot movements for

each individual actuator poke. This matrix is calculated once and used to reconstruct the wavefront in mirror actuator space within the closed-loop control algorithm.

System misalignments (scale and z-rotation) are caused by imperfect mounting or alignment and can also be calibrated out of the wavefront measurement. A spotfield is measured with an unactuated mirror. Using a least-squares approach, a rotation matrix and a scaling factor are fit between the theoretical grid and the measured spot centroids. The calculated scale and rotation are reversed on all subsequent readouts.

Finally, the brightness of each aperture is measured in order to normalize the effects from variable throughput on the reconstructor matrix (see the following subsection for details.)

6.4.2 Closed-Loop Correction Algorithm

6.4.2.1 Wavefront Error Measurement

The wavefront error measurement is calculated by reading in a spot field, mapping each spot to a grid location as defined in Section 7.4.1.1, and calculating the x and y displacement from the centroid of that grid box. An example quiver plot based on the x and y spot location for a defocused system is shown in Figure 6-9. The resolution of the spot movement depends on how accurately the centroiding algorithm can determine the movement of the centroid.

The next step in the control algorithm is to convert the measurement of spot movement on the wavefront sensor to a wavefront shape as described in actuator space.

6.4.2.2 Wavefront Error Reconstruction and Control

A leaky integrator is implemented for this system as in Equation 6.1

$$u_i = (1 - k_l)u_{i-1} + k_0 Rc \tag{6.1}$$

where u_i is the subsequent commanded mirror shape, u_{i-1} is the previous commanded mirror shape, and c is the vector of spot deflections in dx and dy observed

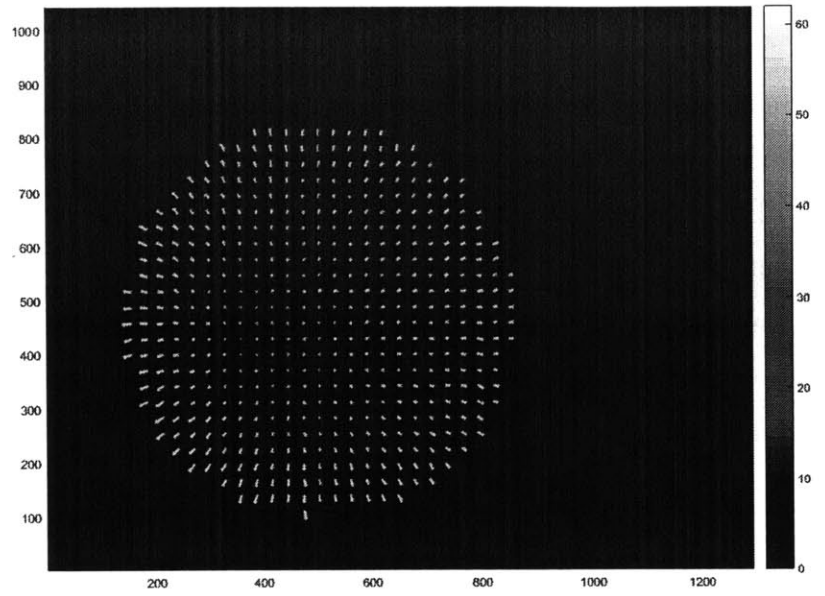

Figure 6-9: Quiver plot showing measured spot deviations from a theoretical flat wavefront. The overall spot deflections are typical of a defocused beam.

on the wavefront sensor. For the gain constants, k_l is set to 0.02 and k_0 is given an initial value of 0.3. Both of these values are tunable. The advantages of using this type of controller is that any unmeasurable wavefront modes (piston and 'waffle') will be slowly driven out of the system.

The matrix R is a Reconstructor matrix, and it is a function of the interaction matrix A, a diagonal matrix of normalized subaperture brightness W, and a covariance matrix C based on expected distortions calculated from a Komolgorov atmospheric model. For the initial controller implementation, the subaperture brightness and covariance matrix were not included, as those are more relevant for imaging through the atmosphere as compared to the relatively benign environment of the optical laboratory.

$$R = (A^T W A + \alpha(\frac{\lambda_{wfs}}{4\pi})^2 C^{-1})^{-1} A^T W \tag{6.2}$$

The phase covariance matrix is scaled by the observing wavelength λ_{wfs} and the parameter α as defined in Equation 6.3.

$$\alpha = \frac{\sigma^2}{3.44(\frac{d}{r_0})^{5/3}} \tag{6.3}$$

6.4.2.3 Commanding the Mirror

This deformable mirror is an electrostatic device with 1.5 μm stroke. The electrostatic actuation allows the actuators to only move in one direction. Thus, after the wavefront is measured, we design the system such that the desired mirror actuations are offset (i.e. we effectively treat 50% stroke as the zero point of mirror actuation) and clipped to fall within the control authority of the mirror.

We accomplish this by first offsetting the actuations such that the center of the measured wavefront is at the 50 percent stroke level of the mirror. Then the mirror command is scaled such that the maximum deflection is 90 percent of the mirror stroke. This limits the correction ability of the mirror slightly but prevents actuator saturation.

Mirror commands are given as an array of input voltages. There is a nonlinear relationship between the applied voltage and the resulting actuator movement as shown in Figure 6-10. The interaction matrix is generated from 100% mirror actuation measurements, so the single-actuator curve is used to convert the desired mirror deflection in percent of overall actuator stroke to the appropriate corresponding voltage command.

Figure 6-11 shows the readout of the control algorithm. The measured spot displacements are used to reconstruct the wavefront distortions in actuator space, and the resulting mirror commands are scaled by the voltage-displacement curve.

6.4.3 Results

The metrics with which the on-orbit payload experiment will determine how well the closed-loop algorithm worked are time to correction and percent Strehl improvement. Control bandwidth is also important if the intended application is atmospheric characterization, as the on-orbit wavefront measurement and control must keep up with

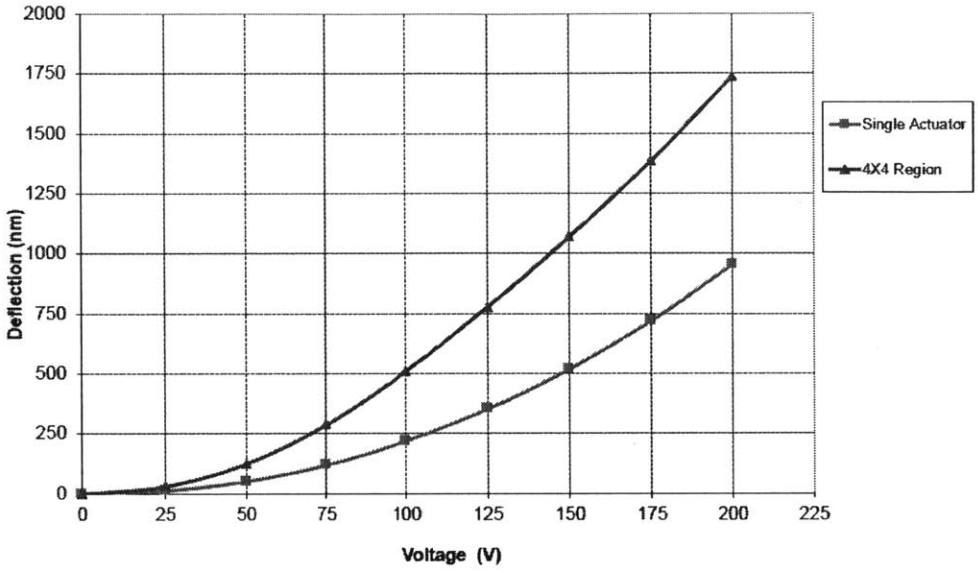

Figure 6-10: Deflection Curve (Voltage vs Stroke) for the BMC mini mirror [95]

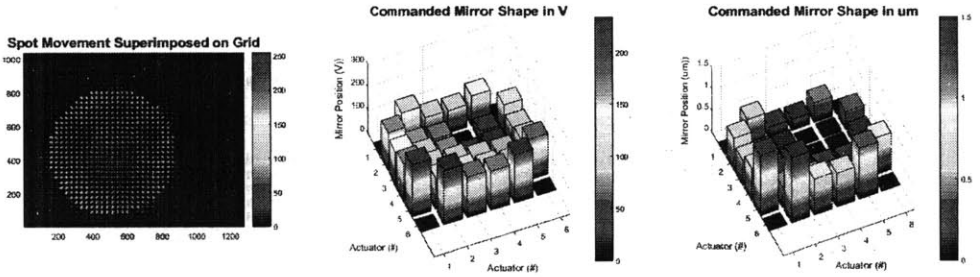

Figure 6-11: Closed Loop Mirror Performance - First Measurement **Note: will be updated**

atmospheric distortions that can change over a period of milliseconds (see Chapter 4). For thermomechanical misalignments, the required correction timescale is much longer, so bandwidths of a Hz or longer are acceptable.

The laboratory validation procedure was not optimized for bandwidth, and the purpose of the experiment is to demonstrate a working closed-loop controller that can apply reasonable correction within the operational limits of the mirror (only six actuators across). Strehl ratio is the focal plane measurement metric in the on-orbit experiment architecture. In the laboratory, the focal plane detector was a web camera with limited exposure control, and even with ND filters in place the sensor was saturated. We instead used encircled energy as the metric for the correction,

using a radius of about two times the Airy radius on the detector.

Figure 6-12 shows an example of the wavefront correction exhibited by the laboratory system, and Figure 6-13 shows how the mirror correction performed (in terms of Encircled Energy) over time. A piece of plastic was used to induce aberrations. The mirror was able to perform modest correction, but higher-order aberrations prevented the system from reaching pre-distortion encircled energy levels.

Figure 6-12: Closed loop mirror correction (left) before turning on the mirror (middle) after introducing aberrations (clear plastic sheeting) and (right) after 5 iterations of the algorithm.

6.5 Limitations and Flight Implementation

As currently set up, the hardware validation experiment only includes a monochromatic coherent laser source. In actual operation, the system must work with an external aperture illuminated by a faint point source or extended object source.

The control loop is also not optimized for fast performance. For speckle nulling and long time-scale corrections (thermo-mechanical distortions) the current performance is acceptable. For correcting distortions due to atmospheric variations, the control algorithm bandwidth must be better than 1 kHz. For static measurements and mirror characterization, the current design is sufficient.

There are several mechanical, electro-optical, and software changes that must be made between this laboratory hardware verification and the flight version of the payload. As selected, the DeMi mission chosen to fly is a 6U CubeSat, so the payload

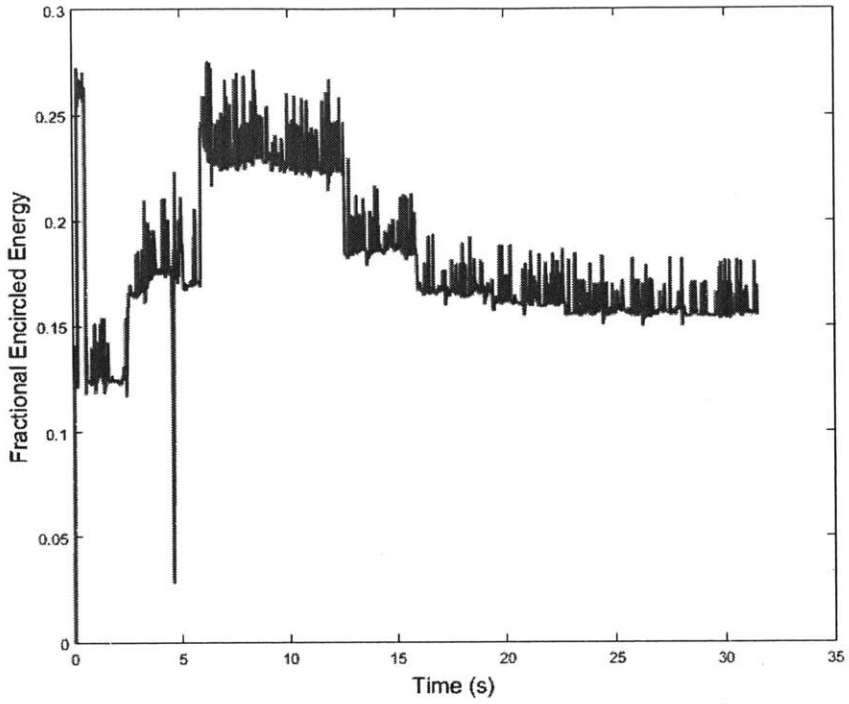

Figure 6-13: Plot of the encircled energy over the control time. The control bandwidth is approximately 0.2 Hz.

can be expanded to fill a 3U volume. This would enable a larger aperture and a deformable mirror with more actuators to be flown, which would enhance the overall science and technology demonstrated with this mission. More actuators enable the correction of higher-order modes and better off-axis wavefront correction, while a larger aperture allows dimmer sources to be detected, which relaxes some of the operational constraints.

Chapter 7

Conclusions and Future Work

With recent research and advances in small-scale sensors and subsystem capabilities, nanosatellites are viable platforms for Earth science missions. Nanosatellites offer close to state of the art measurement performance with better spatial and temporal resolution as compared with large monolithic systems.

This thesis addresses challenges of atmospheric sensing on nanosatellites and presents solutions and applications for improving measurements. The focus of this work is on microwave radiometers and occultation-based measurements for Earth atmospheric characterization and Exoplanet Direct Imaging for exoplanet atmospheric characterization.

7.1 Research Contributions

The research questions and contributions presented in this thesis are:

- How can we improve the accuracy of atmospheric sounding with microwave radiometers on CubeSats?
  - Analyzed coverage, revisit and performance metrics for constellations of nanosatellites hosting microwave radiometers and GPS radio occultation receivers, and identified that high-inclination orbits are optimal for global occultation measurements. Hundreds of global GPSRO opportunities per

day are possible, and six satellites per orbital plane yield revisit rates under one hour.

- Developed a model to predict the number of overlapping measurements that will occur between a microwave radiometer and GPS radio occultation sounder and showed that they meet (and exceed) the calibration requirement of one opportunity per day.
- Developed a method for assessing nanosatellite instrument GPSRO temperature errors to confirm they are below the level needed for radiometer calibration and demonstrated that commercial GPSRO receivers should be able to provide profiles with errors sufficient for calibrating a radiometer. The design requirements are 0.5-1.5 K GPSRO temperature precision to enable calibration of a microwave radiometer to 0.25 K absolute accuracy, and we show a 95% confidence of 0.1-1.7 K precision due to thermal noise for a commercial receiver.

- Can CubeSats demonstrate new wavefront control technologies for atmospheric characterization?
  - Analyzed coverage, revisit, and performance metrics for intersatellite links between two nanosatellites, and identified that dual-satellite systems comprised of one satellite in a polar orbit and one satellite in a mid-inclination orbit yield the most globally-distributed measurements.
  - Characterized atmospheric turbulence for a crosslink laser occultation measurement architecture and identified an application for wavefront control technology on space platforms to enhance atmospheric characterization of Earth using laser occultation.
  - Designed a nanosatellite wavefront control payload and developed mission architecture to demonstrate and characterize MEMS deformable mirror technology in the space environment.
  - Built and prototyped a laboratory experiment of the payload and demon-

strated nominal performance (open-loop mirror characterization to better than 100 nm precision and static closed-loop error correction).

The impact on the state of the art is explained in Table 7-1.

7.2 Future Work

7.2.1 Nanosatellite Atmospheric Sounding

The characterization of overlapping measurements between the radiometer and GPSRO instrumentation can be more nuanced. Modeling can be done to include radiometer sensitivity and account for detailed weightings for atmospheric contributions that correspond to weighting functions for both radiometer and GPSRO. Atmospheric bending is currently not taken into account in the GPSRO model. Other geometric considerations for the overlap measurements include an error assessment and sensitivity analysis for orbit altitude, pitch-up angle, and radiometer orientation.

The main future work and model adjustments for the GPSRO temperature retrieval simulation require flight-like data and processing algorithms. Receiver phase noise measurements came from specification sheets. From the tests that have been run to date, receiver performance seems to be within specifications. We would want to look for environmental sensitivities or contamination from other hardware/components on the spacecraft and re-run analyses with measured noise parameters. The GPS Radio Occultation performance analysis work was done using straightforward profile retrieval algorithm and can be compared with the software intended for flight demonstration. This also includes averaging and smoothing processes. Additionally, environment-dependent noise sources should be added to the thermal noise in the simulation to assess how much the measurement precision can be degraded.

There are several steps that can be taken to improve the overall performance of a nanosatellite GPSRO system. Elements such as propulsion, advanced deployed antenna arrays, or open-loop processing algorithms are all areas of research that could contribute to better measurements deeper into the atmosphere.

Table 7-1: Thesis Contributions

Topic	Current State of the Art	Thesis-Enabled State of the Art	Rationale
Passive Microwave Radiometry Calibration	0.75 K, 1–1.5 K on nanosatellite platforms	0.25 K on nanosatellites (pending launch validation)	Based on my predicted precision of collocated CubeSat GPS radio occultation measurements
Atmospheric Occultation —Radio	Neutral atmosphere GPSRO not demonstrated on CubeSats	0.1–1.7 K precision in neutral atmosphere from CubeSat GPSRO platform (pending launch validation)	Simulated results from COTS receiver with custom antenna
Atmospheric Occultation —Optical	Intersatellite occultation in lower troposphere (<5 km) dominated by scintillation and distortion	Sounding in lower troposphere improved with adaptive optics (mid-actuator count deformable mirrors can compensate for turbulence lower than 5 km)	Crosslink atmospheric turbulence modeling compared with control authority of MEMS deformable mirrors
MEMS Deformable Mirror Technology Readiness Level	Tests performed to date: vacuum, vibration, sounding rocket operation (NASA TRL 5-6)	Long-term on-orbit demonstration (NASA TRL 7 after successful flight)	Design and laboratory validation of mirror characterization payload

7.2.2 Nanosatellite Atmospheric Characterization

The atmospheric turbulence modeling work presented in Chapter 4 can be extended to incorporate a more detailed and orbit-dependent model of a crosslink turbulence signal. We looked at turbulence strength as a function of tangential height, but there are several other parameters that will affect the turbulence profile.

Similarly to the GPSRO modeling, future studies can consider pointing and orbit position error in overall signal noise assessment. A full adaptive optics error budget (wrapping in the wavefront sensor, control bandwidth, external factors) would benefit the study of crosslinks for laser occultation and more clearly answer the question of the usefulness of adaptive optics on such an instrument.

7.2.3 Nanosatellite Adaptive Optics Technology Demonstration

The preliminary laboratory validation of the payload showed that the design met performance requirements for a 3U CubeSat design. With the selection of a 6U flight mission, the mirror characterization payload design should be revisited. A different configuration or volume constraint could expand the tradespace of sensors, reconstruction algorithms, control algorithms, and aperture sizes that would enhance the mission outcome. Development of a detailed electrical and optomechanical design for the flight system should also be included in future efforts. Additive printing is a potential low-cost, fast turnaround option for mounting optical components.

Appendix A

MATLAB Code

A.1 GPS Radio Occultation

A.1.1 Access Calculations

```
%%%%%%%%%%%%%%%%%%%%%%
% File: Global_LO
% Created by: Annie Marinan
% Last modified: 04/06/2016
% Description: This script computes stuff

format long;
clear all
% close all
% count = 1;
set(0,'DefaultFigureWindowStyle','docked')

load('topo.mat','topo','topomap1');

topo2 = [topo(:,181:360) topo(:,1:180)]; % #ok<NODEF>

% Define surface settings
props.FaceColor= 'texture';
```

```
props.EdgeColor = 'none';
props.FaceLighting = 'phong';
props.Cdata = topo2;
[xx,yy,zz] = earth_sphere;

startdate = datenum(2016, 1, 1, 17, 00, 00);
enddate = datenum(2016, 2, 01, 17, 00, 00);
timespan = enddate-startdate;

%% Directory manipulation

% Navigate to directory with all output csv files (note: date column ...
   must
% be a numeric value to read in properly)
cd('C:\Users\Annie-MIT\Documents\STK 10\LaserCommAnimation\LO_Accesses')

out = dir;

numfiles = 1;%length(dir)-2;

% Determine the largest file dimensions from list and make dummy ...
   variable
% of that size

% for foo = 3:length(dir)
%     sizedata = size(csvread(out(foo).name,1,0));
%     if sizedata(1) > maxdata1;
%         maxdata1 = sizedata(1);
%     end
%     if sizedata(2) > maxdata2;
%         maxdata2 = sizedata(2);
%     end
% end
% numfiles = 5; %For test purposes, don't do all the files, please...
dataL1 = cell(numfiles,1);%/2);
filtereddataL1 = dataL1;
```

```
% Fill dummy variable tensor with all data files

for foo = 3:numfiles+2
    clear a;
    filename = '500_60-600_SS.csv';%out(foo).name;
    fid = fopen(filename);
    a = csvread(filename,1,0);
    a(:,1) = a(:,1) + 693960; %Offset to acount for Excel starting ...
        from year 1900 and Matlab starting from year 0
    % To look at data across different timeframes, set start and ...
        stop times
    % and only keep data between those
    a(a(:,1) < startdate,:) = [];
    a(a(:,1) > enddate,:) = [];
%     a(a(:,19) > 250,:) = NaN;
%     a(a(:,14) < 137.5,:) = NaN;
%     a(a(:,5) > 100,:) = NaN;

    b = a;
%     b(a(:,2) > 189.5,:) = NaN; %Azimuth
%     b(a(:,2) < 187.5,:) = NaN;
%     b(a(:,15) > 0,:) = NaN; %Elevation
    b(a(:,5) > 100,:) = NaN; %Tangential Altitude
%     b(a(:,15) < 15,:) = NaN;
    b = b(isfinite(b(:,1)),:);

    dimvectora = size(a);
    dimvectorb = size(b);
    dataL1{foo-2,1} = a;
    filtereddataL1{foo-2,1} = b;
    fid = fclose('all');
end

fclose('all');
```

```
%% Determine individual numbers of accesses
% This relies on the assumption that each access is separated by a ...
   time >>
% timestep of scenario

% Line 1: time step

accessfilteredL1 = zeros(numfiles,1);%/2,1);%/2,1);
accessL1 = zeros(numfiles,1);%/2,1);
durationfiltered = cell(numfiles,1);
startaccessf = cell(numfiles,1);
duration = cell(numfiles,1);
startaccess = cell(numfiles,1);
gain = cell(numfiles,1);
gainfiltered = cell(numfiles,1);
elrate = cell(numfiles,1);
starttime = cell(numfiles,1);
elratefiltered = cell(numfiles,1);
heightrate = cell(numfiles,1);
heightratefiltered = cell(numfiles,1);
% Split each GPS file into individual accesses

for foo = 1:numfiles

    % All Accesses
    time_vector = dataL1{foo,1}(:,1);
    time_vector = time_vector*24*60*60; %convert to seconds
    occults = round(diff(time_vector)) ≤ 70; %Timestep is 60 ...
       seconds, so find which are part of the same occultation
    edges = diff([0 occults' 0]); %find edges of accesses (1 = ...
       start, -1 = end)
    startaccess{foo,1} = find(edges == 1); %get indices of start of ...
       access == indices in time_vector
%     starttime{foo,1} = time_vector(edges == 1);
    endaccess = find(edges == -1); %get indices of end of access == ...
       indices in time_vector
```

```
    lengthoccults = endaccess - startaccess{foo,1}; %get lengths of ...
       runs (units = index = 10 s)
    lengthoccults = lengthoccults; % convert to minutes
    accessL1(foo) = length(lengthoccults);
    duration{foo,1} = lengthoccults;


    % Accesses filtered by radiometer FOV
    time_vectorf = filtereddataL1{foo,1}(:,1)*24*60*60; %convert to ...
       seconds
    occultsf = round(diff(time_vectorf)) ≤ 70; %Timestep is 60 ...
       seconds, so find which are part of the same occultation
    edgesf = diff([0 occultsf' 0]); %find edges of accesses (1 = ...
       start, -1 = end)
    startaccessf{foo,1} = find(edgesf == 1); %get indices of start ...
       of access == indices in time_vector
    endaccessf = find(edgesf == -1); %get indices of end of access ...
       == indices in time_vector
    starttime{foo,1} = datestr(time_vectorf(edgesf == 1)/24/60/60);
    lengthoccultsf = endaccessf - startaccessf{foo,1}; %get lengths ...
       of runs
    lengthoccultsf = lengthoccultsf; %convert to minutes
    accessfilteredL1(foo) = length(lengthoccultsf);
    durationfiltered{foo,1} = lengthoccultsf;

end


% figure(count)
% histogram(nonzeros(accessfilteredL1(:)),20);
% str = sprintf('Accesses to individual GPS satellites within ...
   Radiometer FOV over %0.0f days',timespan);
% title(str,'Fontsize',16);
% count = count + 1;
%
% figure%(count)
```

```
% histogram(nonzeros(accessL1(:)),20);
% str = sprintf('Laser Occultation Opportunities over %0.0f ...
   days',timespan);
% title(str,'FontSize',16);
% count = count + 1;

% figure(count)
% hist((filtereddataL1(:,1,:)-42522)*24);
% title('Time Distribution of Filtered Accesses','Fontsize',16)
% %datetick('x','HH:MM:SS')
% xlabel('Time (hours)')
% xlim([0 24])
% count = count+1;

% figure(count)
% subplot(1,2,1)
% ...
   histogram(nonzeros(cell2mat(cellfun(@(x)x(:),durationfiltered(:),'un',0))),20);
% % title('Overlapping Access Duration Distribution','Fontsize',16)
% xlabel('Time (min)');
% ylabel('Count')
% subplot(1,2,2)
% ...
   ecdf(nonzeros(cell2mat(cellfun(@(x)x(:),durationfiltered(:),'un',0))));
% xlabel('Time (min)');
% count = count + 1;

% fracstartaccessf = cell2mat(cellfun(@(x)x(:),starttime(:),'un',0));
% % fracstartaccessf = fracstartaccessf - fix(fracstartaccessf);
% figure(count)
% histogram(datestr((fracstartaccessf)/60/24/60));
% title('Filtered Access Start Time Distribution','Fontsize',16)
% xlabel('Time (min)');
% count = count + 1;

% ----------------------------------------
```

```
%% Make a bunch of datavectors because useful
% ----------------------------------------
% 1: Time
% 2: Tx Power
% 3: Tx Gain
% 4: Rx Gain
% 5: Range (km)
% 6: Free Space Loss
% 7: Atm loss
% 8: Tantenna
% 9: Doppler Shift (GHz...?)
% 10: Azimuth
% 11: Elevation
% 12: Elevation Rate
% 13: Latitude (tang point)
% 14: Longitude (tang point)
% 15: Tangential height (km)

time = cell(numfiles,1);
range = time;
% azimuth = time;
% el = time;
% elrate = time;
lat = time;
lon = time;
h = time;
hrate = h;

timef = cell(numfiles,1);
rangef = timef;
% azimuthf = timef;
% elf = timef;
% elratef = timef;
latf = timef;
lonf = timef;
hf = timef;
```

```
hratef = hf;

for foo = 1:numfiles

    time{foo,1} = dataL1{foo,1}(:,1);
%     azimuth{foo,1} = dataL1{foo,1}(:,2);
%     el{foo,1} = dataL1{foo,1}(:,3);
    range{foo,1} = dataL1{foo,1}(:,2);
    lat{foo,1} = dataL1{foo,1}(:,3);
    lon{foo,1} = dataL1{foo,1}(:,4);
    h{foo,1} = dataL1{foo,1}(:,5);

    timef{foo,1} = dataL1{foo,1}(:,1);
%     azimuthf{foo,1} = dataL1{foo,1}(:,2);
%     elf{foo,1} = dataL1{foo,1}(:,3);
    rangef{foo,1} = dataL1{foo,1}(:,2);
    latf{foo,1} = dataL1{foo,1}(:,3);
    lonf{foo,1} = dataL1{foo,1}(:,4);
    hf{foo,1} = dataL1{foo,1}(:,5);

    hrate{foo,1} = diff(dataL1{foo,1}(:,5))/30;
%     hrate{foo,1}(hrate{foo,1}>0) = [];
    hratef{foo,1} = diff(filtereddataL1{foo,1}(:,5))/30;
    hratef{foo,1}(hratef{foo,1}>0) = [];

    filtereddataL1{foo,1}((hratef{foo,1}>0),:) = NaN;
end


%% Create histograms and CDFs of access height rate (used to ...
   calculate resolution)
% ...
    ------------------------------------------------------------------------


% figure(count)
% subplot(1,2,1)
```

```
% histogram(nonzeros(cell2mat(cellfun(@(x)x(:),elrate(:),'un',0))),20);
% title('Histogram of Elevation Rate for All Setting ...
   Occultations','Fontsize',16)
% xlabel('Degrees/s');
% subplot(1,2,2)
% ecdf(nonzeros(cell2mat(cellfun(@(x)x(:),elrate(:),'un',0))));
% title('CDF of Elevation Rate for All Setting ...
   Occultations','Fontsize',16)
% xlabel('Degrees/s')
% count = count + 1;
%
figure%(count)
histogram(nonzeros(cell2mat(cellfun(@(x)x(:),rangef(:),'un',0))),30);
title('Range for Setting Occultations','Fontsize',16)
xlabel('Kilometers');
% count = count + 1;
%
figure%(count)
histogram(nonzeros(cell2mat(cellfun(@(x)x(:),hratef(:),'un',0))),30);
title('Tangential Height Rate for Setting Occultations','Fontsize',16)
xlabel('km/s');
% count = count + 1;
%
% figure(count)
% histogram(nonzeros(cell2mat(cellfun(@(x)x(:),hratef(:),'un',0))),100);
% title('Tangential Height Rate for Overlapping Setting ...
   Occultations','Fontsize',16)
% xlabel('km/s');
% count = count + 1;
%


% ----------------
% FOV PLOT WITH SNR


% ------------------------------------------------------------------
% ------------------------------------------------------------------
```

```
figure%(count)
hold on
landareas = shaperead('landareas.shp','UseGeoCoords',true);
axm  = axesm ('eqdcylin', 'Frame', 'on', 'Grid', 'on', 'AngleUnits', ...
   'degrees','MeridianLabel','On','ParallelLabel','On');
geoshow(landareas,'FaceColor',[1 1 1],'EdgeColor',[.6 .6 .6]);
for i = 1:numfiles
    scatter((flipud(filtereddataL1{i,1}(:,4))*pi/210),flipud(filtereddataL1{i,1}(:,3)*p:
end
hc = colorbar;
caxis([0 100]);
colormap jet
xlabel(hc,'Tangential Height (km)','Fontsize',14)
title('Setting Occultations for 400x30 and 400x150 ...
   Orbits','fontsize',16)
% xlabel('Longitude (Degrees)','fontsize',14)
% ylabel('Latitude (Degrees)','fontsize',14)
hold off
% count = count + 1;

figure%(count)
hold on
landareas = shaperead('landareas.shp','UseGeoCoords',true);
axm  = axesm ('eqdcylin', 'Frame', 'on', 'Grid', 'on', 'AngleUnits', ...
   'degrees','MeridianLabel','On','ParallelLabel','On');
geoshow(landareas,'FaceColor',[1 1 1],'EdgeColor',[.6 .6 .6]);
for i = 1:numfiles
    scatter((flipud(dataL1{i,1}(:,4))*pi/210),flipud(dataL1{i,1}(:,3)*pi/180),30,flipud
end
hc = colorbar;
caxis([0 500]);
colormap jet
xlabel(hc,'Tangential Height (km)','Fontsize',14)
title('All Accesses for 400x30 and 400x150 Orbits','fontsize',16)
% xlabel('Longitude (Degrees)','fontsize',14)
```

```
% ylabel('Latitude (Degrees)','fontsize',14)
hold off
% count = count + 1;

% ...
    ------------------------------------------------------------------------
% ------------------------------------------------------------------------

% figure(count)
% hist(accesstotalL2)
% title('Accesses to individual GPS satellites: L2')
% count = count + 1;

%% Plot tangential height versus azimuth for each access
%
% % % The 'proper' range, azimuth, and elevation (I think) are ...
    columns 5, 10, and 11,
% % % respectively
% %
% for foo = 1:numfiles
%     if not(isempty(filtereddataL1{foo,1}))
%         thetaf = filtereddataL1{foo,1}(:,10)*pi/180; %convert from ...
    degrees to radians
%         phif = filtereddataL1{foo,1}(:,11)*pi/180; %convert from ...
    degrees to radians
%         rf = ones(length(thetaf),1)*6378.4; ...
    %filtereddataL1{foo,1}(:,10);
%         theta = dataL1{foo,1}(:,10)*pi/180; %convert from degrees ...
    to radians
%         phi = dataL1{foo,1}(:,11)*pi/180; %convert from degrees to ...
    radians
%         r = ones(length(theta),1)*6378.4; %dataL1{foo,1}(:,10);
%         linkf = ...
    filtereddataL1{foo,1}(:,9)+30;%/max(db2mag(dataL1(:,12,i)));
%         tanheightf = filtereddataL1{foo,1}(:,15);
%         tanheight = dataL1{foo,1}(:,15);
```

```
% %          %     get rid of RAM-facing accesses
% %          for j = 1:length(theta)
% %              if theta(j) < pi/2 || theta(j) > 3*pi/2
% %                  theta(j) = NaN;
% %                  phi(j) = NaN;
% %                  r(j) = NaN;
% %              end
% %              if phi(j) > 15*pi/180
% %                  theta(j) = NaN;
% %                  phi(j) = NaN;
% %                  r(j) = NaN;
% %              end
% %          end
%
%          earththeta = linspace(0,2*pi)';
%          earthphi = -23*pi/180*ones(length(earththeta),1);
%          horphi = zeros(length(earththeta),1);
%          earthr = 6400*ones(length(earththeta),1);
%
%          [Xf, Yf, Zf] = sph2cart(thetaf,phif,rf);
%          [X, Y, Z] = sph2cart(theta,phi,r);
%          [Xe,Ye,Ze] = sph2cart(earththeta,earthphi,earthr);
%          [Xh,Yh,Zh] = sph2cart(earththeta,horphi,earthr);
%
%          Zf = Zf + 6378 + 810;
%          Z = Z + 6378 + 810;
%          Ze = Ze + 6378 + 810;
%          Zh = Zh + 6378 + 810;
%
% %          figure(count)
% %          hold on
% %          scatter3(X,Y,Z,5,[0.95 0.95 0.95],'filled')
% %          scatter3(Xf,Yf,Zf,10,'m','pentagram','filled')
% % %          plot3(Xe,Ye,Ze,'k','LineWidth',2)
% % %          plot3(Xh,Yh,Zh,'--k','LineWidth',2)
```

```
% %          % Create the sphere with Earth topography and adjust ...
   colormap
% %          surface(xx,yy,zz,props)
% %          colormap(topomap1)
% %          hold off
% %          axis equal off
% %          %     legend('All Accesses','Overlapping ...
   Accesses','Earth Tangent','Local Horizontal')
% %          count = count+1;
% %
%
%     end
% end
%
% %Plot all 'overlapping' accesses
%
% figure(count)
% ax1 = gca;
% hold on
% for goo = 1:numfiles
%
% % plot(thetaf*180/pi,tanheightf,':')
% %     plot(theta,height)
% %     ax2 = axes('Position',get(ax1,'Position'),...
% %        'XAxisLocation','bottom',...
% %        'YAxisLocation','right',...
% %        'Color','none',...
% %        'XColor','k','YColor','k');
% %     linkaxes([ax1 ax2],'x');
% %     hold on
% ...
   scatter(filtereddataL1{goo,1}(:,10),filtereddataL1{goo,1}(:,15),10,filtereddataL1{go
% end
% ylabel(ax1,'Tangential Height (km)','Fontsize',14) % label left y-axis
% %     ylabel(ax2,'Tangential Height (km)')
% ylim(ax1,[0 250])
```

```
% %     ylim(ax2,[-301 2287])
% xlim(ax1,[184 186])
% xlabel('Azimuth (degrees)','Fontsize',14)
% %   ylabel('Elevation (degrees)','Fontsize',14)
% str = sprintf('C/N0 (dB) for Access to GPS during Pitch-Up ...
   Maneuver',foo);
% title(str,'Fontsize',16);
% %     h = colorbar;
% hold off
% hc = colorbar;
% xlabel(hc,'C/N0 (dB)','Fontsize',14)
% count = count + 1;
%
%
% %% Plot link signal strength as function of elevation
% %
% % Link Margin (dB) is in column 12. Eb/N0 is in column 9
%
% for foo = 1:numfiles
%     if not(isempty(dataL1{foo,1}))
%         theta = dataL1{foo,1}(:,10);%*pi/180; %convert from ...
   degrees to radians
%         phi = dataL1{foo,1}(:,11);%*pi/180; %convert from degrees ...
   to radians
%         height = ...
   sqrt((6378.4+600)^2-6378.4^2).*tan((pi/2-asin(6378.4/6978.4)+phi*pi/180));
%         tanheight = dataL1{foo,1}(:,15);
%         r = ones(length(theta),1);
%         link = dataL1{foo,1}(:,5)+30;%/max(db2mag(dataL1(:,12,i)));
%         %link = diag(link);
%         %link(link==0) = NaN;
%
%         % get rid of RAM-facing accesses
%         for j = 1:length(theta)
%             if link(j) < -1000
%                 theta(j) = NaN;
```

```
%                   phi(j) = NaN;
%                   r(j) = NaN;
%                   link(j) = NaN;
%                   height(j) = NaN;
%               end
%               if phi(j) > 30
%                   theta(j) = NaN;
%                   phi(j) = NaN;
%                   r(j) = NaN;
%                   link(j) = NaN;
%                   height(j) = NaN;
%               end
%               if theta(j) > 270 || theta(j) < 90
%                   theta(j) = NaN;
%                   phi(j) = NaN;
%                   r(j) = NaN;
%                   link(j) = NaN;
%                   height(j) = NaN;
%               end
%           end
%
%           %[X Y Z] = sph2cart(theta,phi,r);
%
% %           figure(count)
% %           ax2 = gca;
% %           hold on
% % % %           plot(theta,tanheight,':')
% %           scatter(theta,tanheight,20,link,'filled','Parent',ax2);
% %           ylabel(ax2,'Tangential Height (km)','Fontsize',14) % ...
    label left y-axis
% %           ylim(ax2,[0 100])
% %           xlim(ax2,[90 270])
% %           xlabel('Azimuth (degrees)','Fontsize',14)
% %           str = sprintf('C/N0 (dB) for Access to GPS %0.0f during ...
    Pitch-Up Maneuver',foo);
% %           title(str,'Fontsize',16);
```

```
% %          hc = colorbar;
% %          xlabel(hc,'C/N0 (dB)','Fontsize',14)
% %          hold off
% %          count = count + 1;
%
%      end
%
% end
```

A.1.2 Temperature Precision

```
%%%%%%%%%%%%%%%%%%%%%%%%%%%%%%%%%%%%%%%%%%%%%%%%%%%%%%%%
% File Name: reyutp_Earth
% Created by: Renyu, modified for earth by Annie Marinan and Kerri Cahoy
% Description:    This code generates vectors of bending angle and ...
    impact factor
%                 representative of Earth and computes the ...
    associated refractivity
%                 using a power law approximation through the Abel ...
    transform
%                 (courtesy David Hindel)
% Required functions: Gj.m
%                     Fj.m
%                     Lgamma.m
%%%%%%%%%%%%%%%%%%%%%%%%%%%%%%%%%%%%%%%%%%%%%%%%%%%%%%%%

clear all;
close all;

%function [T,Pb,mu] = renyutp(alpha,a)

% Renyu's code to retreive Temp/Press from a & alpha
% set up examples of impact parameter a and bending angle theta
% comment out to use your own a and theta
```

```
% A=3385; % km Mars
A = 6371; %km Earth
% Theta1=1.95E-4; % Mars
Theta1 = 1.745e-2; % radians, bending angle at surface of earth
% s1=365; % Mars
s1 = A/7.5; % Assume scale height 7, Re 6371
% Theta2=1.4E-4; % Mars, second term
% s2=3650; % Mars, second term
TT=1; % one term 1 / two term 2

apre=0.1; % 100-m steps
height=250; % km
rcontrol=80;
jcontrol=rcontrol/apre;

a=A:apre:(A+height); % impact parameter
N=size(a,2);
theta=Theta1*(A./a).^s1;
if TT==2
    theta=Theta1*(A./a).^s1+Theta2*(A./a).^s2;
end

% Add noise to theta based on bending angle error
% for r = 1:1000
    DesiredSD = 0.4e-9;        % sigma_alpha from Link calculations
    epsilon = random('norm',0,DesiredSD,[1 length(theta)]);  % some ...
       random noise
%     theta_noise_matrix(r,:) = theta + epsilon;
    theta_noise = theta + epsilon;
% end

% theta_noise = mean(theta_noise_matrix,1);

%retrieve from a and theta
%N is the total number of data points
```

```
% % Not sure what this is (commented section below), don't think we ...
   need it
% right now
% a2p = a2(1500:end-8);
% alphap = alpha(1500:end-8);
%
% [aa,ind] = sort(a2p);
% a        = a2p(ind);
% theta    = -(alphap(ind));

% % For function form, pick step size automatically
% N = size(a,1);
% mu = zeros(1,N);
% v = zeros(1,N);
% r = zeros(1,N);
% apre = (max(a)-min(a))/N;

% linear interpolation

for i=1:N-1
    C(i)=(theta(i+1)-theta(i))/(a(i+1)-a(i));
    D(i)=(theta(i+1)+theta(i))/2-C(i)*(a(i+1)+a(i))/2;

    C_noise(i)=(theta_noise(i+1)-theta_noise(i))/(a(i+1)-a(i));
    D_noise(i)=(theta_noise(i+1)+theta_noise(i))/2-C(i)*(a(i+1)+a(i))/2;
end



for j=1:N-1
    kerr=0;
    kerr_noise = 0;
    for i=j:N-1
        kerr=kerr+C(i)*(Gj(a(j),a(i+1))-Gj(a(j),a(i)))+D(i)*(Fj(a(j),a(i+1))-Fj(a(j),a(
        kerr_noise=kerr_noise+C_noise(i)*(Gj(a(j),a(i+1))-Gj(a(j),a(i)))+D_noise(i)*(Fj
    end
```

```
mu(j)=exp(kerr/pi);
r(j)=a(j)/mu(j);
v(j)=(mu(j)-1)*1E+6; %refractivity in N units

mu_noise(j)=exp(kerr_noise/pi);
r_noise(j)=a(j)/mu_noise(j);
v_noise(j)=(mu_noise(j)-1)*1E+6;

% The following is for verification purpose only. Comment out if ...
   you using your own a and theta

a_c(j)=a(j);
rerr=1;
if j<jcontrol
while rerr>1E-9
kerr_c=Theta1*(A/a_c(j))^s1/2/sqrt(pi)*exp(LGamma(s1/2)-LGamma((s1+1)/2));
if TT==2
    kerr_c=kerr_c+Theta2*(A/a_c(j))^s2/2/sqrt(pi)*exp(LGamma(s2/2)-LGamma((s2+1)/2);
end
mu_c(j)=exp(kerr_c);
r_c(j)=a_c(j)/mu_c(j);
rerr=abs(r_c(j)-r(j));
a_c(j)=mu_c(j)*r(j);
end
else
kerr_c=Theta1*(A/a_c(j))^s1/2/sqrt(pi)*exp(LGamma(s1/2)-LGamma((s1+1)/2));
if  TT==2
    kerr_c=kerr_c+Theta2*(A/a_c(j))^s2/2/sqrt(pi)*exp(LGamma(s2/2)-LGamma((s2+1)/2);
end
mu_c(j)=exp(kerr_c);
r_c(j)=a_c(j)/mu_c(j);
end
v_c(j)=(mu_c(j)-1)*1E+6;

err(j)=abs(v(j)-v_c(j))/v_c(j);
```

```
end

% Compute P and T from retrieved mu

kb=1.38065E-23; % Bolzmann constant, SI

% kappa=1.804E-29;% Mars, SI
% m=7.221E-26;     % Mars mean molecular mass, SI
% g=3.7;           % Mars acceleration of gravity, SI

% Cannot confirm earth kappa yet, skipping these for now
kappa = 6.138e-29;       % Earth refractive volume, SI (Van der Waals ...
    radius calculation?)
% NOTE: for calculations using kappa, comment out avogadro's number ...
    in m
m = 28.97*1.661e-27*6.022e23;     % Earth mean molecular mass, kg ...
    (dry air) [NASA Earth Fact Sheet] multiplied by amu to SI conversion
g = 9.81;                % Earth acceleration of gravity, SI
b1 = 77.6;               % Earth, N-unit K/mbar
R = 8.31447;             % m^3 ?mbar ?/K/?(kg)mol

nu=v*1E-6; % refractivity
nu_c = v_c*1E-6;
nu_noise = v_noise*1e-6;
n=nu/kappa; % number density
n_c = nu_c/kappa;
n_noise = nu_noise/kappa;
rho = v*m/b1/R; % air density, kg/m^3
rho_c = v_c*m/b1/R;
rho_noise = v_noise*m/b1/R;
dd=apre*1E+3; % layer thickness in m %Eventually want to make this ...
    Fresnel Zone Diameter - roughly 1.4 km, but alt-dependent

% N1=size(n,2);                    % Comment out to calculate using ...
    v,m,b1,R
```

```
% N1_c = size(n_c,2);              % Comment out to calculate using ...
   v,m,b1,R
N1 = size(rho,2);                 % Comment out to calculate using kappa
N1_noise = size(rho_noise,2);
P=zeros(1,N1);
P_noise = zeros(1,N1_noise);
N1_c = size(rho_c,2);             % Comment out to calculate using kappa
P_c = zeros(1,N1_c);
for i=N1:-1:1
    add=rho(i)*g*dd; %dp = r*rho*dr % Comment out to calculate using ...
       kappa
    %     add = n(i)*m*g*dd;          % Comment out to calculate ...
       using v,m,b1,R
    for j=1:i
        P(j)=P(j)+add;
    end
end

for i=N1_c:-1:1
    add=rho_c(i)*g*dd; %dp = r*rho*dr  % Comment out to calculate ...
       using kappa
%     add = n_c(i)*m*g*dd;          % Comment out to calculate using ...
   v,m,b1,R
    for j=1:i
        P_c(j)=P_c(j)+add;
    end
end

for i=N1_noise:-1:1
    add=rho_noise(i)*g*dd; %dp = r*rho*dr  % Comment out to ...
       calculate using kappa
%     add = n_noise(i)*m*g*dd;          % Comment out to calculate ...
   using v,m,b1,R
    for j=1:i
        P_noise(j)=P_noise(j)+add;
    end
```

```
end

% T=P./n/kb;                          % Comment out to calculate using ...
    v,m,b1,R
% T_c = P_c./n_c/kb;                  % Comment out to calculate using ...
    v,m,b1,R
% T_noise = P_noise./n_noise/kb;

T=P./v*77.6; % N = 77.6 P/T (Kursinki thesis, eq 2.3.2)  % Comment ...
    out to
% calculate using kappa
T_c=P_c./v_c*77.6;              % Comment out to calculate using kappa
T_noise = P_noise./v_noise*77.6;

Pb = P*1e-5;
% Pb_c=P_c*1E-5; % pressure in bar
Pb_noise = P_noise*1e-5;

% Plot refractivity calculation error

% Plot Temperature calculation error

err_noise_t = abs((T_noise - T)./T);
err_T_calc = abs((T_c-T));

figure
semilogx(err_noise_t,r-A,'LineWidth',2)
title('Temperature Error due to Bending Angle Error','Fontsize',16)
xlabel('Fractional Temperature Error','Fontsize',14)
ylabel('Height (km)','Fontsize',14)
ylim([0 50])

figure
semilogx(abs(T_noise-T),r-A,'LineWidth',2)
title('Temperature Error due to Bending Angle Error','Fontsize',16)
xlabel('Temperature Error (K)','Fontsize',14)
```

```
ylabel('Height (km)','Fontsize',14)
ylim([0 50])

figure
semilogx(err_T_calc,r-A,'LineWidth',2)
title('Temperature Error due to Computational Error','Fontsize',14)
xlabel('Temperature Error (K)','Fontsize',14)
ylabel('Height (km)','Fontsize',14)
ylim([0 50])



figure
hold on
plot(T,r-A,'b','LineWidth',2)
plot(T_noise,r-A,'.r','LineWidth',2)
hold off
title('Temperature as a Function of Height','Fontsize',16)
xlabel('Temperature (K)')
ylabel('Height (km)')
ylim([0 50])
xlim([200 300])
legend('Truth','With Bending Angle Error');

figure
hold on
semilogx(abs(theta_noise(1:2500)-theta(1:2500)),r-A,'LineWidth',2)
hold off
title('Bending Angle Error as a Function of Height','Fontsize',16)
xlabel('Bending Angle Error (rad)','Fontsize',14)
ylabel('Height (km)','Fontsize',14)
ylim([0 50])




% figure
% plot(P,r-A,'LineWidth',2)
```

```
% title('Pressure as a Function of Height','Fontsize',16)
% xlabel('Pressure (bar)')
% ylabel('Height (km)')
%
% figure
% plot(v,r-A,'LineWidth',2)
% title('Refractivity as a Function of Height','Fontsize',16)
% xlabel('Refractivity (N-units)')
% ylabel('Height (km)')
```

A.2 Open-Loop Wavefront Reconstruction

```
%%%%%%%%%%%%%%%%%%%%%%%%%%%%%%%%%%%%%%%%%%%%%%%%%%%%%%%%
% File: DM_control_script
% Made by: Annie Marinan
% Last modified: 03/02/2016
%
% Description:  This script is a function-free version of the
% DM_control_main code that was difficult to debug
%               Steps involved: (1) Define System Variables
%                               (2) Set 'grid' geometry
%                               (3) Read in reference spots to find
%                               centroid
%                               (3a) Find centroid locations of ...
    reference
%                               spots by gridpoint
%                               (4) Read in Δ spot measurement and find
%                               centroid locations by gridpoint
%                               (5) Compute dx and dy vectors
%                               (6) Reconstruct wavefront (mirror ...
    surface
%                               measurement)
%
```

```
% Required Functions: FastPeakFind - reference centroid list
%                     Ref_Spotfield - find all spots
%                     DeMi_Calibration - find rotation and zoom offset
%                     DeMi_Interaction - automate poking actuators to
%                     calculate interaction matrix
%%%%%%%%%%%%%%%%%%%%%%%%%%%%%%%%%%%%%%%%%%%%%%%%%%%%

% clear all;
% close all;
% set(0,'DefaultFigureWindowStyle','docked');

function [W num_grid_across] = DM_Open_Loop(file)


%% 1. Define physical system parameters (SI units)

% Misc System Stuff
max_rms_error = 0.05; % um
system_mag = 2; %magnification of the system between the mirror and LA
lambda = 635e-3; % um, wavelength of laser

% Mirror
mirror_d = 1000; % um, or 1.5 mm mirror diameter
actuator_pitch = 300; % um, mirror actuator pitch

% Lenslet Array (LA)
lenslet_pitch = 150; % um lenslet pitch
lenslet_f = 6700; % um lenslet individual focal length

% Detector
pixel_pitch = 5.2; %um pixel pitch
det_x = 1280; % number of pixels in x-dimension (Matlab columns)
det_y = 1024; % number of pixels in y-dimension (Matlab rows)

% Control Loop Parameters
k_l = 0.02;
```

```
k_0 = 0.3;


%% 2. Generate the 'grid' of system-defined boxes on the detector

% Determine number of grid points across (assuming beam circumscribes
% mirror)

num_grid_across = floor(mirror_d*system_mag*sqrt(2)/lenslet_pitch);
if mod(num_grid_across,2) == 0
    num_grid_across = num_grid_across - 1;
end

% Define x- and y- vectors of grid centroids
n = floor(num_grid_across/2);
l2p = lenslet_pitch/pixel_pitch;
v_row = (-n*l2p):(l2p):(n*l2p);
v_col = v_row;

%% 3. Read in reference spot image and find centroid

% [camera_handle, camera_frame] = OPEN_CAMERA_TL_DCx_64bit;
% avgref = GRAB_FRAME_TL_DCx_64bit(camera_handle,camera_frame);

cd('C:\Users\Annie-MIT\Documents\MATLAB\20160419_BMC');
% cd('D:\MATLAB\20150821_BMC');
% avgref = zeros(1024,1280);
% for i = 1:4
%     avgref = avgref + im2double(rgb2gray(imread('Flat_100_1.tif',i)));
% end
% avgref = avgref./4;
avgref = rgb2gray(imread('Flat_pull_20160419.tif'));
intensity_avg = mean(mean(avgref));
intensity_std = std(std(double(avgref)));
scale = intensity_avg + 3*intensity_std; %for spots, want pixels ...
   where intensity is at least 4 stddev above background
```

```
% Compute physical center of spotfield (nonweighted average of centroid
% locations) and identify the spot closest to the center
% [refcent statsref] = Ref_Spotfield(avgref);
[refcent, statsref] = Ref_Spotfield(avgref);
com_ref_x = mean(refcent(:,1));
com_ref_y = mean(refcent(:,2));
DTr = delaunayTriangulation(refcent);
centspotloc = nearestNeighbor(DTr,[com_ref_x com_ref_y]);

%% 3a. Find spots within grid points

% Move grid to be centered on previously-identified center spot

v_row = v_row + refcent(centspotloc,1);
v_col = v_col + refcent(centspotloc,2);

[VROW, VCOL] = meshgrid(v_row,v_col);
grid_flat_row = reshape(VROW,1,num_grid_across*num_grid_across);
grid_flat_col = reshape(VCOL,1,num_grid_across*num_grid_across);

% Perform FastPeakFind in regions of gridpoints to find centroid ...
    locations
% of spots within grid
% Also do sanity check plot on where the spotfield is being cropped

% figure
% ha = tight_subplot(27,27,[0.001 0.001],0.001,[0.001 0.001]);
clim = [0 63];
for hoo = 1:num_grid_across^2
    rowstart = floor(grid_flat_row(hoo)-l2p/2);
    colstart = floor(grid_flat_col(hoo)-l2p/2);
    gridcrop(:,:,hoo) = avgref(colstart:colstart + ...
        ceil(l2p),rowstart:rowstart+ceil(l2p));
    peaks = FastPeakFind(uint16(gridcrop(:,:,hoo)),scale,4,0,2);
```

```
    %           axes(ha(index));
    %           h1 = imagesc(gridcrop(:,:,foo));
    %           hold on
    %           if not(isempty(peaks))
    %               plot(peaks(1),peaks(2),'bs')
    %           end
    %           hold off
    % %           set(h1,'alphadata',(~isnan(scaled_phase(:,:,index))));
    %           caxis(clim)
    %           colormap(gray)
    %           axis equal
    %           axis off

    if isempty(peaks)
        spotcent_row(hoo) = NaN;
        spotcent_col(hoo) = NaN;
        peakvector(hoo,:) = [NaN NaN];
    else
        spotcent_row(hoo) = (rowstart-1) + peaks(1);
        spotcent_col(hoo) = (colstart-1) + peaks(2);
        peakvector(hoo,:) = [peaks(1) peaks(2)];
    end
end

% Overlay grid on top of spotfield

%% 3b. Rotate image to keep grid straight to start with (can't ...
    correct rotation with mirror)

% Vector of spot centroids is in pixel units. Want origin to be at ...
    center
% of grid to get correct rotation.
spotcent_row_rot = spotcent_row - refcent(centspotloc,1);
spotcent_row_rot = ...
    reshape(spotcent_row_rot,num_grid_across,num_grid_across);
```

```
spotcent_row_rot = ...
    spotcent_row_rot(6:num_grid_across-5,6:num_grid_across-5);
spotcent_row_rot = reshape(spotcent_row_rot,1,(num_grid_across-10)^2);
spotcent_col_rot = spotcent_col - refcent(centspotloc,2);
spotcent_col_rot = ...
    reshape(spotcent_col_rot,num_grid_across,num_grid_across);
spotcent_col_rot = ...
    spotcent_col_rot(6:num_grid_across-5,6:num_grid_across-5);
spotcent_col_rot = reshape(spotcent_col_rot,1,(num_grid_across-10)^2);

% Do the same thing with inital grid.

grid_flat_row_rot = grid_flat_row - refcent(centspotloc,1);
grid_flat_row_rot = ...
    reshape(grid_flat_row_rot,num_grid_across,num_grid_across);
grid_flat_row_rot = ...
    grid_flat_row_rot(6:num_grid_across-5,6:num_grid_across-5);
grid_flat_row_rot = reshape(grid_flat_row_rot,1,(num_grid_across-10)^2);
grid_flat_col_rot = grid_flat_col - refcent(centspotloc,2);
grid_flat_col_rot = ...
    reshape(grid_flat_col_rot,num_grid_across,num_grid_across);
grid_flat_col_rot = ...
    grid_flat_col_rot(6:num_grid_across-5,6:num_grid_across-5);
grid_flat_col_rot = reshape(grid_flat_col_rot,1,(num_grid_across-10)^2);

% Now use rotation matrix and least squares solve to figure out most ...
    likely
% rotation. R = [cosTheta -sinTheta; sinTheta cosTheta]

x_model = vertcat(spotcent_col_rot,spotcent_row_rot);
nanmodel = isnan(x_model);
x_meas = vertcat(grid_flat_col_rot,grid_flat_row_rot);
nanmeas = isnan(x_meas);
x_model(:,or(nanmodel(1,:),nanmeas(1,:))) = [];
x_meas(:,or(nanmodel(1,:),nanmeas(1,:))) = [];
```

```
R = (x_meas')\(x_model');

theta = mean([asind(abs(R(1,2))),asind(abs(R(2,1)))]);
rotatedimage = imrotate(avgref,-theta);
% figure
% imagesc(rotatedimage)

%-------------------------------------------------------------------------
%% 4. Re-do spot finding for rotated image

intensity_std = std(std(double(rotatedimage)));
scale_rot = intensity_avg + 5*intensity_std; %for spots, want pixels ...
    where intensity is at least 4 stddev above background

% Compute physical center of spotfield (nonweighted average of centroid
% locations) and identify the spot closest to the center
[refcent_rot statsref] = Ref_Spotfield(rotatedimage);
com_ref_x_rot = mean(refcent_rot(:,1));
com_ref_y_rot = mean(refcent_rot(:,2));
DTr = delaunayTriangulation(refcent_rot);
centspotloc_rot = nearestNeighbor(DTr,[com_ref_x_rot com_ref_y_rot]);

% Find spots within grid points

% Move grid to be centered on previously-identified center spot

v_row = v_row - refcent(centspotloc,1) + refcent_rot(centspotloc_rot,1);
v_col = v_col - refcent(centspotloc,2) + refcent_rot(centspotloc_rot,2);

[VROW, VCOL] = meshgrid(v_row,v_col);
grid_flat_row = reshape(VROW,1,num_grid_across*num_grid_across);
grid_flat_col = reshape(VCOL,1,num_grid_across*num_grid_across);

% Perform FastPeakFind in regions of gridpoints to find centroid ...
    locations
% of spots within grid
```

```
% Also do sanity check plot on where the spotfield is being cropped

% figure
% ha = tight_subplot(27,27,[0.001 0.001],0.001,[0.001 0.001]);
clim = [0 63];
for hoo = 1:num_grid_across^2
    rowstart = floor(grid_flat_row(hoo)-l2p/2);
    colstart = floor(grid_flat_col(hoo)-l2p/2);
    gridcrop_rot(:,:,hoo) = rotatedimage(colstart:colstart + ...
        ceil(l2p),rowstart:rowstart+ceil(l2p));
%     gridcrop_rot(:,:,hoo) = rotatedimage(rowstart:rowstart + ...
    ceil(l2p),colstart:colstart+ceil(l2p));

    peaks = FastPeakFind(uint16(gridcrop_rot(:,:,hoo)),scale_rot,4,0,2);

    %           axes(ha(index));
    %           h1 = imagesc(gridcrop(:,:,foo));
    %           hold on
    %           if not(isempty(peaks))
    %               plot(peaks(1),peaks(2),'bs')
    %           end
    %           hold off
    % %           set(h1,'alphadata',(~isnan(scaled_phase(:,:,index))));
    %           caxis(clim)
    %           colormap(gray)
    %           axis equal
    %           axis off

    if isempty(peaks)
        spotcent_row_rot(hoo) = NaN;
        spotcent_col_rot(hoo) = NaN;
        peakvector(hoo,:) = [NaN NaN];
    else
        spotcent_row_rot(hoo) = (rowstart-1) + peaks(1);
        spotcent_col_rot(hoo) = (colstart-1) + peaks(2);
        peakvector(hoo,:) = [peaks(1) peaks(2)];
```

```
    end
end

% ...
    ------------------------------------------------------------------------

%% 5. Read in and Rotate Measured Spot Image

% avgmeas = rgb2gray(imread('Poke_03_100.tif'));
% avgmeas = rgb2gray(imread(file));
avgmeas = zeros(1024,1280);
for i = 1:4
    avgmeas = avgmeas + im2double(rgb2gray(imread(file,i)));
end
avgmeas = avgmeas./4;

avgmeas = imrotate(avgmeas,-theta);



% Find spots within grid points

[meascent statsmeas] = Ref_Spotfield(avgmeas);
com_meas_x = mean(meascent(:,1));
com_meas_y = mean(meascent(:,2));
DTr = delaunayTriangulation(meascent);
centspotmeas = nearestNeighbor(DTr,[com_meas_x com_meas_y]);

v_row = v_row - refcent_rot(centspotloc_rot,1) + ...
    meascent(centspotmeas,1);
v_col = v_col - refcent_rot(centspotloc_rot,2) + ...
    meascent(centspotmeas,2);

[VROW, VCOL] = meshgrid(v_row,v_col);
grid_flat_row_meas = reshape(VROW,1,num_grid_across*num_grid_across);
grid_flat_col_meas = reshape(VCOL,1,num_grid_across*num_grid_across);
```

```
% Perform FastPeakFind in regions of gridpoints to find centroid ...
    locations
% of spots within grid
% Also do sanity check plot on where the spotfield is being cropped

% figure
% ha = tight_subplot(27,27,[0.001 0.001],0.001,[0.001 0.001]);
clim = [0 63];
for hoo = 1:num_grid_across^2
    rowstartmeas = floor(grid_flat_row_meas(hoo)-l2p/2);
    colstartmeas = floor(grid_flat_col_meas(hoo)-l2p/2);
    gridcropmeas(:,:,hoo) = avgmeas(colstartmeas:colstartmeas + ...
        ceil(l2p),rowstartmeas:rowstartmeas+ceil(l2p));
%     gridcrop(:,:,hoo) = avgmeas(rowstart:rowstart + ...
    ceil(l2p),colstart:colstart+ceil(l2p));

    peaksmeas = FastPeakFind(uint16(gridcropmeas(:,:,hoo)),scale,4,0,2);

    %           axes(ha(index));
    %           h1 = imagesc(gridcrop(:,:,foo));
    %           hold on
    %           if not(isempty(peaks))
    %               plot(peaks(1),peaks(2),'bs')
    %           end
    %           hold off
    % %           set(h1,'alphadata',(~isnan(scaled_phase(:,:,index))));
    %           caxis(clim)
    %           colormap(gray)
    %           axis equal
    %           axis off

    if isempty(peaksmeas)
        spotcent_rowmeas(hoo) = NaN;
        spotcent_colmeas(hoo) = NaN;
        peakvectormeas(hoo,:) = [NaN NaN];
    else
```

```
        spotcent_rowmeas(hoo) = (rowstartmeas-1) + peaksmeas(1);
        spotcent_colmeas(hoo) = (colstartmeas-1) + peaksmeas(2);
        peakvectormeas(hoo,:) = [peaksmeas(1) peaksmeas(2)];
    end
end

% Plot with grid overlaid on spotfield

% figure
% imagesc(avgmeas);
% colormap(gray)
% colorbar('vert')
% hold on;
% for foo = 1:num_grid_across
%     rowstartmeas = v_row(foo) - 12p/2;
%     for goo = 1:num_grid_across
%         colstartmeas = v_col(goo) - 12p/2;
%         rectangle('position', [rowstartmeas, colstartmeas, 12p, ...
   12p],'EdgeColor','r');
%     end
% end
% plot(spotcent_rowmeas,spotcent_colmeas,'bs')
% hold off
% axis equal tight
% set(gca,'YDir','normal')
% title('Measured Spotfield with Grid (red) and Centroids ...
   (blue)','Fontsize',16)


%% 6. Generate x-y displacement vectors:

% X-direction: column motion
% Y-direction: row motion
%It's unclear which is supposed to be x and which is supposed to be y.
```

```
Δx_ref = (spotcent_rowmeas - grid_flat_row_meas) - (spotcent_row_rot ...
    - grid_flat_row); % Compare measured to reference
% (unactuated mirror)
Δy_ref = (spotcent_colmeas - grid_flat_col_meas) - (spotcent_col_rot ...
    - grid_flat_col); % Compare measured to reference
% (unactuated mirror)

Δx_th = spotcent_rowmeas - grid_flat_row_meas; % Compare measured to ...
    flat
Δy_th = spotcent_colmeas - grid_flat_col_meas; % Compare measured to ...
    flat

Δx_rot = spotcent_row_rot - grid_flat_row;
Δy_rot = spotcent_col_rot - grid_flat_col;

Δx_unrot = spotcent_row - grid_flat_row;
Δy_unrot = spotcent_col - grid_flat_col;

% Generate quiver plot based on this information. Use original ...
    location of
% spots as points and Δx/Δy as vectors

figure
hold on
imagesc(avgmeas)
colormap(gray)
colorbar('vert')
quiver(grid_flat_row,grid_flat_col,Δx_ref,Δy_ref,0.5,'c','filled','LineWidth',2)
hold off
axis equal tight
set(gca,'YDir','normal')
title('Spot Movement Superimposed on Grid','Fontsize',16)

% figure
% hold on
% imagesc(avgmeas)
```

```
% colormap(gray)
% colorbar('vert')
% ...
    quiver(spotcent_row_rot,spotcent_col_rot,Δx_ref,Δy_ref,0.5,'c','filled','LineWidth',
% hold off
% axis equal tight
% set(gca,'YDir','normal')
% title('Spot Movement Superimposed on Reference ...
    Spotfield','Fontsize',16)

% figure
% hold on
% imagesc(avgmeas)
% colormap(gray)
% colorbar('vert')
% ...
    quiver(grid_flat_row,grid_flat_col,Δx_rot,Δy_rot,0.5,'c','filled','LineWidth',2)
% hold off
% axis equal tight
% set(gca,'YDir','normal')
% title('Rotated Reference Spot Deltas','Fontsize',16)

% figure
% hold on
% imagesc(avgmeas)
% colormap(gray)
% colorbar('vert')
% ...
    quiver(grid_flat_row,grid_flat_col,Δx_unrot,Δy_unrot,0.5,'c','filled','LineWidth',2)
% hold off
% axis equal tight
% set(gca,'YDir','normal')
% title('UnRotated Reference Spot Deltas','Fontsize',16)

% Convert Δx and Δy vectors to dz/dx and dz/dy based on lenslet
% properties
```

```
dzdx = atan(Δx_ref*pixel_pitch./lenslet_f);
% dzdx = reshape(dzdx,num_grid_across,num_grid_across);
dzdy = atan(Δy_ref*pixel_pitch./lenslet_f);
% dzdy = reshape(dzdy,num_grid_across,num_grid_across);




%% 10. Reconstruct the wavefront by actually doing the math (Southwell)

dx = ...
    reshape(Δx_ref*pixel_pitch/lenslet_f*lenslet_pitch,num_grid_across,num_grid_across);
dy = ...
    reshape(Δy_ref*pixel_pitch/lenslet_f*lenslet_pitch,num_grid_across,num_grid_across);

Sx = dx;
Sx = reshape(Sx,1,num_grid_across^2);
Sx(isnan(Sx)) = 0;
Sy = dy;
Sy = reshape(Sy,1,num_grid_across^2);
Sy(isnan(Sy)) = 0;
Sx = reshape(Sx,num_grid_across,num_grid_across);
Sy = reshape(Sy,num_grid_across,num_grid_across);

W = zonalReconstruction(Sx, Sy, 1);

% W = intgrad2( Sx, Sy );
figure;
minima = min(min(W));
if( minima < 0 )
   minima = abs(minima);
else
   minima = 0;
end
surf(W+minima)
```

```
colorbar
title('3D plot')
set(gca,'XTickLabel',[0:lenslet_pitch:num_grid_across*lenslet_pitch]);
set(gca,'YTickLabel',[0:lenslet_pitch:num_grid_across*lenslet_pitch]);
set(gca,'xtick',[0:1:num_grid_across]);
set(gca,'ytick',[0:1:num_grid_across]);
xlabel('x-position in [um]')
ylabel('y-position in [um]')
zlabel('z-height in [um]')

% subplot(2,1,2);
% quiver(xDefault,yDefault,dx,dy,0)
% title('measured slopes')
% ylabel('pixel y-axis')
% xlabel('pixel x-axis')
% grid on
% axis([0 224 0 224])
% % change grid spacing
% set(gca,'xtick',[0:l2p:num_grid_across*l2p]);
% set(gca,'ytick',[0:l2p:num_grid_across*l2p]);

set(gcf, 'PaperPosition', [0 0 20 20]); %Position plot at left hand ...
   corner with width 5 and height 5.
set(gcf, 'PaperSize', [20 20]); %Set the paper to have width 5 and ...
   height 5.
saveas(gcf, 'test3', 'pdf') %Save figure
```

A.3 Closed-Loop Wavefront Control

A.3.1 Calibration

```
%%%%%%%%%%%%%%%%%%%%%%%%%%%%%%%%%%%%%%%%%%%%
% File: DM_control_script
```

```
% Made by: Annie Marinan
% Last modified: 03/02/2016
%
% Description:  This script is a function-free version of the
% DM_control_main code that was difficult to debug
%                Steps involved: (1) Define System Variables
%                                (2) Set 'grid' geometry
%                                (3) Read in reference spots to find
%                                centroid
%                                (4) Find centroid locations of reference
%                                spots by gridpoint
%                                (5) Calculate rotation and zoom offset
%
% Required Functions: FastPeakFind - reference centroid list
%                     Ref_Spotfield - find all spots
%%%%%%%%%%%%%%%%%%%%%%%%%%%%%%%%%%%%%%%%%%%%%%%%%%%%

clear all;
close all;
set(0,'DefaultFigureWindowStyle','docked');

% function [dzdx dzdy] = DM_control_script(file)


%% 1. Define physical system parameters (SI units)

% Misc System Stuff
max_rms_error = 0.05; % um
system_mag = 2; %magnification of the system between the mirror and LA
lambda = 635e-3; % um, wavelength of laser

% Mirror
mirror_d = 1500; % um, or 1.5 mm mirror diameter
actuator_pitch = 300; % um, mirror actuator pitch

% Lenslet Array (LA) in California
```

```
lenslet_pitch = 150; % um lenslet pitch
lenslet_f = 6700; % um lenslet individual focal length

% Lenslet Arary (LA) at MIT
% lenslet_pitch = 300; % um lenslet pitch
% lenslet_f = 6700; % um lenslet individual focal length

% Detector
pixel_pitch = 5.2; %um pixel pitch
det_x = 1280; % number of pixels in x-dimension (Matlab columns)
det_y = 1024; % number of pixels in y-dimension (Matlab rows)

% Actuator Stroke
stroke = 100;

%% 2. Generate the 'grid' of system-defined boxes on the detector

% Determine number of grid points across (assuming beam circumscribes
% mirror)

num_grid_across = floor(mirror_d*system_mag*sqrt(2)/lenslet_pitch);
if mod(num_grid_across,2) == 0
    num_grid_across = num_grid_across - 1;
end

% Define x- and y- vectors of grid centroids
n = floor(num_grid_across/2);
l2p = lenslet_pitch/pixel_pitch;
v_row = (-n*l2p):(l2p):(n*l2p);
v_col = v_row;

%% 3. Read in reference spot image (from camera, no actuators poked) ...
   and find centroid

[camera_handle, camera_frame] = OPEN_CAMERA_TL_DCx_64bit;
SET_PIXCLK_EXPTIME_FPS_TL_DCx_64bit(camera_handle,5,0,10);
```

```
avgref = GRAB_FRAME_TL_DCx_64bit(camera_handle,camera_frame);
avgref = avgref';

% avgref = rgb2gray(imread('Flat_1.tif'));
intensity_avg = mean(mean(avgref));
intensity_std = std(std(double(avgref)));
scale = intensity_avg + 5*intensity_std; %for spots, want pixels ...
    where intensity is at least 4 stddev above background

% Compute physical center of spotfield (nonweighted average of centroid
% locations) and identify the spot closest to the center
[refcent statsref] = Ref_Spotfield(avgref);
com_ref_x = mean(refcent(:,1));
com_ref_y = mean(refcent(:,2));
DTr = delaunayTriangulation(refcent);
centspotloc = nearestNeighbor(DTr,[com_ref_x com_ref_y]);

%% 3a. Find spots within grid points

% Move grid to be centered on previously-identified center spot

v_row = v_row + refcent(centspotloc,1);
v_col = v_col + refcent(centspotloc,2);

[VROW, VCOL] = meshgrid(v_row,v_col);
grid_flat_row = reshape(VROW,1,num_grid_across*num_grid_across);
grid_flat_col = reshape(VCOL,1,num_grid_across*num_grid_across);

% Perform FastPeakFind in regions of gridpoints to find centroid ...
    locations
% of spots within grid
% Also do sanity check plot on where the spotfield is being cropped

% figure
% ha = tight_subplot(27,27,[0.001 0.001],0.001,[0.001 0.001]);
clim = [0 63];
```

```
for hoo = 1:num_grid_across^2
    rowstart = floor(grid_flat_row(hoo)-l2p/2);
    colstart = floor(grid_flat_col(hoo)-l2p/2);
    gridcrop(:,:,hoo) = avgref(colstart:colstart + ...
       ceil(l2p),rowstart:rowstart+ceil(l2p));
    peaks = FastPeakFind(uint16(gridcrop(:,:,hoo)),scale,4,0,2);

    %          axes(ha(index));
    %          h1 = imagesc(gridcrop(:,:,foo));
    %          hold on
    %          if not(isempty(peaks))
    %              plot(peaks(1),peaks(2),'bs')
    %          end
    %          hold off
    % %          set(h1,'alphadata',(~isnan(scaled_phase(:,:,index))));
    %          caxis(clim)
    %          colormap(gray)
    %          axis equal
    %          axis off

    if isempty(peaks)
        spotcent_row(hoo) = NaN;
        spotcent_col(hoo) = NaN;
        peakvector(hoo,:) = [NaN NaN];
    else
        spotcent_row(hoo) = (rowstart-1) + peaks(1);
        spotcent_col(hoo) = (colstart-1) + peaks(2);
        peakvector(hoo,:) = [peaks(1) peaks(2)];
    end
end

% Overlay grid on top of spotfield

%% 3b. Rotate image to keep grid straight to start with (can't ...
   correct rotation with mirror)
```

```
% Vector of spot centroids is in pixel units. Want origin to be at ...
    center
% of grid to get correct rotation.
spotcent_row_rot = spotcent_row - refcent(centspotloc,1);
spotcent_row_rot = ...
    reshape(spotcent_row_rot,num_grid_across,num_grid_across);
spotcent_row_rot = ...
    spotcent_row_rot(7:num_grid_across-5,7:num_grid_across-5);
spotcent_row_rot = reshape(spotcent_row_rot,1,(num_grid_across-11)^2);
spotcent_col_rot = spotcent_col - refcent(centspotloc,2);
spotcent_col_rot = ...
    reshape(spotcent_col_rot,num_grid_across,num_grid_across);
spotcent_col_rot = ...
    spotcent_col_rot(7:num_grid_across-5,7:num_grid_across-5);
spotcent_col_rot = reshape(spotcent_col_rot,1,(num_grid_across-11)^2);

% Do the same thing with inital grid.

grid_flat_row_rot = grid_flat_row - refcent(centspotloc,1);
grid_flat_row_rot = ...
    reshape(grid_flat_row_rot,num_grid_across,num_grid_across);
grid_flat_row_rot = ...
    grid_flat_row_rot(7:num_grid_across-5,7:num_grid_across-5);
grid_flat_row_rot = reshape(grid_flat_row_rot,1,(num_grid_across-11)^2);
grid_flat_col_rot = grid_flat_col - refcent(centspotloc,2);
grid_flat_col_rot = ...
    reshape(grid_flat_col_rot,num_grid_across,num_grid_across);
grid_flat_col_rot = ...
    grid_flat_col_rot(7:num_grid_across-5,7:num_grid_across-5);
grid_flat_col_rot = reshape(grid_flat_col_rot,1,(num_grid_across-11)^2);

% Now use rotation matrix and least squares solve to figure out most ...
    likely
% rotation. R = [cosTheta -sinTheta; sinTheta cosTheta]

x_model = vertcat(spotcent_col_rot,spotcent_row_rot);
```

```
nanmodel = isnan(x_model);
x_meas = vertcat(grid_flat_col_rot,grid_flat_row_rot);
nanmeas = isnan(x_meas);
x_model(:,or(nanmodel(1,:),nanmeas(1,:))) = [];
x_meas(:,or(nanmodel(1,:),nanmeas(1,:))) = [];

R = (x_meas')\(x_model');

theta = mean([asind(abs(R(1,2))),asind(abs(R(2,1)))]);
rotatedimage = imrotate(avgref,-theta);
figure
imagesc(rotatedimage)

%-------------------------------------------------------------------------
%% 4. Re-do spot finding for rotated image

intensity_std = std(std(double(rotatedimage)));
scale_rot = intensity_avg + 5*intensity_std; %for spots, want pixels ...
    where intensity is at least 4 stddev above background

% Compute physical center of spotfield (nonweighted average of centroid
% locations) and identify the spot closest to the center
[refcent_rot statsref] = Ref_Spotfield(rotatedimage);
com_ref_x_rot = mean(refcent_rot(:,1));
com_ref_y_rot = mean(refcent_rot(:,2));
DTr = delaunayTriangulation(refcent_rot);
centspotloc_rot = nearestNeighbor(DTr,[com_ref_x_rot com_ref_y_rot]);

% Find spots within grid points

% Move grid to be centered on previously-identified center spot

v_row = v_row - refcent(centspotloc,1) + refcent_rot(centspotloc_rot,1);
v_col = v_col - refcent(centspotloc,2) + refcent_rot(centspotloc_rot,2);

[VROW, VCOL] = meshgrid(v_row,v_col);
```

```
grid_flat_row = reshape(VROW,1,num_grid_across*num_grid_across);
grid_flat_col = reshape(VCOL,1,num_grid_across*num_grid_across);

% Perform FastPeakFind in regions of gridpoints to find centroid ...
    locations
% of spots within grid
% Also do sanity check plot on where the spotfield is being cropped

% figure
% ha = tight_subplot(27,27,[0.001 0.001],0.001,[0.001 0.001]);
clim = [0 63];
for hoo = 1:num_grid_across^2
    rowstart = floor(grid_flat_row(hoo)-l2p/2);
    colstart = floor(grid_flat_col(hoo)-l2p/2);
    gridcrop_rot(:,:,hoo) = rotatedimage(colstart:colstart + ...
        ceil(l2p),rowstart:rowstart+ceil(l2p));
%     gridcrop_rot(:,:,hoo) = rotatedimage(rowstart:rowstart + ...
    ceil(l2p),colstart:colstart+ceil(l2p));

    peaks = FastPeakFind(uint16(gridcrop_rot(:,:,hoo)),scale_rot,4,0,2);

    %          axes(ha(index));
    %          h1 = imagesc(gridcrop(:,:,foo));
    %          hold on
    %          if not(isempty(peaks))
    %              plot(peaks(1),peaks(2),'bs')
    %          end
    %          hold off
    % %          set(h1,'alphadata',(~isnan(scaled_phase(:,:,index))));
    %          caxis(clim)
    %          colormap(gray)
    %          axis equal
    %          axis off

    if isempty(peaks)
        spotcent_row_rot(hoo) = NaN;
```

```
        spotcent_col_rot(hoo) = NaN;
        peakvector(hoo,:) = [NaN NaN];
    else
        spotcent_row_rot(hoo) = (rowstart-1) + peaks(1);
        spotcent_col_rot(hoo) = (colstart-1) + peaks(2);
        peakvector(hoo,:) = [peaks(1) peaks(2)];
    end
end

% ...
    ------------------------------------------------------------------------
%% 5. Poke an actuator, read in and Rotate Measured Spot Image

influence_matrix = zeros(2*(num_grid_across^2),32);
mapping_ID = 1; %Check Boston Micromachines book for info on this value
[error_code, driver_info] = OPEN_miniDM(mapping_ID); %opens ...
    communication with DM

% Find spots within grid points

% TODO: Implement section within lines to allow algorithm to work ...
    even if
% spotfield moves around the detector
% - Calculate center of spotfield, set grid, and find centroids just ...
    as in
% reference case
% - Calculate centroid motion from reference to measure
% - Calculate individual centroid motion from normalized grid location

% Perform FastPeakFind in regions of gridpoints to find centroid ...
    locations
% of spots within grid
% Also do sanity check plot on where the spotfield is being cropped

act = 1;
```

```
for ind = 1:36

    value = stroke;
    newz = ones(36,1)*0;
    newz(ind) = value;
    UPDATE_miniDM(driver_info,newz); %Sets the array values to the DM

    avgmeas = GRAB_FRAME_TL_DCx_64bit(camera_handle,camera_frame);
    avgmeas = avgmeas';
    avgmeas = imrotate(avgmeas,theta);

    clim = [0 63];
    for hoo = 1:num_grid_across^2
        rowstartmeas = floor(grid_flat_row(hoo)-l2p/2);
        colstartmeas = floor(grid_flat_col(hoo)-l2p/2);
        gridcropmeas(:,:,hoo) = avgmeas(colstartmeas:colstartmeas + ...
            ceil(l2p),rowstartmeas:rowstartmeas+ceil(l2p));
        %     gridcrop(:,:,hoo) = avgmeas(rowstart:rowstart + ...
            ceil(l2p),colstart:colstart+ceil(l2p));

        peaksmeas = ...
            FastPeakFind(uint16(gridcropmeas(:,:,hoo)),scale,4,0,2);

        %         axes(ha(index));
        %         h1 = imagesc(gridcrop(:,:,foo));
        %         hold on
        %         if not(isempty(peaks))
        %             plot(peaks(1),peaks(2),'bs')
        %         end
        %         hold off
        % %           ...
            set(h1,'alphadata',(~isnan(scaled_phase(:,:,index))));
        %         caxis(clim)
        %         colormap(gray)
        %         axis equal
        %         axis off
```

```
    if isempty(peaksmeas)
        spotcent_rowmeas(hoo) = NaN;
        spotcent_colmeas(hoo) = NaN;
        peakvectormeas(hoo,:) = [NaN NaN];
    else
        spotcent_rowmeas(hoo) = (rowstartmeas-1) + peaksmeas(1);
        spotcent_colmeas(hoo) = (colstartmeas-1) + peaksmeas(2);
        peakvectormeas(hoo,:) = [peaksmeas(1) peaksmeas(2)];
    end
end

% Plot with grid overlaid on spotfield

% figure
% imagesc(avgmeas);
% colormap(gray)
% colorbar('vert')
% hold on;
% for foo = 1:num_grid_across
%     rowstartmeas = v_row(foo) - 12p/2;
%     for goo = 1:num_grid_across
%         colstartmeas = v_col(goo) - 12p/2;
%         rectangle('position', [rowstartmeas, colstartmeas, ...
   12p, 12p],'EdgeColor','r');
%     end
% end
% plot(spotcent_rowmeas,spotcent_colmeas,'bs')
% hold off
% axis equal tight
% set(gca,'YDir','normal')
% title('Measured Spotfield with Grid (red) and Centroids ...
    (blue)','Fontsize',16)


%% 6. Generate x-y displacement vectors:
```

```
% X-direction: column motion
% Y-direction: row motion
%It's unclear which is supposed to be x and which is supposed to ...
   be y.

Δx_ref = spotcent_rowmeas - spotcent_row_rot; % Compare measured ...
   to reference
% (unactuated mirror)
Δy_ref = spotcent_colmeas - spotcent_col_rot; % Compare measured ...
   to reference
% (unactuated mirror)

Δx_th = spotcent_rowmeas - grid_flat_row; % Compare measured to flat
Δy_th = spotcent_colmeas - grid_flat_col; % Compare measured to flat

Δx_rot = spotcent_row_rot - grid_flat_row;
Δy_rot = spotcent_col_rot - grid_flat_col;

Δx_unrot = spotcent_row - grid_flat_row;
Δy_unrot = spotcent_col - grid_flat_col;

% Generate quiver plot based on this information. Use original ...
   location of
% spots as points and Δx/Δy as vectors

figure
hold on
imagesc(avgmeas)
colormap(gray)
colorbar('vert')
quiver(spotcent_row_rot,spotcent_col_rot,Δx_ref,Δy_ref,0.5,'c','filled','LineWidth',
hold off
axis equal tight
set(gca,'YDir','normal')
```

```
    title('Spot Movement Superimposed on Reference ...
        Spotfield','Fontsize',16)


    dzdx = atan(Δx_th./lenslet_f);
    % dzdx = reshape(dzdx,num_grid_across,num_grid_across);
    dzdy = atan(Δy_th./lenslet_f);
    % dzdy = reshape(dzdy,num_grid_across,num_grid_across);

    if not(ind == any([1,6,31,36]))
        influence_matrix(:,act) = vertcat(Δx_ref',Δy_ref');
        act = act + 1;
    end

end

UPDATE_miniDM(driver_info,zeros(36,1));%Flattens mirror before ...
   closing it
error_code = CLOSE_miniDM(driver_info); %Ends communication with DM
CLOSE_CAMERA_TL_DCx_64bit(camera_handle,camera_frame);
```

A.3.2 Closed-Loop Operation

```
%%%%%%%%%%%%%%%%%%%%%%%%%%%%%%%%%%%%%%%%%%%%%%%%%%%%%%%%
% File: DM_control_script
% Made by: Annie Marinan
% Last modified: 01/28/2016
%
% Description:  This script is a function-free version of the
% DM_control_main code that was difficult to debug
%               Steps involved: (1) Define System Variables
%                               (2) Set 'grid' geometry
%                               (3) Read in reference spots to find
%                               centroid
```

```
%                                   (3a) Find centroid locations of ...
    reference
%                                   spots by gridpoint
%                                   (3b) Calculate rotation offset
%                                   (4) Repeat Steps 3-3a for rotated image
%                                   (unactuated mirror)
%                                   (5) Read in Δ spot measurement and find
%                                   centroid locations by gridpoint
%                                   (6) Compute dx and dy vectors
%                                   (7) Read in interaction matrix
%                                   (8) Calculate Reconstruction matrix and
%                                   solve for mirror deflections
%                                   (9) Scale and covert mirror ...
    deflections to
%                                   voltages
%
% Required Functions: FastPeakFind - reference centroid list
%                     Ref_Spotfield - find all spots
%                     OPEN_CAMERA_TL_DCx_64bit.mex
%                     CLOSE_CAMERA_TL_DCx_64bit.mex
%                     GRAB_FRAME_TL_DCx_64bit.mex
%                     SET_PIXCLK_EXPTIME_FPS_TL_DCx_64bit.mex
%                     OPEN_Mini_DM.mex
%                     UPDATE_Mini_DM.mex
%                     CLOSE_Mini_DM.mex
%%%%%%%%%%%%%%%%%%%%%%%%%%%%%%%%%%%%%%%%%%%%%%%%%%%%%%%%%%%%%%%%%%%%%%%%%%%%

clear all;
close all;
set(0,'DefaultFigureWindowStyle','docked');

% function [dzdx dzdy] = DM_control_script(file)


%% 1. Define physical system parameters (SI units)
```

```
% Misc System Stuff
max_rms_error = 0.05; % um
system_mag = 2; %magnification of the system between the mirror and LA
lambda = 635e-3; % um, wavelength of laser

% Mirror
mirror_d = 1500; % um, or 1.5 mm mirror diameter
actuator_pitch = 300; % um, mirror actuator pitch

% Lenslet Array (LA)
lenslet_pitch = 150; % um lenslet pitch
lenslet_f = 6700; % um lenslet individual focal length

% Detector
pixel_pitch = 5.2; %um pixel pitch
det_x = 1280; % number of pixels in x-dimension (Matlab columns)
det_y = 1024; % number of pixels in y-dimension (Matlab rows)

% Control Loop Parameters
k_1 = 0.02;
k_0 = 0.5;


%% 2. Generate the 'grid' of system-defined boxes on the detector

% Determine number of grid points across (assuming beam circumscribes
% mirror)

num_grid_across = floor(mirror_d*system_mag*sqrt(2)/lenslet_pitch);
if mod(num_grid_across,2) == 0
    num_grid_across = num_grid_across - 1;
end

% Define x- and y- vectors of grid centroids
n = floor(num_grid_across/2);
l2p = lenslet_pitch/pixel_pitch;
```

```
v_row = (-n*l2p):(l2p):(n*l2p);
v_col = v_row;

%% 3. Read in reference spot image and find centroid

% This only happens once.

[camera_handle, camera_frame] = OPEN_CAMERA_TL_DCx_64bit;
SET_PIXCLK_EXPTIME_FPS_TL_DCx_64bit(camera_handle,5,0,10);
avgref = GRAB_FRAME_TL_DCx_64bit(camera_handle,camera_frame);
avgref = avgref';

% avgref = rgb2gray(imread('Flat_1.tif'));
intensity_avg = mean(mean(avgref));
intensity_std = std(std(double(avgref)));
scale = intensity_avg + 5*intensity_std; %for spots, want pixels ...
    where intensity is at least 4 stddev above background

% Compute physical center of spotfield (nonweighted average of centroid
% locations) and identify the spot closest to the center
[refcent statsref] = Ref_Spotfield(avgref);
com_ref_x = mean(refcent(:,1));
com_ref_y = mean(refcent(:,2));
DTr = delaunayTriangulation(refcent);
centspotloc = nearestNeighbor(DTr,[com_ref_x com_ref_y]);

%% 3a. Find spots within grid points

% Move grid to be centered on previously-identified center spot

v_row = v_row + refcent(centspotloc,1);
v_col = v_col + refcent(centspotloc,2);

[VROW, VCOL] = meshgrid(v_row,v_col);
grid_flat_row = reshape(VROW,1,27*27);
grid_flat_col = reshape(VCOL,1,27*27);
```

```
% Perform FastPeakFind in regions of gridpoints to find centroid ...
   locations
% of spots within grid
% Also do sanity check plot on where the spotfield is being cropped

% figure
% ha = tight_subplot(27,27,[0.001 0.001],0.001,[0.001 0.001]);
clim = [0 63];
for hoo = 1:num_grid_across^2
    rowstart = floor(grid_flat_row(hoo)-l2p/2);
    colstart = floor(grid_flat_col(hoo)-l2p/2);
    gridcrop(:,:,hoo) = ...
       avgref(rowstart:rowstart+ceil(l2p),colstart:colstart + ...
       ceil(l2p));
    peaks = FastPeakFind(uint16(gridcrop(:,:,hoo)),scale,4,0,2);

    %          axes(ha(index));
    %          h1 = imagesc(gridcrop(:,:,foo));
    %          hold on
    %          if not(isempty(peaks))
    %              plot(peaks(1),peaks(2),'bs')
    %          end
    %          hold off
    % %          set(h1,'alphadata',(~isnan(scaled_phase(:,:,index))));
    %          caxis(clim)
    %          colormap(gray)
    %          axis equal
    %          axis off

    if isempty(peaks)
        spotcent_row(hoo) = NaN;
        spotcent_col(hoo) = NaN;
        peakvector(hoo,:) = [NaN NaN];
    else
        spotcent_row(hoo) = (rowstart-1) + peaks(1);
```

```
        spotcent_col(hoo) = (colstart-1) + peaks(2);
        peakvector(hoo,:) = [peaks(1) peaks(2)];
    end
end

% Overlay grid on top of spotfield

%% 3b. Rotate image to keep grid straight to start with (can't ...
    correct rotation with mirror)

% Vector of spot centroids is in pixel units. Want origin to be at ...
    center
% of grid to get correct rotation.
spotcent_row_rot = spotcent_row - refcent(centspotloc,1);
spotcent_row_rot = ...
    reshape(spotcent_row_rot,num_grid_across,num_grid_across);
spotcent_row_rot = ...
    spotcent_row_rot(11:num_grid_across-10,11:num_grid_across-10);
spotcent_row_rot = reshape(spotcent_row_rot,1,(num_grid_across-20)^2);
spotcent_col_rot = spotcent_col - refcent(centspotloc,2);
spotcent_col_rot = ...
    reshape(spotcent_col_rot,num_grid_across,num_grid_across);
spotcent_col_rot = ...
    spotcent_col_rot(11:num_grid_across-10,11:num_grid_across-10);
spotcent_col_rot = reshape(spotcent_col_rot,1,(num_grid_across-20)^2);

% Do the same thing with inital grid.

grid_flat_row_rot = grid_flat_row - refcent(centspotloc,1);
grid_flat_row_rot = ...
    reshape(grid_flat_row_rot,num_grid_across,num_grid_across);
grid_flat_row_rot = ...
    grid_flat_row_rot(11:num_grid_across-10,11:num_grid_across-10);
grid_flat_row_rot = reshape(grid_flat_row_rot,1,(num_grid_across-20)^2);
grid_flat_col_rot = grid_flat_col - refcent(centspotloc,2);
```

```
grid_flat_col_rot = ...
    reshape(grid_flat_col_rot,num_grid_across,num_grid_across);
grid_flat_col_rot = ...
    grid_flat_col_rot(11:num_grid_across-10,11:num_grid_across-10);
grid_flat_col_rot = reshape(grid_flat_col_rot,1,(num_grid_across-20)^2);

% Now use rotation matrix and least squares solve to figure out most ...
    likely
% rotation. R = [cosTheta -sinTheta; sinTheta cosTheta]

x_model = vertcat(spotcent_col_rot,spotcent_row_rot);
x_meas = vertcat(grid_flat_col_rot,grid_flat_row_rot);

R = (x_meas')\(x_model');

theta = mean([asind(abs(R(1,2))),asind(abs(R(2,1)))]);
rotatedimage = imrotate(avgref,-theta);
figure(1)
imagesc(rotatedimage)

%-------------------------------------------------------------------------
%% 4. Re-do spot finding for rotated/scaled image

% This becomes u_1.

intensity_std = std(std(double(rotatedimage)));
scale_rot = intensity_avg + 5*intensity_std; %for spots, want pixels ...
    where intensity is at least 4 stddev above background

% Compute physical center of spotfield (nonweighted average of centroid
% locations) and identify the spot closest to the center
[refcent_rot statsref] = Ref_Spotfield(rotatedimage);
com_ref_x_rot = mean(refcent_rot(:,1));
com_ref_y_rot = mean(refcent_rot(:,2));
DTr = delaunayTriangulation(refcent_rot);
centspotloc_rot = nearestNeighbor(DTr,[com_ref_x_rot com_ref_y_rot]);
```

```
% Find spots within grid points

% Move grid to be centered on previously-identified center spot

v_row = v_row - refcent(centspotloc,1) + refcent_rot(centspotloc_rot,1);
v_col = v_col - refcent(centspotloc,2) + refcent_rot(centspotloc_rot,2);

[VROW, VCOL] = meshgrid(v_row,v_col);
grid_flat_row = reshape(VROW,1,27*27);
grid_flat_col = reshape(VCOL,1,27*27);

% ...
    ------------------------------------------------------------------------
%% 5. Initiate Control Loop

% This is where the control loop starts.

% Read in interaction matrix A
pokeinfo = load('BMC_Pokes_20160126.mat');
nanrow = pokeinfo.row;
A = pokeinfo.pokematrix; %(1458 x 32)
A(nanrow,:) = []; % Ignore gridpoints that yielded no spots
A(isnan(A)) = 0;
B = pinv(A);

b = 0.051260;
a = 0.027707;

u_prev = zeros(1,32);
var = 0;
mapping_ID = 1; %Check Boston Micromachines book for info on this value
[error_code, driver_info] = OPEN_miniDM(mapping_ID); %opens ...
    communication with DM

while var<10
```

```
avgmeas = GRAB_FRAME_TL_DCx_64bit(camera_handle,camera_frame);
avgmeas = avgmeas';

% avgmeas = rgb2gray(imread('Flat_2.tif'));
avgmeas = imrotate(avgmeas,-theta);
% avgmeas = rgb2gray(imread(file));

% Find spots within grid points

% Perform FastPeakFind in regions of gridpoints to find centroid ...
   locations
% of spots within grid
% Also do sanity check plot on where the spotfield is being cropped

% figure
% ha = tight_subplot(27,27,[0.001 0.001],0.001,[0.001 0.001]);
clim = [0 63];
for hoo = 1:num_grid_across^2
    rowstartmeas = floor(grid_flat_row(hoo)-l2p/2);
    colstartmeas = floor(grid_flat_col(hoo)-l2p/2);
    gridcropmeas(:,:,hoo) = avgmeas(colstartmeas:colstartmeas + ...
       ceil(l2p),rowstartmeas:rowstartmeas+ceil(l2p));
    peaksmeas = ...
       FastPeakFind(uint16(gridcropmeas(:,:,hoo)),scale,4,0,2);

    if isempty(peaksmeas)
        spotcent_rowmeas(hoo) = NaN;
        spotcent_colmeas(hoo) = NaN;
        peakvectormeas(hoo,:) = [NaN NaN];
    else
        spotcent_rowmeas(hoo) = (rowstartmeas-1) + peaksmeas(1);
        spotcent_colmeas(hoo) = (colstartmeas-1) + peaksmeas(2);
        peakvectormeas(hoo,:) = [peaksmeas(1) peaksmeas(2)];
    end
end
```

```
    % Plot with grid overlaid on spotfield

%     figure(2)
%     imagesc(avgmeas);
%     colormap(gray)
%     colorbar('vert')
%     hold on;
%     for foo = 1:num_grid_across
%         rowstartmeas = v_row(foo) - 12p/2;
%         for goo = 1:num_grid_across
%             colstartmeas = v_col(goo) - 12p/2;
%             rectangle('position', [rowstartmeas, colstartmeas, ...
    12p, 12p],'EdgeColor','r');
%         end
%     end
%     plot(spotcent_rowmeas,spotcent_colmeas,'bs')
%     hold off
%     axis equal tight
%     set(gca,'YDir','normal')
%     title('Measured Spotfield with Grid (red) and Centroids ...
    (blue)','Fontsize',16)


    %% 6. Generate x-y displacement vectors:

    % X-direction: column motion
    % Y-direction: row motion
    % It's unclear which is supposed to be x and which is supposed ...
       to be y.

    Δx_th = spotcent_rowmeas - grid_flat_row; % Compare measured to flat
    Δy_th = spotcent_colmeas - grid_flat_col; % Compare measured to flat

    figure(2)
    subplot(1,3,1)
```

```
    hold on
    imagesc(avgmeas)
    colormap(gray)
    colorbar('vert')
    quiver(grid_flat_row,grid_flat_col,Δx_th,Δy_th,0.5,'c','filled','LineWidth',2)
    hold off
    axis equal tight
    set(gca,'YDir','normal')
    title('Spot Movement Superimposed on Grid','Fontsize',16)
    refreshdata;
    drawnow;

    %Uncomment the section between lines for de-bugging rotation.
    % ------------------------------------------------------------

%     Δx_ref = spotcent_rowmeas - spotcent_row_rot; % Compare ...
    measured to reference
%     (unactuated mirror)
%     Δy_ref = spotcent_colmeas - spotcent_col_rot; % Compare ...
    measured to reference
%     (unactuated mirror)
%     Δx_rot = spotcent_row_rot - grid_flat_row;
%     Δy_rot = spotcent_col_rot - grid_flat_col;
%     Δx_unrot = spotcent_row - grid_flat_row;
%     Δy_unrot = spotcent_col - grid_flat_col;
%
%     Generate quiver plot based on this information. Use original ...
    location of
%     spots as points and Δx/Δy as vectors
%
%     figure
%     hold on
%     imagesc(avgmeas)
%     colormap(gray)
%     colorbar('vert')
```

```
%     ...
    quiver(spotcent_row_rot,spotcent_col_rot,Δx_ref,Δy_ref,0.5,'c','filled','LineWidth',
%     hold off
%     axis equal tight
%     set(gca,'YDir','normal')
%     title('Spot Movement Superimposed on Reference ...
    Spotfield','Fontsize',16)
%
%     figure
%     hold on
%     imagesc(avgmeas)
%     colormap(gray)
%     colorbar('vert')
%     ...
    quiver(grid_flat_row,grid_flat_col,Δx_rot,Δy_rot,0.5,'c','filled','LineWidth',2)
%     hold off
%     axis equal tight
%     set(gca,'YDir','normal')
%     title('Rotated Reference Spot Deltas','Fontsize',16)
%
%     figure
%     hold on
%     imagesc(avgmeas)
%     colormap(gray)
%     colorbar('vert')
%     ...
    quiver(grid_flat_row,grid_flat_col,Δx_unrot,Δy_unrot,0.5,'c','filled','LineWidth',2)
%     hold off
%     axis equal tight
%     set(gca,'YDir','normal')
%     title('UnRotated Reference Spot Deltas','Fontsize',16)
%
     % ...
       ------------------------------------------------------------------------
```

```
% Convert Δx and Δy vectors to dz/dx and dz/dy based on lenslet
% properties

dzdx = -atan(Δx_th./lenslet_f);
% dzdx = reshape(dzdx,num_grid_across,num_grid_across);
dzdy = -atan(Δy_th./lenslet_f);
% dzdy = reshape(dzdy,num_grid_across,num_grid_across);


%% 7. Control Implementation: Read in the Interaction Matrix A

c = horzcat(dzdx,dzdy);
c = c'; % (1 x 1458)
c(nanrow,:) = [];
c(isnan(c)) = 0;

%% 8. Create Reconstructor Matrix B

% B is just the inverse of A multiplied by a scaling factor for ...
   piston
% and/or intensity normalization

% TODO: Create loop that goes through actuations and makes this ...
   a feedback
% system

u_cmd = (1-k_l)*u_prev + (k_0*B*c)';
% u is in actuator space in units of percentage of actuator ...
   stroke (?)

%% 9. Scale and apply actuator curve to the mirror shape before ...
   commanding

% Because it gets input as a 36-element vector with zeros at 1, ...
   6, 31, 36
```

```
act_vector = u_cmd;

% Offset actuations to get rid of negative actuations

act_vector = act_vector - min(act_vector);

% Scale actuations to fall within mirror stroke range (1.5 um)

act_vector = act_vector/(max(abs(act_vector)))*1.5;

% Convert to Voltage commands
% mirror_command is in microns, want it in Volts to send to mirror
% nm deflection = 0.027707*V^2 - 0.051260*V;
% V = (0.051260 + sqrt(0.051260^2 + 4*0.027707*(nm ...
    def)))/(2*0.027707)

act_vector_V = (b + sqrt(b^2 + 4.*a.*(act_vector*1000)))./(2*a);

mirror_shape = zeros(1,36);
mirror_shape(2:5) = act_vector(1:4);
mirror_shape(7:30) = act_vector(5:28);
mirror_shape(32:35) = act_vector(29:32);

mirror_command = zeros(36,1);
mirror_command(2:5) = act_vector_V(1:4);
mirror_command(7:30) = act_vector_V(5:28);
mirror_command(32:35) = act_vector_V(29:32);

mirrormap_V = reshape(mirror_command,6,6);
mirrormap_um = reshape(mirror_shape,6,6);

figure(2)
subplot(1,3,2)
h_V=bar3(mirrormap_V);
% For each barseries, map its CData to its ZData
for i = 1:length(h_V)
```

```
    zdata = get(h_V(i),'ZData');
    set(h_V(i),'CData',zdata)
    % Add back edge color removed by interpolating shading
end
% Tell handle graphics to use interpolated rather than flat shading
colormap(jet);
shading interp
set(h_V,'EdgeColor','k')
colorbar;
xlabel('Actuator (#)')
ylabel('Actuator (#)')
zlabel('Mirror Position (V))')
title('Commanded Mirror Shape in V','Fontsize',16)
refreshdata;
drawnow;

figure(2)
subplot(1,3,3)
h_um=bar3(mirrormap_um);
% For each barseries, map its CData to its ZData
for i = 1:length(h_um)
    zdata = get(h_um(i),'ZData');
    set(h_um(i),'CData',zdata)
    % Add back edge color removed by interpolating shading
end
% Tell handle graphics to use interpolated rather than flat shading
colormap(jet);
shading interp
set(h_um,'EdgeColor','k')
colorbar;
xlabel('Actuator (#)')
ylabel('Actuator (#)')
zlabel('Mirror Position (um))')
title('Commanded Mirror Shape in um','Fontsize',16)
refreshdata;
drawnow;
```

```
    %% Command shape to mirror


    mirror_command = mirror_command/250*0.95*100;
    UPDATE_miniDM(driver_info,mirror_command);

    var = var + 1;
    u_prev = u_cmd;

end

%Close everything

newimage = GRAB_FRAME_TL_DCx_64bit(camera_handle,camera_frame);

UPDATE_miniDM(driver_info,zeros(36,1));%Flattens mirror before ...
    closing it
error_code = CLOSE_miniDM(driver_info); %Ends communication with DM
CLOSE_CAMERA_TL_DCx_64bit(camera_handle,camera_frame);
```

Bibliography

[1] H. Heidt, J. Puig-Suari, A. Moore, S. Nakasuka, and R. Twiggs, "Cubesat: A New Generation of Picosatellite for Education and Industry Low-Cost Space Experimentation," in *SSC00-V-5*, Logan, UT, 2001.

[2] K. Woellert, P. Ehrenfreund, A. Ricco, and H. Hertzfeld, "Cubesats: Cost-effective science and technology platforms for emerging and developing nations," *Advances in Space Research*, vol. 47, pp. 663–684, 2011.

[3] Committee on Earth Science and Applications from Space, *Earth Science and Applications from Space: National Imperatives for the Next Decade and Beyond*, English, 2007.

[4] M.M. Burlacu and P. Lorenz, "A survey of small satellites domain challenges, applications, and communications issues," *ICaST: ICST's Global Community Magazine*, 2010.

[5] A. Petro, *Small spacecraft technology*, 2012. [Online]. Available: `http://www.nasa.gov/offices/oct/crosscutting_capability/edison/smallsat_tech.html`.

[6] Saint Louis University, *CubeSat Database*. [Online]. Available: `http://sites.google.com/a/slu.edu/swartwout/home/cubesat-database` (visited on 11/21/2015).

[7] M. Swartwout, "The First One Hundred CubeSats: A Statistical Look," *Journal of Small Satellites*, vol. 2, no. 2, pp. 213–233, 2013.

[8] E. Hand, "Startup Liftoff: How flocks of small, cheap satellites, hatched in Silicon Valley, will constantly monitor a changing Earth," *Science*, pp. 172–177, Apr. 2015.

[9] Anna Heiney and Brian Dunbar, *About ELaNa: Project ELaNa: Launching Education into Space*, 2015. [Online]. Available: `https://www.nasa.gov/content/about-elana`.

[10] M. D. D. Staff, *Small Spacecraft Technology State of the Art*, 2014.

[11] J. Foust, "Spire Raises $40 Million for Weather Satellite Constellation," Jun. 2015. [Online]. Available: `http://spacenews.com/spire-raises-40-million-for-weather-satellite-constellation..`

[12] Arash Mehrparvar, David Pignatelli, Justin Carnahan, Riki Munakate, Wenschel Lan, Armen Toorian, Amy Hutputanasin, and Simon Lee, "Cubesat design specification," The CubeSat Program: California Polytechnic State University, Tech. Rep., 2014.

[13] D. Selva and D. Krejci, "Review: A Survey and Assessment of the Capabilities of Cubesats for Earth Observation," *Acta Astronautica*, vol. 74, pp. 50–68, Nov. 2012.

[14] K. Tomisayu, "Remote sensing of the earth by microwaves," in *Proceedings of the IEEE*, vol. 6, 1974.

[15] William Blackwell, "Micromas: First Step Towards a Nanosatellite Constellation for Global Storm Observation," in *Proceedings of the 27th Annual AIAA/USU Conference on Small Satellites*, Logan, UT, Aug. 2013.

[16] S. Schweitzer, G. Kirchengast, and V. Proschek, "Atmospheric influences on infrared-laser signals used for occultation measurements between Low Earth Orbit satellites," *Atmospheric Measurement Techniques*, vol. 4, pp. 2273–2292, 2011. DOI: 10.5194/amt-4-2273-2011.

[17] X. Zou, L. Lin, and F. Weng, "Absolute calibration of ATMS upper level temperature sounding channels using GPS RO observations," *IEEE Trans. Geo. Remote Sensing*, vol. 52, no. 2, pp. 1397–1406, 2014.

[18] AMSU-A, *Eumetsat: Monitoring weather and climate from space.* [Online]. Available: http://www.eumetsat.int/website/home/Satellites/CurrentSatellites/Metop/MetopDesign/AMSUA/index.html.

[19] MHS, *Eumetsat: Monitoring weather and climate from space.* [Online]. Available: http://www.eumetsat.int/website/home/Satellites/CurrentSatellites/Metop/MetopDesign/MHS/index.html.

[20] *Polar-Orbiting Satellites: With costs increasing and data continuity at risk, improvements needed in a tri-agency decision making*, 2009.

[21] W. J. Blackwell and J. Pereira, "New Small Satellite Capabilities for Microwave Atmospheric Remote Sensing: The Earth Observing Nanosatellite-Microwave (EON-MW)," in *Proceedings of the 29th Annual AIAA/USU Conference on Small Satellites*, Logan, UT, 2015.

[22] M. R. Schoeberl, A. R. Douglass, E. Hilsenrath, P. K. Bhartia, R. Beer, J. W. Waters, M. R. Gunson, L. Froidevaux, J. C. Gille, J. J. Barnett, P. F. Levelt, and P. DeCola, "Overview of the eos aura mission," *IEEE Transactions on Geoscience and Remote Sensing*, vol. 44, no. 5, pp. 1066–1074, 2006.

[23] N. R. Council, *Path, precipitation and all-weather temperature and humidity*, Washington, DC, 2008. DOI: 10.17226/11952.

[24] ——, *Gacm, global atmospheric composition mission*, Washington, DC, 2008. DOI: 10.17226/11952.

[25] G. Kirchengast, *Occultations for Probing Atmosphere and Climate*, G. Kirchengast, U. Foelsche, and A. K. Steiner, Eds. Berlin, Heidelberg: Springer Berlin Heidelberg, 2004, ch. Occultations for Probing Atmosphere and Climate: Setting the Scene, pp. 1–8, ISBN: 978-3-662-09041-1. DOI: 10.1007/978-3-662-09041-1_1. [Online]. Available: http://dx.doi.org/10.1007/978-3-662-09041-1_1.

[26] Christian Rocken, Ying-Hwa Kuo, Sergey Sokolovskiy, and Richard Anthes, *The ROCSAT-3/COSMIC Mission and Applications of GPS Radio Occultation Data to Weather and Climate.*

[27] E. Robert Kursinski, "The GPS Radio Occultation Concept: Theoretical Performance and Initial Results," English, Doctor of Philosophy, California Institute of Technology, Pasadena, CA, Mar. 1997.

[28] O. Montenbruck, *GNSS Receivers for Space Applications*, TU Munchen, May 2008.

[29] *Halogen occultation experiment.* [Online]. Available: http://haloe.gats-inc.com/about/index.php.

[30] "Atmospheric chemistry experiment (ace): Mission overview," *Geophysical Research Letters*, vol. 32, 2005.

[31] L. L. Gordley, M. E. Hervig, C. Fish, J. M. Russell III, S. Bailey, J. Cook, S. Hansen, A. Shumway, G. Paxton, L. Deaver, T Marshall, J. Burton, B. Magill, C. Brown, E. Thompson, and J. Kemp, "The solar occultation for ice experiment," *Journal of Atmospheric and Solar-Terrestrial Physics*, vol. 71, pp. 300–315, 2009.

[32] R. Furrer, H. Rubin, M. Schaale, A. V. Poberovsky, A. V. Mironenkov, and Y. M. Timofeyev, "Miriam - a space-borne sun occultation experiment for atmospheric trace gas spectroscopy," *GeoJournal*, vol. 32, no. 1, pp. 17–27, 1994.

[33] J. P. Burrows, E. Holzle, A. P. H. Goede, H. Visser, and W. Fricke, "Schiamachy - scanning imaging absorption spectrometer for atmospheric chartography," *Acta Astronautica*, vol. 35, no. 7, pp. 445–451, 1995.

[34] J. Albert, "Satellite-mounted light sources as photometric calibration standards for ground-based telescopes," *The Astronomical Journal*, vol. 143, no. 8, 2012.

[35] P. Minott, "Design of retrodirector arrays for laser ranging of satellites," NASA Goddard Space Flight Center, Tech. Rep., 1974. DOI: 19740018193.

[36] C. Ting, D.G. Voelz, and M.K. Giles, "Laser satellite communications with adaptive optics," in *Proc. SPIE*, vol. 5892, 2005.

[37] e. a. M. W. Smith, "Exoplanetsat: Detecting transiting exoplanets using a low-cost cubesat platform," in *Proc. SPIE*, vol. 7731.

[38] K. Cahoy, A. Marinan, M. Webber, and C. Kerr, "Cubesat deformable mirror demonstration," in *IEEE Aerospace*, Big Sky, Montana, 2013.

[39] S. Seager, Ed., *Exoplanets*. United States of America: The University of Arizona Press in collaboration with the Lunar and Planetary Institute, 2010.

[40] R. K. Tyson, *PRINCIPLES of Adaptive Optics*. Boca Raton, FL, USA: CRC Press, 2011.

[41] M.Levine and R. Soummer, *Overview of technologies for direct optical imaging of exoplanets*, 2009. [Online]. Available: `http://planetquest.jpl.nasa.gov/TPF-C/TechnologyAstro2010WPVisiblePlanetImagingFinal.pdf`.

[42] M. van Dam, D.L. Mignant, and Bruce Macintosh, "Performance of the keck observatory adaptive-optics system," *Applied Optics*, vol. 43, no. 29, pp. 5458–5467, 2004.

[43] Jennifer Roberts, Antonin Bouchez, Rick Burruss, Richard Dekany, Stephen Guiwits, and Mitchell Troy, "Optical Characterization of the PALM-3000 3388-Actuator Deformable Mirror," 2010. [Online]. Available: `http://www.oir.caltech.edu/twiki_oir/bin/view/Palomar/Palm3000/WebHome`.

[44] D. et al, "Recent science and engineering results with the laser guidestar adaptive optic system at lick observatory," *Proc. SPIE 4839, Adaptive Optical System Technologies II*, no. 354, 2003.

[45] T. Berkefeld and et al, "Adaptive optics for satellite-to-ground laser communication at the 1m telescope of the esa optical ground station, tenerife, spain," in *Proc. of SPIE Adaptive Optics Systems II*, vol. 7736, 2010.

[46] B. A. Macintosh, J. R. Graham, D. W. Palmer, R. Doyon, J. Dunn, D. T. Gavel, J. Larkin, B. Oppenheimer, L. Saddlemyer, A. Sivaramakrishnan, W. J. Kent, B. Bauman, D. A. Erickson, C. Marois, L. A. Poyneer, and R. Soumer, "The gemini planet imager: From science to design to construction," vol. 7015, 2008. DOI: `10.1117/12.788083`. [Online]. Available: `http://dx.doi.org/10.1117/12.788083`.

[47] B. M. et al, "Extreme adaptive optics for the thirty meter telescope," in *SPIE: Advances in Adaptive Optics II*, vol. 6272, 2006.

[48] Christopher Mendillo, Supriya Chakrabarti, Timothy Cook, Brian Hicks, and Benjamin Lane, "Flight Demonstration of a milliarcsecond pointing system for direct exoplanet imaging," *Applied Optics*, vol. 51, no. 29, pp. 7069–7079, Oct. 2012, ISSN: 1559-128X/12/297069-11.

[49] C.B. Mendillo, J. J. Martel, G.A. Howe, K. Hewasawam, S.C. Finn, T.A. Cook, S. Chakrabarti, E.S. Douglas, D. Mawet, O. Guyon, G. J. Lozi, K.L. Cahoy, and A.D. Marinan, "The low-order wavefront sensor for the picture-c mission," vol. 9605, 2015.

[50] J. L. et al, "A new type of space telescope for observation of extreme lightning phenomena in the upper atmosphere," *IEEE Transactions on Geoscience and Remote Sensing*, vol. 50, no. 10, pp. 3941–3949, 2012.

[51] B. Y. et al, "Mems micromirror characterization in space environments," *Optics Express*, vol. 17, pp. 3370–3380, 2009.

[52] J. Trauger, "Access - a science and engineering assessment of space coronagraph concepts for the direct imaging and spectroscopy of exoplanetary systems," in *Beyond JWST Conference, Space Telescope Science Institute*, 2009.

[53] I.Poberezhskiy, F. Zhao, X. An, K. Balasubramanian, R. Belikov, E. Cady, R. Demers, R. Diaz, Q. Gong, B. Gordon, R. Goullioud, F. Greer, O. Guyon, M. Hoenk, N.J. Kasdin, B. Kern, J. Krist, A. Kuhnert, M. McElwain, B. Mennesson, D. Moody, R. Muller, B. Nemati, K. Patterson, A.J. Riggs, D. Ryan, B.J. Seo, S. Shaklan, E. Sidick, F. Shi, N. Siegler, R. Soummer, H. Tang, J. Trauger, J. K. Wallace, X. Wang, V. White, D. Wilson, K. Yee, H. Zhou, and N. Zimmerman, "Technology development towards wfirst-afta coronagraph," vol. 9143, 2014.

[54] Science and Technology Definition Team and Exo-C Design Team, "Exo-c: Imaging nearby worlds, final report," Caltech, Tech. Rep. 15-1197, 2015.

[55] R. B. et al, "Excede techology development i: First demonstrations of high contrast at 1.2 l/d for an explorer space telescope mission," in *Proc. of SPIE*, vol. 8442, 2012.

[56] E. Bendek, R. Belikov, J. Lozi, S. Thomas, J. Males, and S. Weston, "Small satellite mission concept to image earth-like planets around alpha centauri," in *29th Annual AIAA/USU Conference on Small Satellites*, Logan, UT, 2015.

[57] D. Aviv, *LASER Space Communications*. Norwood, MA: Artech House, 2006.

[58] R. Kingsbury, K. Riesing, and K. Cahoy, "Design of a free-space optical communication module for small satellites," in *Proc. of the AIAA/USU Conference on Small Satellites*, vol. SSC14-IX-6, 2014.

[59] C. Pong, "High-precision pointing and attitude estimation and control algorithms for hardware-constrained spacecraft," Doctor of Philosophy, Massachusetts Institute of Technology, 2014.

[60] S. Cole, *Nasa selects instruments to study air pollution, tropical cyclones*, 2016. [Online]. Available: `https://www.nasa.gov/press-release/nasa-selects-instruments-to-study-air-pollution-tropical-cyclones`.

[61] J. Walker, "Continuous whole-earth coverage by circular-orbit satellite patterns," Royal Aircraft Establishment, Farnborough, Hants, UK, Tech. Rep., 1977. DOI: 850100.

[62] E. Hayes, "An algorithm for the computation of coverage area by earth observing satellites," in *AIAA Astrodynamics Conference*, 1986, p. 121.

[63] D. Beste, "Design of satellite constellations for optimal continuous coverage," *IEEE Transactions on Aerospace and Electronic Systems*, vol. AES-14, no. 3, 466–473, 1978.

[64] S. Cornara, T. W. Beech, and M. Bello-Mora, "Satellite constellation mission analysis and design," *Acta Astronautica*, vol. 48, no. 512, 681–691, 2001.

[65] C. Jilla and D. Miller, "Multi-objective, multidisciplinary design optimization methodology for distributed satellite systems," *Journal of Spacecraft and Rockets*, vol. 41, no. 1, 39–50, 2004.

[66] L. A. IV, "Increased fidelity space weather data collection using a non-linear cubesat network," Doctor of Philosophy, University of Southern California, 2009.

[67] A. Ballard, "Rosette constellations of earth satellites," *IEEE Transactions on Aerospace and Electronic Systems*, vol. AES-16, no. 5, 656–673, 1980.

[68] D. J. Pegher and J.A. Parish, "Optimizing coverage and revisit time in sparse military satellite constellations: A comparison of traditional approaches and genetic algorithms," Masters, Naval Postgraduate School, Monterey, CA, 2004.

[69] R. S. Legge, "Optimization and valuation of recongurable satellite constellations under uncertainty," PhD thesis, 2014. [Online]. Available: `http://hdl.handle.net/1721.1/97261`.

[70] A. D. Marinan, A. K. Nicholas, and K. L. Cahoy, "Ad hoc cubesat constellations: Secondary launch coverage and distribution," Big Sky, MO, 2013.

[71] D. H. Staelin, "Measurements and interpretation of the microwave spectrum of the terrestrial atmosphere near 1-centimeter wavelength," *Journal of Geophysical Research*, vol. 71, no. 12, pp. 2875–2881, 1966, ISSN: 2156-2202. DOI: `10.1029/JZ071i012p02875`. [Online]. Available: `http://dx.doi.org/10.1029/JZ071i012p02875`.

[72] L. W. Schaper, D. H. Staelin, and J. W. Waters, "The estimation of tropospheric electrical path length by microwave radiometry," *Proceedings of the IEEE*, vol. 58, no. 2, pp. 272–273, Feb. 1970, ISSN: 0018-9219. DOI: `10.1109/PROC.1970.7616`.

[73] W. J. Blackwell, R. V. Leslie, M. L. Pieper, and J. E. Samra, "Al-weather hyperspectral atmospheric sounding," Lexington, MA, 2, 2010.

[74] *Polarcube: An advanced radiometer 3u cubesat.* [Online]. Available: `http://spacegrant.colorado.edu/allstar-projects/polarcube`.

[75] B. H. Lim, *Radiometer atmospheric cubesat experiment (race)*, 2010. [Online]. Available: `http://phaeton.jpl.nasa.gov/external/projects/race.cfm`.

[76] W. H. Swartz, L. P. Dyrud, S. R. Lorentz, D. L. Wu, W. J. Wiscombe, S. J. Papadakis, P. M. Huang, E. L. Reynolds, A. W. Smith, and D. M. Deglaua, *The ravan cubesat mission: Advancing technologies for climate observation*, Milan, Italy, 2015.

[77] D. L. Wu, J. Esper, N. Ehsan, T. E. Johnson, W. R. Mast, J. R. Piepmeier, and P. E. Racette, *Icecube: Spaceflight validation of an 874-ghz submillimeter wave radiometer for cloud ice remote sensing*, Leesburg, VA, 2014.

[78] e. a. W.J. Blackwell, "Microwave radiometer technology acceleration mission (mirata): Advancing weather remote sensing with nanosatellites," in *Proceedings of the 28th Annual AIAA/USU Conference on Small Satellites*, Logan, UT, 2014.

[79] William Blackwell, Rebecca Bishop, Kerri Cahoy, Brian Cohen, Clayton Crail, Lidia Cucurull, Pratik Dave, Michael DiLiberto, Neal Erickson, Chad Fish, Shu-peng Ho, R. Vincent Leslie, Adam Milstein, and Idahosa Osaretin, "Radiometer Calibration Using Colocated GPS Radio Occultation Measurements," *IEEE Transactions on Geoscience and Remote Sensing*, vol. 52, no. 10, pp. 6423–6433, 2013. DOI: 10.1109/TGRS.2013.2296558.

[80] S. M. Leidner, T. Nehrkorn, J. Henderson, and M/ Mountian, "Severe weather study shows potential of gnss-ro," GeoOptics, Tech. Rep., 2015.

[81] E. Njoku, "Passive microwave remote sensing of the earth from space - a review," in *Proceedings of the IEEE*, vol. 70, 1982.

[82] R. Anthes, "Exploring Earth's atmosphere with radio occultation: Contributions to weather, climate and space weather," *Atmospheric Measurement Techniques Discussions*, vol. 4, pp. 135–212, 2011.

[83] E. Kahr, L. Bradbury, P. G. O'Keefe, and S. Skone, "Design and operation of the gps receiver onboard the canx-2 nanosatellite," *Navigation*, vol. 60, pp. 143–156, 2013.

[84] *SNAP-1: The Mission.* [Online]. Available: http://www.sstl.co.uk/Missions/SNAP-1-Launched-2000/SNAP-1/SNAP-1-The-Mission.

[85] Rebecca Bishop, David Hinkley, Daniel Stoffel, David Ping, Paul Straus, and Timothy Burbaker, "First Results from the GPS Compact Total Electron Content Sensor (CTECS) on the PSSCT-2 Nanosat," Logan, UT, Aug. 2012.

[86] G. Lightsey and T. Humphreys, "Foton: A software-defined, compact, low-cost gps radio occultation sensor," in *GEOScan Planning Workshop*, 2011.

[87] A. Hauschild, M. Markgraf, and O. Montenbruck, "The navigation and occultation experiment gps receiver performance on board a leo satellite," *InsideGNSS*, pp. 48–57, 2014.

[88] N. Inc., *Receivers oem628: Next generation high performance gnss receiver, version 13*, Canada, 2015.

[89] V. Proschek, G. Kirchengast, and S. Schweitzer, "Greenhouse gas profiling by infrared-laser and microwave occultation: Retrieval algorithm and demonstration results from end-to-end simulations," *Atmospheric Measurement Techniques*, vol. 4, pp. 2035–2058, 2011. DOI: 10.5194/amt-4-2035-2011.

[90] S. Mottini, A. Loescher, M. Aguirre, I. Bakalski, and G. Kirchengast, "A new approach to climatology from space: Laser occultation," in *International Conference on Space Optics*, Rhodes, Greece, 2010.

[91] e. a. D. E. Smith, "Two way laser link over interplanetary distance," *Science*, vol. 311, no. 53, p. 5757, 2006.

[92] L. C. Andrews and R. L. Phillips, *Laser Beam Propagation through Random Media, Second Edition.* Bellingham, WA: Society of Photo-Optical Instrumentation Engineers, 2005, ISBN: 9780819459480.

[93] T. T. Nielsen and G. Oppenhauser, "In-orbit test result of an operational optical intersatellite link between artemis and spot4, silex," in *Proc. SPIE*, vol. 4635, 2002.

[94] T. G. Bifano, J. Perreault, R. Krishnamoorthy Mali, and M. N. Horenstein, "Microelectromechanical deformable mirrors," *IEEE Journal of Selected Topics in Quantum Electronics*, vol. 5, no. 1, pp. 83–89, 1999.

[95] Boston Micromachines Corporation, *Mini-dm Specification Sheet*, 2014. [Online]. Available: `http://www.bmc.bostonmicromachines.com/pdf/Mini-DM.pdf`.

[96] S. A. Cornelissen, P. A. Bierden, T. G. Bifano, and C. V. Lam, "4096-element continuous face-sheet mems deformable mirror for high-contrast imaging," *Journal of Micro/Nanolithography, MEMS, and MOEMS*, vol. 8, no. 3, 2009.

[97] A. Diouf, A. P. Legendre, J. B. Stewart, T. G. Bifano, and Y. Lu, "Open-loop shape control for continuous microelectromechanical system deformable mirror," *Appl. Opt.*, vol. 49, no. 31, G148–G154, 2010.

[98] B. R. Oppenheimer and S. Hinkley, "High-contrast observations in optical and infrared astronomy," *Annual Review of Astronomy Astrophysics*, vol. 47, no. 1, pp. 253–289, 2009.

[99] K. Stapelfeldt, "Extrasolar planets and star formation: Science opportunities for future elts, the scientific requirements for extremely large telescopes," in *Proceedings of the 232nd Symposium of the International Astronomical Union*, 2005, pp. 149–158.

[100] R. Angel, "Ground based imaging of extrasolar planets using adaptive optics," *Nature*, vol. 368, pp. 203–207, 1994.

[101] M. Perrin, A. Sivaramakrishnan, R. Makidon, B. Oppenheimer, and J. Graham, "The structure of high strehl ratio point-spread functions," *Astrophysical Journal*, vol. 596, pp. 702–712, 2003.

[102] M. Kuchner and W. Traub, "A coronagraph with a band-limited mask for finding terrestrial planets," *Astrophysical Jounral*, vol. 570, no. 2, pp. 900–908,

[103] N.J. Kasdin, R. Vanderbei, D. Spergel, and M. Littman, "Extrasolar planet finding via optimized apodized pupil and shaped pupil coronagraphs," *Astrophysical Journal*, vol. 582, pp. 1147–1161, 2003.

[104] O. Guyon, E. Pluzhnik, R. Galicher, F. Martinache, S. Ridgway, and R. Woodruff, "Exoplanet imaging with a phase-induced amplitude apodization coronagraph. i. principle," *Astrophysical Journal*, vol. 622, pp. 744–758, 2005.

[105] E. Serabyn, D. Mawet, and R. Burruss, "An image of an exoplanet separated by two diffraction beamwidths from a star," *Nature*, vol. 464, no. 7291, pp. 1018–1020, 2010.

[106] D. Mawet, E. Serabyn, K. Liewer, R. Burruss, J. Hickey, and D. Shemo, "The vector vortex coronagraph: Laboratory results and first light at palomar observatory," *Astrophysical Journal*, vol. 709, no. 1, pp. 53–57, 2010.

[107] P. Deroo, M. Swain, and R. Green, "Spectroscopy of exoplanet atmospheres with the finesse explorer mission," 2012.

[108] W. Cash, E. Schindhelm, J. Arenberg, R. Polidan, N. J. Kasdin, R. Vanderbei, S. Kilston, and C. Noecker, "External occulters for direct observation of exoplanets: An overview," *UV/Optical/IR Space Telescopes: Innovative Technologies and Concepts III*, 2007.

[109] R. G. Lyon, M. Clampin, R. Woodruff, G. Vasudevan, M. Shao, M. Levine, G. Melnick, V. Tolls, P. Petrone, P. Dogoda, J. Duval, and J. Ge, "Visible nulling coronagraphy for exo-planetary detection and characterization," *Direct Imaging of Exoplanets: Science Techniques*, 2006.

[110] D. Defrere, C. Stark, K. Cahoy, and I. Beerer, "Direct imaging of exoearths embedded in clumpy debris disks," 2012.

[111] M. D. Lallo, R. B. Makidon, S. Casertano, and J. E. Krist, "Temporal optical behavior of hst: Focus, coma, and astigmatism history," vol. 6270, 2006. DOI: 10.1117/12.672040. [Online]. Available: http://dx.doi.org/10.1117/12.672040.

[112] T. Mai, Ed., *Technology readiness level*, 2012. [Online]. Available: https://www.nasa.gov/directorates/heo/scan/engineering/technology/txt_accordion1.html.

[113] A. Saenz-Otero, "Design Principles for the Development of Space Technology Maturation Laboratories aboard the International Space Station," Doctor of Philosophy, Massachusetts Institute of Technology, 2005.

[114] B. Stark, "Mems reliability assurance guidelines for space applications," Tech. Rep., 1999. DOI: JPL-Publ-99-1.

[115] W. van Spengen, "Mems reliability from a failure mechanisms perspective," *Microelectronics Reliability*, vol. 43, no. 7, pp. 1049–1060, 2003.

[116] Paul Bierden, Thomas Bifano, Steven Cornelissen, Jeremy Kasdin, and Marie Levine, "Technology Milestone White Paper: MEMS Deformable Mirror Technology," Tech. Rep. JPL Document D-81373, 2013.

[117] H. Shea, "Reliability of mems for space applications," in *Proc. SPIE*, 2006.

[118] "General environmental verification standard for gsfc flight programs and projects," Tech. Rep., 2013. DOI: GSFC-STD-7000.

[119] A. Travinsky, D. Vorobiev, A.D. Raisanen, J. Pellish, Z. Ninkov, M. Robberto, and S. Heap, "The effects of heavy ion radiation on digital micromirror device performance," in *Proc. SPIE*, vol. 9761, 2016.

[120] R. Young, "Flight opportunities," in *FAA Commercial Space Tranportation Conference*, 2016.

[121] E.S. Douglas, K. Hewasawam, C.B. Mendillo, K.L. Cahoy, T.A. Cook, S.C. Finn, G.A. Howe, M.J. Kuchner, N.K. Lewis, A.D. Marinan, D. Mawet, and S. Chakrabarti, "End-to-end simulation of high-contrast imaging systems: Methods and results for the picture mission family," vol. 9605, 2015.

[122] "Nanoracks: First commercial laboratory in space," NanoRacks LLC, Tech. Rep., 2012. [Online]. Available: `http://nanoracks.com/wp-content/uploads/NanoRacks-Commercial-Spacelab-Presentation-1.pdf`.

[123] H.G. Pippin, S.L.B. Woll, K.Y. Blohowiak, L.K. Olli, and J.H. Osborne, "On-orbit and ground testing of space environment interactions with materials," *Progress in Organic Coatings*, vol. 47, pp. 458–468, 2003.

[124] Roy W. Spencer, "The role of passive microwave radiometers in climate monitoring," NASA Space Science and Techology Center, Tech. Rep.

[125] K. Cahoy, J.M. Byrne, T. Cordeiro, P. Dav, Z. Decker, A. Kennedy, R. Kingsbury, A. Marinan, W. Marlow, T. Nguyen, S. Shea, W. J. Blackwell, G. Allen, C. Galbraith, V. Leslie, I. Osaretin, M. DiLiberto, P. Klein, M. Shields, E. Thompson, D. Toher, D. Freeman, J. Meyer, and R. Little, "The Microwave Radiometer Technology Acceleration CubeSat (MiRaTA)," in *Earth Science Technology Forum*, 2015.

[126] S. T. Brown, S. Desai, W. Lu, and A. Tanner, "On the Long-Term Stability of Microwave Radiometers Using Noise Diodes for Calibration," *IEEE Transactions on Geoscience and Remote Sensing*, vol. 5, no. 7, pp. 1908–1920, 2007.

[127] D. W. Draper, D. A. Newell, D. S. McKague, and J. R. Piepmeier, "Assessing calibration stability using the global precipitation measurement (gpm) microwave imager (gmi) noise diodes," *IEEE Journal of Selected Topics in Applied Earth Observations and Remote Sensing*, vol. 8, no. 9, pp. 4239–4247, 2015.

[128] Christina Muth, Paul S. Lee, James C. Shiue, and W. Allan Webb, "Advanced Technology Microwave Sounder on NPOESS and NPP," *IEEE*, pp. 2454–2458, 2004. DOI: 0-7803-8742-2/04.

[129] E. Fetzer, L. M. McMillin, D. Tobin, H. H. Aumann, M. R. Gunson, W. W. McMillan, D. E. Hagan, M. D. Hofstader, J. Yoe, D. N. Whiteman, J. E. Barnes, R. Bennartz, H. Vomel, V. Walden, M. Newchurch, P. J. Minnett, R. Atlas, F. Schmidlin, E. T. Olsen, M. D. Goldberg, S. Zhou, H. Ding, W. L. Smith, and H. Revercomb, "Airs/amsu/hsb validation," *IEEE Transations on Geoscience and Remote Sensing*, vol. 41, no. 2, pp. 418–431, 2003.

[130] B. Tian, C. O. Ao, D. E. Waliser, E. J. Fetzer, A. J. Mannucci, and J. Teixeira, "Intraseasonal temperature variability in the upper troposphere and lower stratosphere from the gps radio occultation measurements," *J. Geophys. Res.*, vol. 117, no. D15110, 2012.

[131] Hajj, G.A. Kursinski, E.R., Schofield, J. T., Linfield, R. P., and Hardy, K. R., "Observing Earth's atmosphere with radio occultation measurements using the Global Positioning System," *Journal of Geophysical Research*, vol. 102, no. D19, pp. 23 429–23 465, Oct. 1997. DOI: 0148-0227/97/97JD-01569509.00.

[132] G.A. Hajj, E. R. Kursinski, L. J. Romans, W. I. Bertiger, and S.S. Leroy, "A technical description of atmospheric sounding by GPS occultation," JASTP, *Journal of Atmospheric and Solar-Terrestrial Physics*, vol. 64, pp. 451–469, 2002. DOI: 1364-6826/02.

[133] Radiocommunication Sector of ITU, "Attenuation by atmospheric gases," Geneva, Tech. Rep. Recommendation ITU-R P.676-10, Sep. 2013.

[134] G. Fjeldbo, A. Kliore, and V. R. Eshlemann, "The neutral atmosphere of Venus studied with the Mariner V radio occultation experiments," *Journal of Astronomy*, vol. 76, no. 2, 123–140, 1971.

[135] D. J. Jacob, *Introduction to Atmospheric Chemistry*. Princeton, NJ: Princeton University Press, 1999.

[136] Bilal Ahmad, "Accuracy and Resolution of Atmospheric Profiles Obtained from Radio Occultation Measurements," English, Doctor of Philosophy, Stanford University, Palo Alto, CA, Dec. 1998.

[137] Jeremy Harrison, Peter Bernath, and Gottfried Kirchengast, "Spectroscopic requirements for ACCURATE, a microwave and infrared-laser occultation satellite mission," *Journal of Quantitative Spectroscopy & Radiative Transfer*, vol. 112, pp. 2347–2354, 2011. DOI: 10.1016/j.jqsrt.2011.06.003.

[138] M. Schneider and F. Hase, "Improving spectroscopic line parameters by means of atmospheric spectra: Theory and example for water vapor and solar absorption spectra," *Journal of Quantitative Spectroscopy & Radiative Transfer*, vol. 110, pp. 1825–1839, 2009. DOI: 10.1016/j.jqsrt.2009.04.011.

[139] N. Perlot, "Atmospheric occultation of optical intersatellite links: Coherence loss and related parameters," *Applied Optics*, vol. 48, no. 12, pp. 2290–2302, 2009.

[140] J. W. Hardy, *ADAPTIVE Optics for Astronomical Telescopes*. New York: Oxford University Press, 1998.

[141] Wesley Traub and Ben Oppenheimer, "Direct Imaging of Exoplanets," *Exoplanets*, S. Seager, Ed., pp. 111–156, 2010.

[142] W. Southwell, "Wave-front estimation from wave-front slope measurements," English, *Journal of Optical Society of America*, vol. 70, no. 8, pp. 998–1006, Aug. 1980.

[143] Seng-Whan Bahk, "Highly accurate wavefront reconstruction algorithms over broad spatial-frequency bandwidth," *Optics Express*, vol. 19, no. 20, Sep. 2011.

[144] Johannes Pfund, Norbert Lindlein, and Johannes Schwider, "Misalignment effects of the ShackHartmann sensor," *Applied Optics*, vol. 37, no. 1, pp. 22–27, Jan. 1998.

[145] T. Fusco, S. Thomas, M. Nicolle, A. Tokovinin, V. Michau, and G. Rousset, "Optimization of Center of Gravity algorithms in a Shack-Hartmann sensor," in *Proceedings of SPIE*, vol. 6272, 2006, pp. 1–11. (visited on 06/09/2014).

[146] Damien Gratadour, Eric Gendron, and Gerard Rousset, "Symmetrically weighted center of gravity for Shack-Hartmann wavefront sensing on a laser guide star," in *Proc. SPIE*, vol. 7736, 2010.

[147] Virendra N. Mahajan, "Zernike Circle Polynomials and Optical Aberrations of Systems with Circular Pupils," *Supplement to Applied Optics*, pp. 8121–8124, Dec. 1994.

[148] R. J. Noll, "Zernike Polynomials and Atmospheric Turbulence," *The Optical Society of America*, vol. 66, no. 3, pp. 207–211, Mar. 1976.

[149] *Verifire Laser Interferometers*, 2010. [Online]. Available: `http://www.zygo.com/met/interferometers/verifire/verifire_br.pdf`.

[150] *Verifire QPZ Specification*, 2014. [Online]. Available: `http://www.zygo.com/met/interferometers/verifire/qpz/Verifire_QPZ_Specs.pdf`.

[151] Zygo Corporation, *MetroPro Reference Guide, version 9.0*, 2011.